

Summer 2017

Modeling The Gross-Pitaevskii Equation using The Quantum Lattice Gas Method

Armen M. Oganosov

College of William and Mary - Arts & Sciences, armen.ox@gmail.com

Follow this and additional works at: <https://scholarworks.wm.edu/etd>



Part of the [Physics Commons](#)

Recommended Citation

Oganosov, Armen M., "Modeling The Gross-Pitaevskii Equation using The Quantum Lattice Gas Method" (2017). *Dissertations, Theses, and Masters Projects*. Paper 1530192375.

<http://dx.doi.org/10.21220/s2-2dcm-7v23>

This Dissertation is brought to you for free and open access by the Theses, Dissertations, & Master Projects at W&M ScholarWorks. It has been accepted for inclusion in Dissertations, Theses, and Masters Projects by an authorized administrator of W&M ScholarWorks. For more information, please contact scholarworks@wm.edu.

Modeling the Gross-Pitaevskii Equation Using the Quantum Lattice Gas Method

Armen Oganessov
New York, New York

Master of Science, College of William & Mary, 2013
Bachelor of Arts, Hunter College, 2010

A Dissertation presented to the Graduate Faculty
of The College of William & Mary in Candidacy for the Degree of
Doctor of Philosophy

Department of Physics

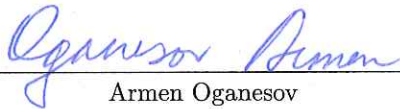
College of William & Mary
January 2018

©2018
Armen Oganessov
All rights reserved.

APPROVAL PAGE

This Dissertation is submitted in partial fulfillment of
the requirements for the degree of

Doctor of Philosophy



Armen Oganessov

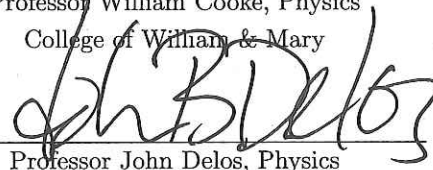
Approved by the Committee, November 2017


9/11/17


Committee Chair

Professor George Vahala, Physics
College of William & Mary


Professor William Cooke, Physics
College of William & Mary


Professor John Delos, Physics
College of William & Mary


Professor Marc Sher, Physics
College of William & Mary


Dr. Robert Rubinstein, Physics
NASA Langley Research Center

ABSTRACT

We present an improved Quantum Lattice Gas (QLG) algorithm as a mesoscopic unitary perturbative representation of the mean field Gross Pitaevskii (GP) equation for Bose-Einstein Condensates (BECs). The method employs an interleaved sequence of unitary collide and stream operators. QLG is applicable to many different scalar potentials in the weak interaction regime and has been used to model the Korteweg-de Vries (KdV), Burgers and GP equations. It can be implemented on both quantum and classical computers and is extremely scalable. We present results for 1D soliton solutions with positive and negative internal interactions, as well as vector solitons with inelastic scattering. In higher dimensions we look at the behavior of vortex ring reconnection. A further improvement is considered with an improved operator splitting technique via a Fourier transformation. This is great for quantum computers since the quantum FFT is exponentially faster than its classical counterpart which involves non-local operations on the entire lattice (Quantum FFT is the backbone of the Shor algorithm for quantum factorization). We also present an imaginary time method in which we transform the Schrödinger equation into a diffusion equation for recovering ground state initial conditions of a quantum system suitable for the QLG algorithm.

TABLE OF CONTENTS

Acknowledgments	iii
Dedication	iv
List of Figures	v
CHAPTER	1
1 Introduction	1
2 The Gross-Pitaevskii Equation	4
2.1 Bose-Einstein Condensates	4
2.2 Gross-Pitaevskii Equation	6
2.3 Some GPE Results	11
2.3.1 Dimensionless GPE	11
2.3.2 Madelung Transform and Quantization	13
2.3.3 Energy of a GPE System	14
3 Quantum Lattice Gas Algorithm	16
3.1 Quantum Bits	16
3.2 Square Root of Swap	21
3.3 Relativistic Dirac collision operator	26
3.4 Non-Relativistic Operator with Phase	40
4 QLG Simulation Results	43
4.1 1D Quantum Harmonic Oscillator	43
4.2 Bright Solitons	45
4.3 Vector Solitons	53

4.4	Dark Solitons	57
4.5	Vortex Rings	63
5	Imaginary Time	72
5.1	Imaginary-Time Collision Operator	72
5.2	1D SHO	74
5.3	1D NLS	75
6	Road Forward	80
6.1	Fourier Operator Splitting	80
6.2	Spin-1 Interaction	83
7	Conclusion	85
APPENDIX A		
	BEC Phase State Derivation	88
APPENDIX B		
	Brief Derivation of Second Quantization	92
APPENDIX C		
	Dimensionless GPE	101
	Bibliography	105

ACKNOWLEDGMENTS

I would like to thank George Vahala for his infinite patience and Min Soe for guidance in navigating through all the programming involved. My committee for making this possible, and the William & Mary physics department for their support. Lastly the DoD for giving us all that computer time on their large fancy machines.

I present this thesis in honor of both of my mothers and sister, whose efforts on my behalf lead to a future.

LIST OF FIGURES

3.1	<i>Bloch sphere</i> representation	18
4.1	FIG: 4.1 Simulation results for SHO ground state and first two excited states. . .	45
4.2	The deviation of the QLG solution after $t = 10^6$ iterations from its analytic counterpart for the case $n = 0$ shown in Fig. [4.1a].	46
4.3	Snapshot of $ \psi(x, t_i) $ at 8000 time intervals ($\Delta t = 8k$) for (<i>top</i>) pre-collision and (<i>bottom</i>) post-collision soliton motion. Initially, the larger soliton has its peak around $x \sim -2000$ while the smaller soliton has its peak around $x \sim +2000$. Color scheme for (<i>top</i>): blue ($t = 0$) \rightarrow red ($t = 8k$) \rightarrow brown ($t = 16k$) \rightarrow green ($t = 24k$) \rightarrow blue ($t = 32k$) \rightarrow red-overlap ($t = 40k$). Color scheme for (<i>bottom</i>): blue-overlap ($t = 40k$) \rightarrow red ($t = 48k$) \rightarrow brown ($t = 56k$) \rightarrow green ($t = 64k$) \rightarrow blue ($t = 72k$) \rightarrow red ($t = 80k$). The large amplitude soliton always moves to the right while the lower amplitude soliton always moves to the left under periodic boundary conditions. Soliton overlap/collision occurs at $t = 40k$. Note that the solitons move with the same amplitude and speed pre- and post-collision.	49
4.4	Snapshot of $ \psi(x, t_i) $ at time intervals of ($\Delta t = 8k$) for the post-15 th collision. Initial time instant for these six snap-shots is $t = 832k$ with the larger soliton peak at around $x \sim -2200$, and the smaller peak at $x \sim +1950$: (<i>top</i>) pre-15 th collision and (<i>bottom</i>) post-15 th collision soliton motion. The color scheme is the same as in Figure [4.2].	50
4.5	The time evolution of the collision-induced spatial phase shifts in the larger soliton with speed $\beta = 0.5$ lattice units/time step. The spatial shift in-between soliton-soliton collisions is basically a constant, as expected theoretically for soliton-soliton collisions of 1D NLS. The Gibbs-like spikes that appear during the soliton-soliton overlap collision is a numerical artifact on the use of the peak in $ \psi $ during the collision.	51
4.6	The time evolution of the energy integral, a constant of the motion of the 1D NLS Hamiltonian system. For the chosen parameters, $E_{const.} = -0.889$. The Gibbs-like spikes that appear during the soliton-soliton overlap collision are numerical artifacts related to the stencil used to calculate Equation [4.6]	52
4.7	The collisional evolution of Manakov solitons left figure. The pre-collision states at $t = 0$, $t = 10K$, $t = 20K$ while the post-collision states right figure are at times $t = 25K$, $t = 35K$, $t = 45K$. The first polarization amplitude 2-soliton $ Q_1(x, t) $ is in blue, while the orthogonal polarization 2-soliton $ Q_2(x, t) $ is in red. The inelastic soliton collision occurs for specially chosen soliton amplitudes and speeds, and in this case the post-collision soliton for $ Q_1(x, t) = 0$ for $x < 3000$ is totally absent. Simulations performed on a grid $L = 6000$, under periodic boundary conditions. . .	57

4.8	A plot of the time evolution of the vector 2-soliton peaks, $max_{1 \leq x \leq L} Q_n(x, t) $, $n = 1, 2$, in each mode. Vector soliton-soliton collisions occur whenever the peaks spike. For the parameters chosen, an inelastic Manakov soliton collision occurs only for $t = 24K$, with the subsequent loss of one of the solitons. This soliton reappears following the next vector soliton-soliton overlap collision. The dashed curves are for the higher amplitude soliton within that particular mode, while the solid curve is for the lower soliton amplitude. For the integrable Manakov system the vector 2-soliton solution exhibits invariant soliton properties away from the collisional overlap regions: i.e., the constant horizontal sections indicate the non-overlapping soliton spatial regions.	58
4.9	Two dark solitons with an equal depth of $\alpha = 0.025$ and velocities $\beta = \pm 0.025$ lattice units/time step. At $t = 0$ the left soliton is moving to the right and the right soliton is moving to the left. At $t = 3.94 \times 10^4$ we observe an almost complete overlap of the two solitons, and at $t = 6 \times 10^4$ they have passed through each other. The grid length $L = 3000$ with $\Delta x = 1$	60
4.10	Two dark solitons with an equal depth of $\alpha = 0.0375$ and velocities $\beta = \pm 0.00625$ lattice units/time step. At $t = 0$ the left soliton is moving to the right and the right soliton is moving to the left. At $t = 3.7 \times 10^4$ we observe the maximum partial overlap of the two solitons before their velocities change sign, and at $t = 5 \times 10^4$ the initial left (right) soliton is moving left (right). The grid length $L = 800$ with $\Delta x = 1$	61
4.11	FIG: 4.11	62
4.12	Modeling dark solitons with velocity $\beta = 0.06875$ (lattice units)/(time step). This velocity is too high which is reflected in the lack of energy conservation throughout the simulation.	63
4.13	FIG: 4.13 Isosurfaces of vortex-rings	68
4.14	FIG: 4.14 Poincaré recurrence in vortex-ring simulations.	69
4.15	FIG: 4.15 Simulation of vortex-ring reconnection in a stronger interaction regime.	71
5.1	(a) IT-QLG testing stability over 4×10^5 iterations. $\Omega = [-500, 500]$, $\Delta x = \frac{1}{\sqrt{2}}$, $k = \frac{1}{\Omega^2}$. (b) $Error = \psi_{analytic} - \psi_{IT} $. Comparing the analytic ground state for the SHO and the IT-QLG algorithm result. (c) IT-QLG ground state solution after 3.5×10^3 iterations, same parameters as in Fig.[5.1a]. (d) $Error = \psi_{analytic} - \psi_{IT} $	76
5.2	(a) Matching Succi's result for the 1D NLS equation. $\Omega = [-150, 150]$, $\Delta x = \frac{1}{2}$, $\Delta_0 = 16$, $\omega = \frac{1}{128}$, $m = 1/8$ and $\beta = +1$. (b) Difference between the BEFD ($\Delta x = 0.1$) converged value versus the QLG-IT algorithm, $Error = \psi_{BEFD} - \psi_{IT} $	78
5.3	(a) Stationary bright-soliton solutions for the 1D NLS. $\Omega = [-500, 500]$, $\beta = -1$, $\Delta x = 1$. Here, ψ_0 is purely real producing a single soliton and ψ_{10} has a complex phase producing two solitons. (b) Energy of the stationary solutions when substituted into the time-evolving unitary QLG algorithm.	78
5.4	(a) Stationary dark-soliton solution for the 1D NLS. $\Omega = [-500, 500]$, $\beta = +1$, $\Delta x = 1$, $\alpha = 0.1$. (b) Energy stability of the stationary solution when substituted into the time-evolving QLG algorithm for 5×10^4 time steps.	79

6.1	Bright-soliton collision using the QLG sequence presented in eq. [6.2]. Simulation performed on a grid of length $L = 4096$ with $\Delta x = \Delta t = 1$, and velocity $\beta = 0.06875$ with the left most soliton moving to the right and right soliton to the left.	82
7.1	Testing strong scalability of a prototype spin-1 QLG algorithm on the Argonne's supercomputer Mira.	86
7.2	Testing weak scalability of a prototype spin-1 QLG algorithm on the Argonne's supercomputer Mira.	86
A.1	The polylogarithm function $Li_n(z) = \sum_{p=1}^{\infty} \frac{z^p}{(p+c)^n}$ plotted for $n = 3/2$, $c = 0$ and $0 < z \leq 1$	90

MODELING THE GROSS-PITAIEVSKII EQUATION USING THE QUANTUM
LATTICE GAS METHOD

CHAPTER 1

Introduction

Many advances have been made recently that are paving the way forward to quantum computing. Alongside these advancements algorithms have been developed to take advantage of the future technology as quantum information systems hold a lot of promise for greater understanding of the nano world. Unlike in classical computers where operations are often represented by stochastic or permutation matrices, a quantum operator U must be a unitary matrix, satisfying

$$U^\dagger U = I \tag{1.1}$$

where U^\dagger is the Hermitian conjugate of U , and I is the identity. Due to the unitary nature of quantum operators, which we call gates in line with their classical counterparts, quantum gates are logically reversible. The significance of this can be easily seen if we consider an irreversible classical AND gate. An AND gate implements the logical conjunction 'and' in

a digital circuit. It returns a positive output of 1, only when both inputs are also 1, it 'effectively finds the minimum between two binary digits'¹. When an AND gate processes bits of data, there is a loss of information involved that manifests in energy dissipated equal to $kT\ln(2)$ for every bit that is erased (k being the Boltzmann's constant and T temperature in Kelvin of the chip at which the computation was performed). Many advances in modern computers came from the development of reversible gates allowing for a reduction in energy dissipation, that often comes in the form of heat. This paved the way for greater miniaturization of modern chips. Having such an advantage inherent in a quantum gate is one of the many drivers for quantum computing. How quantum gates are currently manifested in the lab varies depending on how the qubits that they act upon are encoded. For example when dealing with spin qubits, the gate is applied through the manipulation of a magnetic field, while for qubits encoded in an ion trap, the gate operations are performed by varying the laser beam acting on the ions.

This dissertation will focus on a particular quantum algorithm, the Quantum Lattice Gas method, QLG for short. The method employs a novel approach towards quantum dynamics via qubits, first introduced by Feynman². These qubit representations permit close to ideal parallelization on even classical supercomputers. The specific QLG considered was originally developed by Yezek and Boghosian³, here we present the next iteration of this method. QLG while a quantum algorithm can also be implemented on classical computers allowing us to test its efficacy and scalability. There are many existing numerical approaches to tackling physical problems, the advantages offered by QLG are its ability to be employed

on large computer clusters and utilize many cores simultaneously, as well as future functionality on quantum computers. This dissertation is organized in the following manner: Chapter 2 will be an introduction to the Gross-Pitaevskii equation, the physical system we set out to model; Chapter 3 will introduce the QLG algorithm with some background on its previous iteration, as well as the currently implemented matrix operator; Chapter 4 will present simulation results for various systems; Chapter 5 will look at an imaginary time approach to determine initial conditions, along with some results; Chapter 6 will present the road forward using a more robust operator splitting technique; and lastly Chapter 7 will conclude this thesis.

CHAPTER 2

The Gross-Pitaevskii Equation

2.1 Bose-Einstein Condensates

Before we delve into the Gross-Pitaevskii equation, it is worthwhile to have a brief discussion about the physical system it describes, the Bose-Einstein condensates (BEC). A BEC is a state of matter that occurs at very low temperatures, in which the majority of the particles condense into the ground quantum state, a condensate. Only bosons (integer spin particles) can undergo this particular phase transition, since the Pauli exclusion principle disallows fermions (half-integer spin particles) from occupying the same quantum state. That has not stopped nature though, in that super-conductivity is believed to be a condensate of electron pairs, dubbed Cooper pairs after Leon Cooper who described the phenomena in 1956. Einstein originally predicted the existence of condensates sometime in 1925⁴, but it was not until much later that they would be realized in experiments. A detailed look at the derivation

can be seen in Appendix A. The difficulty stemmed from just how cold the atoms had to be, near absolute zero (100 nK). The first successful BEC was created in 1995⁵, using a number of clever techniques such as laser cooling atoms in a harmonic trap, magnetic trapping and evaporative cooling. Laser cooling takes advantage of the Doppler effect of a thermal atom moving away or toward a laser beam. If the beam's energy is slightly less than the transition energy of an atomic species, then an incoming atom, appearing blue-shifted, will absorb the incoming photon. Later the excited atom will release a photon with a higher energy than the one originally absorbed, losing momentum in the process. Conversely the atom moving away from the beam will be slightly red-shifted and will ignore the beam entirely. While this reduces the average temperature of the system, magnetic traps are used to keep the neutral atoms confined. Typically done via devices called MOTs (magnetic-optical traps), a spherical quadrupole magnetic configuration is used which applies a restoring force on the trapped atoms towards the center. This is done through the interaction of the magnetic-dipole moment with the external magnetic fields. Lastly evaporative cooling is employed to further reduce the average temperature of the system to the appropriate BEC transition temperature. Evaporative cooling is a process in which the trapping potential amplitude is gradually lowered, allowing more energetic atoms to escape the trap, leaving behind the atoms with an overall lower average kinetic energy. Conceptually this idea is no different from cooling your hot cup of tea by leaving it idle while the hot particles escape via evaporation. Interested readers can refer to the plethora of literature that covers all of these topics in great detail, including the more modern techniques of optical cooling, for example⁶.

2.2 Gross-Pitaevskii Equation

The next topic to consider, is how do we model a Bose-Einstein condensate? This is effectively answered by the Gross-Pitaevskii equation (GPE)⁷.

$$i\hbar\partial_t\psi = \frac{-\hbar^2}{2m}\nabla^2\psi + V(\mathbf{r})\psi + (g_0N|\psi|^2 - \mu)\psi \quad (2.1)$$

where ψ is the 1-particle wave function to which all the BEC particles collapse at $T = 0$, $V(\mathbf{r})$ is an external trapping potential, N is the number of particles, μ is the chemical potential and the coupling constant $g_0 = \frac{4\pi\hbar^2 a_s}{m}$ with a_s as the scattering length. Below we derive the GPE since it is the main result we work with and attempt to model. For the derivation we will ignore the chemical potential μ as it can be incorporated into $V(\mathbf{r})$ from a mathematical standpoint. We begin with the 2nd quantized Hamiltonian (Appendix B),

$$\hat{H} = \int d^3r \hat{\psi}^\dagger(r) H_0 \hat{\psi}(r) + \frac{1}{2} \int d^3r \int d^3r' \hat{\psi}^\dagger(r) \hat{\psi}^\dagger(r') V_{int}(r, r') \hat{\psi}(r') \hat{\psi}(r) \quad (2.2)$$

$$H_0 = \frac{-\hbar^2}{2m} \nabla^2 + V_{ext}$$

$$V_{int} = \text{is the inter-particle interaction between the bosons} \quad (2.3)$$

$$V_{ext} = \frac{1}{2}m (\omega_x^2 x^2 + \omega_y^2 y^2 + \omega_z^2 z^2)$$

ω 's are the trapping frequencies along the respective dimension and m is the mass of the particles. We assume that the bosonic gas is dilute with hard-sphere elastic collisions between

the atoms and their interaction is modeled by a Dirac δ function potential

$$V_{int}(\mathbf{r}, \mathbf{r}') = g_0 \delta(\mathbf{r} - \mathbf{r}') \quad (2.4)$$

The s-wave scattering length is positive for repulsive interactions and negative for attractive interactions. Inserting the eq. [2.4] potential into the second term of our Hamiltonian in eq. [2.2] we easily integrate out the r' dependence,

$$\hat{H} = \int d^3r \hat{\psi}^\dagger(r) H_0 \hat{\psi}(r) + \frac{g_0}{2} \int d^3r \hat{\psi}^\dagger(r) \hat{\psi}^\dagger(r) \hat{\psi}(r) \hat{\psi}(r) \quad (2.5)$$

Using Heisenberg's equation of motion we look at the time evolution of our wavefunction with our Hamiltonian (eq. [2.5]).

$$\begin{aligned} i\hbar \partial_t \hat{\psi}(r') &= [\hat{\psi}(r'), \hat{H}] \\ &= \hat{\psi}(r') \hat{H} - \int d^3r \hat{\psi}^\dagger(r) H_0 \hat{\psi}(r) \hat{\psi}(r') - \frac{g_0}{2} \int d^3r \hat{\psi}^\dagger(r) \hat{\psi}^\dagger(r) \hat{\psi}(r) \hat{\psi}(r) \hat{\psi}(r') \end{aligned} \quad (2.6)$$

Note that $\hat{\psi}$ depends on both space and time. Using the bosonic commutation relations (refer to Appendix B eq. [B.7]),

$$\begin{aligned} [\hat{\psi}^\dagger(r'), \hat{\psi}(r)] &= \delta(r' - r) \\ [\hat{\psi}^\dagger(r'), \hat{\psi}^\dagger(r)] &= [\hat{\psi}(r'), \hat{\psi}(r)] = 0 \end{aligned} \quad (2.7)$$

we can simplify eq. [2.5]. Going term by term we start with the first term on the right hand side of eq. [2.6].

$$\begin{aligned}
\hat{\psi}(r')\hat{H} &= \int d^3r \hat{\psi}(r')\hat{\psi}^\dagger(r)H_0\hat{\psi}(r) + \frac{g_0}{2} \int d^3r \hat{\psi}(r')\hat{\psi}^\dagger(r)\hat{\psi}^\dagger(r)\hat{\psi}(r)\hat{\psi}(r) \\
&= \int d^3r \hat{\psi}(r')\hat{\psi}^\dagger(r)H_0\hat{\psi}(r) + \frac{g_0}{2} \int d^3r \left\{ \left[\hat{\psi}(r'), \hat{\psi}^\dagger(r) \right] \hat{\psi}^\dagger(r)\hat{\psi}(r)\hat{\psi}(r) + \hat{\psi}^\dagger(r)\hat{\psi}(r')\hat{\psi}^\dagger(r)\hat{\psi}(r)\hat{\psi}(r) \right\} \\
&= \int d^3r \hat{\psi}(r')\hat{\psi}^\dagger(r)H_0\hat{\psi}(r) + \frac{g_0}{2} \int d^3r \left\{ \delta(r' - r)\hat{\psi}^\dagger(r)\hat{\psi}(r)\hat{\psi}(r) + \hat{\psi}^\dagger(r)\hat{\psi}(r')\hat{\psi}^\dagger(r)\hat{\psi}(r)\hat{\psi}(r) \right\}
\end{aligned} \tag{2.8}$$

Next we look at the the second term on the right hand side of eq. [2.6]

$$\begin{aligned}
\int d^3r \hat{\psi}^\dagger(r)H_0\hat{\psi}(r)\hat{\psi}(r') &= \int d^3r \left\{ \left[\hat{\psi}^\dagger(r), \hat{\psi}(r') \right] H_0\hat{\psi}(r) + \hat{\psi}(r')\hat{\psi}^\dagger(r)H_0\hat{\psi}(r) \right\} \\
&= \int d^3r \left\{ - \left[\hat{\psi}(r'), \hat{\psi}^\dagger(r) \right] H_0\hat{\psi}(r) + \hat{\psi}(r')\hat{\psi}^\dagger(r)H_0\hat{\psi}(r) \right\} \tag{2.9} \\
&= \int d^3r \left\{ -\delta(r' - r)H_0\hat{\psi}(r) + \hat{\psi}(r')\hat{\psi}^\dagger(r)H_0\hat{\psi}(r) \right\}
\end{aligned}$$

The second term of eq. [2.9] cancels the first term of eq. [2.8]! Looking at the third and final term on the right hand side of eq. [2.6],

$$\begin{aligned}
\frac{g_0}{2} \int d^3r \hat{\psi}^\dagger(r)\hat{\psi}^\dagger(r)\hat{\psi}(r)\hat{\psi}(r)\hat{\psi}(r') &= \frac{g_0}{2} \int d^3r \left\{ \left[\hat{\psi}(r'), \hat{\psi}^\dagger(r), \right] \hat{\psi}^\dagger(r)\hat{\psi}(r)\hat{\psi}(r) + \hat{\psi}^\dagger(r)\hat{\psi}(r')\hat{\psi}^\dagger(r)\hat{\psi}(r)\hat{\psi}(r) \right\} \\
&= \frac{g_0}{2} \int d^3r \left\{ - \left[\hat{\psi}^\dagger(r), \hat{\psi}(r') \right] \hat{\psi}^\dagger(r)\hat{\psi}(r)\hat{\psi}(r) + \hat{\psi}^\dagger(r)\hat{\psi}(r')\hat{\psi}^\dagger(r)\hat{\psi}(r)\hat{\psi}(r) \right\} \\
&= \frac{g_0}{2} \int d^3r \left\{ -\delta(r' - r)\hat{\psi}^\dagger(r)\hat{\psi}(r)\hat{\psi}(r) + \hat{\psi}^\dagger(r)\hat{\psi}(r')\hat{\psi}^\dagger(r)\hat{\psi}(r)\hat{\psi}(r) \right\}
\end{aligned} \tag{2.10}$$

Again we have the second term of eq 2.10 cancel with the third term of eq. [2.8] and the first term of eq. [2.10] adding to the 2nd term of eq. [2.8]! Putting everything together we have,

$$\begin{aligned}
i\hbar\partial_t\hat{\psi}(r') &= \int d^3r\delta(r'-r)H_0\hat{\psi}(r) + g \int d^3r\delta(r'-r)\hat{\psi}^\dagger(r)\hat{\psi}(r)\hat{\psi}(r) \\
i\hbar\partial_t\hat{\psi}(r') &= \left\{ H_0 + g\hat{\psi}^\dagger(r')\hat{\psi}(r') \right\} \hat{\psi}(r') \\
i\hbar\partial_t\hat{\psi}(r) &= H_0\hat{\psi}(r) + g \left| \hat{\psi}(r) \right|^2 \hat{\psi}(r)
\end{aligned} \tag{2.11}$$

The last line in eq. [2.11] looks like the Gross-Pitaevskii equation we're after, but it contains field operators which are sums of single particle wavefunctions. Typically a BEC will have on the order of tens of thousands of atoms, and so such a problem is not tractable as is. To simplify it we proceed by splitting the operator into two parts,

$$\begin{aligned}
\hat{\psi} &= \psi + \phi \\
\phi &\ll \psi
\end{aligned} \tag{2.12}$$

Here ψ is the mean field value of the macroscopic wavefunction and ϕ is a small deviation from this mean. Following the procedure in the paper, we substitute eq. [2.12] into eq. [2.11],

$$i\hbar\partial_t(\psi + \phi) = H_0(\psi + \phi) + g |(\psi + \phi)|^2 (\psi + \phi) \tag{2.13}$$

Going term by term we first look at the LHS of eq. [2.13].

$$i\hbar\partial_t(\psi + \phi) = i\hbar\partial_t\psi + i\hbar\partial_t\phi \quad (2.14)$$

Because ϕ is very small we can assume that $\partial_t\phi = 0$. The first RHS term becomes

$$H_0(\psi + \phi) = H_0\psi + H_0\phi \quad (2.15)$$

Again we can assume that $\nabla^2\phi = 0$ in the above term although the external potential term remains. Lastly looking at the second RHS term we have,

$$\begin{aligned} g_0 |(\psi + \phi)|^2 (\psi + \phi) &= g \{(\psi + \phi)(\psi^\dagger + \phi^\dagger)\} (\psi + \phi) \\ &= g_0 \{(\psi\psi^\dagger + \psi\phi^\dagger + \phi\psi^\dagger + \phi\phi^\dagger)(\psi + \phi)\} \\ &= g_0(\psi\psi^\dagger\psi + \psi\psi^\dagger\phi + \psi\phi^\dagger\psi + \psi\phi^\dagger\phi + \phi\psi^\dagger\psi + \phi\psi^\dagger\phi + \phi\phi^\dagger\psi + \phi\phi^\dagger\phi) \end{aligned} \quad (2.16)$$

Taking all of the 0th order terms (only dependence on ψ) from equations 2.14, 2.15 and 2.16, we recover the GPE

$$\begin{aligned} i\hbar\partial_t\psi &= H_0\psi + g(\psi\psi^\dagger\psi) \\ i\hbar\partial_t\psi &= \left(\frac{-\hbar^2}{2m}\nabla^2 + V_{ext} + g|\psi|^2\right)\psi \end{aligned} \quad (2.17)$$

Of course one may consider higher order terms which is an active area of research, beyond the mean-field theory. Higher order terms are required when dealing with very dense BECs, and it has been shown that dynamic instabilities can cause, what are usually very small, quantum fluctuations to be amplified such that higher order terms are required to model the system properly⁸.

2.3 Some GPE Results

2.3.1 Dimensionless GPE

Before proceeding further we'll present the dimensionless GPE equation which we use in our simulations.

$$i\partial_t\psi = -\nabla^2\psi + g|\psi|^2\psi \quad (2.18)$$

Here $g = 4\pi a_0^2 Na$, with a_0 as the characteristic length of the system, a the scattering length and N the number of particles in the BEC. To recover eq. [2.18] we rescale the dimensions of our system (akin going to different unit basis). For the moment we'll consider an external harmonic trapping potential with equal frequencies, $\omega = \omega_x = \omega_y = \omega_z$. Our rescaled units

are,

$$\begin{aligned}
x_s &= \frac{x}{L} \\
t_s &= \frac{t}{\tau} = \omega t \\
V_{ext} &= \frac{m}{2} \omega^2 (\vec{x} \cdot \vec{x}) = \frac{mL^2}{2} \omega^2 (\vec{x}_s \cdot \vec{x}_s) \\
V_{int} &= g |\psi(x_s, t_s)|^2 \\
\Psi(x, t) &\rightarrow \psi(x_s, t_s)
\end{aligned} \tag{2.19}$$

x_s is the rescaled spatial unit, t_s is the rescaled unit of time, L is length, and τ is time. To quickly double check that all the units so far are fine recall that the coefficient of V_{int} is,

$$\begin{aligned}
g_0 &= \frac{4\pi\hbar^2 Na}{m} \\
\hbar^2 &= (Js)^2 = (J\tau)^2 = (\text{Force } L \tau)^2 = \left(m \frac{L}{\tau^2} L\tau\right)^2 = \frac{m^2 L^4}{\tau^2} \\
a &= L \text{ (unit wise)} \\
N &= \frac{\# \text{ of particles}}{\text{Volume}} = \frac{1}{L^3} \\
g &= \frac{m^2 L^4}{\tau^2} \left(\frac{1}{L^3}\right) \frac{L}{m} = m \left(\frac{L}{\tau}\right)^2 \text{ (units of energy)}
\end{aligned} \tag{2.20}$$

The complete details of recovering eq. [2.18] are presented in Appendix C. As an example of what some of these physical values actually are, for ^{87}Rb the mass $m = 1.44 \times 10^{-25}$ kg with a scattering length $a_s \approx 0.5$ nm while the characteristic length $a_0 = 50 \sim 100$ microns. Typical particle numbers of BECs are $N = 10^2 \sim 10^{15}$ and trapping frequencies used are $\omega \approx 20\pi$ (rad/sec).

2.3.2 Madelung Transform and Quantization

We can gain some insight into the quantum fluid via the Madelung transformation, transforming the complex-valued wave eq. [2.18] into two real-valued functions in polar coordinates. Specifically we take $\psi = \sqrt{\rho}e^{i\phi/2}$, with ρ as the mean density, and upon separating the real and imaginary parts recover the hydrodynamic form of the GPE.

$$\rho(r, t) = |\psi(r, t)|^2 \quad (2.21)$$

$$\partial_t \rho + \nabla \cdot (\rho \nabla \phi) = 0 \quad (2.22)$$

$$\partial_t (\nabla \phi) + \frac{1}{2}(\nabla \phi)^2 + 2g\rho - 2\frac{\nabla^2 \sqrt{\rho}}{\sqrt{\rho}} = 0 \quad (2.23)$$

Defining the velocity, $v \equiv \nabla \phi$, makes eq. [2.22] the fluid continuity equation and eq. [2.23] the compressible, irrotational Euler equation. Irrotational because the circulation, Γ , must vanish for a conservative vector field, which the velocity is.

$$\Gamma = \oint_C v dl = \int_A \nabla \times \nabla \phi = 0 \quad (2.24)$$

Thus the vorticity $\omega \equiv \nabla \times v = 0$. We identify the pressure in eq. [2.23] as

$$p(\rho^2) = 2g\rho - 2\frac{\nabla^2 \sqrt{\rho}}{\sqrt{\rho}} \quad (2.25)$$

This pressure, $p(\rho^2)$, depends only on density with $2g\rho$ being the classical pressure, while $2\frac{\nabla^2\sqrt{\rho}}{\sqrt{\rho}}$ is a unique pressure term that appears in the quantum fluid. When a fluid's state depends on density only, it is called barotropic.

Some interesting results can be gleaned from the hydrodynamic GP equations. Despite being an irrotational fluid, there is a condition under which the angular momentum is non-zero! When there is a singularity in the phase ϕ . The wavefunction will still be single-valued, but by allowing for a singularity in the phase, the change in $\Delta\phi = \phi_2 - \phi_1$, when going around the closed contour C in eq. [2.24] must be a multiple of 2π .

$$\Gamma = \oint_C v dl = \phi_2 - \phi_1 = 2\pi n \frac{\hbar}{m} \quad (2.26)$$

n in eq. [2.26] is an integer describing the winding number of the singularity. The physical manifestation of this singularity is a quantized vortex. We have to be careful here because we just allowed a singularity into our system, and often these can be unphysical. Indeed the kinetic energy of the system would diverge in the presence of a vortex at the core ($r = 0$). This can be resolved if we require the density ρ to be 0 at the vortex core. Eq. [2.24] is only valid for non-singular fields thus the vortex is a topological singularity.

2.3.3 Energy of a GPE System

Equations 2.22 and 2.23 are not well defined at the vortex core, because the phase ϕ at these locations is not well defined (recall $\rho = 0$ at the core). This is not due to any physics,

but rather is a mathematical artifact of the transformation we used. There is a more robust way to perform this transformation and this has been done by C. Nore et al.⁹. The important result for us are the energies of the condensate,

$$\begin{aligned}
 \text{kinetic energy: } E_{kin} &= \int dx \rho |v|^2 \\
 \text{internal energy: } E_{int} &= 2g \int dx \rho^2 \\
 \text{quantum energy: } E_{qua} &= 4 \int dx |\nabla \sqrt{\rho}|^2
 \end{aligned} \tag{2.27}$$

with the density $\rho = \psi^\dagger \psi$ and momentum $\rho v = i(\psi \nabla \psi^\dagger - \psi^\dagger \nabla \psi)$. The total energy of the system is the sum of all three, $E_{tot} = E_{kin} + E_{int} + E_{qua}$. In an experimental settings one can't really distinguish the individual energies in this fashion, but this can be done in simulations, where tracking the exchange of energy can provide additional insight into the physics of the problem. The result in eq. [2.27] is derived from the GPE Lagrangian \mathcal{L} ,

$$\mathcal{L} = \frac{i}{2}(\psi^\dagger \partial_t \psi - \psi \partial_t \psi^\dagger) - |\nabla \psi|^2 - \frac{g}{2} |\psi|^4 \tag{2.28}$$

\mathcal{L} in eq. [2.28] is invariant to a phase rotation, spatial translation, and a time translation which lead to the conservation of mass, momentum and energy respectively.

CHAPTER 3

Quantum Lattice Gas Algorithm

3.1 Quantum Bits

The Quantum Lattice Gas (QLG) algorithm was originally envisioned as a quantum algorithm¹⁰. The unit of information in quantum computing is a quantum bit, or qubit for short. Unlike a classical digital bit that only takes on a binary value of 0 or 1, a qubit through superposition can additionally exist as any value in between¹¹. Realizing a qubit is a very active area of research, they can be encoded in the polarization of photons, or the spin of a system, be it electron, nuclear or atomic spin. We can express a qubit as a superposition of basis states,

$$\begin{aligned} |q\rangle &= \alpha |0\rangle + \beta |1\rangle \\ |\alpha|^2 + |\beta|^2 &= 1 \end{aligned} \tag{3.1}$$

When measuring a qubit the result is either $|0\rangle$ or $|1\rangle$ with a probability of $|\alpha|^2$ or $|\beta|^2$ respectively. As briefly mentioned in the introduction, one can operate on a qubit with a quantum logic gate, a unitary transformation that will take a state $|q\rangle \rightarrow |q'\rangle = \alpha'|0\rangle + \beta'|1\rangle$.

An example quantum gate is the *Hadamard* operator,

$$H = \frac{1}{\sqrt{2}} \begin{pmatrix} 1 & 1 \\ 1 & -1 \end{pmatrix} \quad (3.2)$$

Using the matrix representation for the qubit states, $|0\rangle = \begin{pmatrix} 1 \\ 0 \end{pmatrix}$, $|1\rangle = \begin{pmatrix} 0 \\ 1 \end{pmatrix}$ one immediately sees that the action of the Hadamard gate is

$$\begin{aligned} H|0\rangle &= \frac{1}{\sqrt{2}} \begin{pmatrix} 1 & 1 \\ 1 & -1 \end{pmatrix} \begin{pmatrix} 1 \\ 0 \end{pmatrix} = \frac{1}{\sqrt{2}} \begin{pmatrix} 1 \\ 1 \end{pmatrix} = \frac{|0\rangle + |1\rangle}{\sqrt{2}} \\ H|1\rangle &= \frac{1}{\sqrt{2}} \begin{pmatrix} 1 & 1 \\ 1 & -1 \end{pmatrix} \begin{pmatrix} 0 \\ 1 \end{pmatrix} = \frac{|0\rangle - |1\rangle}{\sqrt{2}} \end{aligned}$$

QLG utilizes two qubits per lattice cell, a 2-level system which can be expressed via the *Bloch sphere* representation. We consider the state as a point on a unit sphere with polar coordinates θ and ϕ as shown in Fig. [3.1].

In this representation a *Bloch* vector is simply a spherical unit vector,

$$\vec{B}_s = (\cos(\phi)\sin(\theta), \sin(\phi)\sin(\theta), \cos(\theta)) \quad (3.3)$$

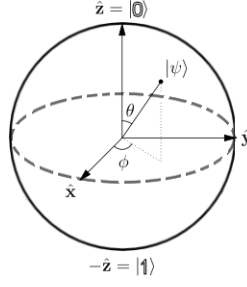


FIG. 3.1: Bloch sphere representation

and a general rotation $R_{\vec{n}}$ of a Bloch vector \vec{B}_s around a real unit vector \vec{n} is

$$R_{\vec{n}} = e^{-i\theta\vec{n} \cdot \vec{\sigma}/2} = \cos\left(\frac{\theta}{2}\right) I - i \sin\left(\frac{\theta}{2}\right) (n_x\sigma_x + n_y\sigma_y + n_z\sigma_z) \quad (3.4)$$

Here $\vec{\sigma}$ is the Pauli Matrix vector and I is the identify matrix.

$$\sigma_x = \begin{pmatrix} 0 & 1 \\ 1 & 0 \end{pmatrix}, \sigma_y = \begin{pmatrix} 0 & -i \\ i & 0 \end{pmatrix}, \sigma_z = \begin{pmatrix} 1 & 0 \\ 0 & -1 \end{pmatrix} \quad (3.5)$$

Equation [3.4] will be the starting point of generating the new collision operator in the QLG algorithm.

A second distinguishing feature of qubits is that they can exhibit quantum entanglement, non-local correlations. Two qubits are considered entangled when a measurement on one qubit affects the other, indicating that they are not entirely independent. A natural basis

for a classical qubit pair in the 2^2 dimensional Hilbert space consists of tensor product states

$$|0\rangle \otimes |0\rangle \equiv |00\rangle$$

$$|0\rangle \otimes |1\rangle \equiv |01\rangle$$

$$|1\rangle \otimes |0\rangle \equiv |10\rangle$$

$$|1\rangle \otimes |1\rangle \equiv |11\rangle$$

where it is understood that in the simplifying notation $|00\rangle$ the 1st entry is the state of the 1st qubit, while the 2nd entry is the state of the 2nd qubit. Thus any state $|\Omega_{\otimes}\rangle$ in this tensor product Hilbert space can be represented by $|\Omega_{\otimes}\rangle = (\alpha_0 |0\rangle + \alpha_1 |1\rangle) \otimes (\beta_0 |0\rangle + \beta_1 |1\rangle) = \alpha_0\beta_0 |00\rangle + \alpha_0\beta_1 |01\rangle + \alpha_1\beta_0 |10\rangle + \alpha_1\beta_1 |11\rangle$. But what if our state is $|\Phi^+\rangle = \frac{|00\rangle+|11\rangle}{\sqrt{2}}$? $|\Phi^+\rangle$ cannot be represented by a product of superpositions of the elements in the classical basis set! For $|01\rangle$ to be 0 either $\alpha_0 = 0$ or $\beta_1 = 0$. But if $\alpha_0 = 0$ then we cannot recover $|00\rangle$ and similarly for the $|11\rangle$ state if $\beta_1 = 0$. What has happened is that the tensor product Hilbert space is treating the 2 qubits independent of each other, this is how one manipulates classical bits. But for pairs of entangled qubits one finds states have their qubits correlated to each other. This correlation is what we mean by quantum entanglement. The state $|\Phi^+\rangle$ is, in fact, a maximally entangled 2-qubit state, and is called a Bell state. There are 3 other maximally entangled Bell states for the 2 qubit system which form the basis that we will be

using:

$$\begin{aligned}
 |\Phi^+\rangle &= \frac{1}{\sqrt{2}} (|0\rangle \otimes |0\rangle + |1\rangle \otimes |1\rangle) \\
 |\Phi^-\rangle &= \frac{1}{\sqrt{2}} (|0\rangle \otimes |0\rangle - |1\rangle \otimes |1\rangle) \\
 |\Psi^+\rangle &= \frac{1}{\sqrt{2}} (|0\rangle \otimes |1\rangle + |1\rangle \otimes |0\rangle) \\
 |\Psi^-\rangle &= \frac{1}{\sqrt{2}} (|0\rangle \otimes |1\rangle - |1\rangle \otimes |0\rangle)
 \end{aligned} \tag{3.6}$$

The qubits encode the quantum particle occupation probabilities and the algorithm applies a series of local unitary operations on a lattice populated by the Bell states.

QLG is a three step algorithm:

1. Initialize the wavefunction $|\psi(x, t)\rangle$
2. collision step (entangling the qubits via a quantum-gate $\hat{\mathcal{C}}$)
3. streaming (interchanging amplitudes via $\hat{\mathcal{S}}$)

The initialization step is rather straightforward, we encode the wavefunction in the qubits that span our lattice. The entangling step is performed via a collision operator $\hat{\mathcal{C}}$, in this step the qubits are acted on by the potential of the system. $\hat{\mathcal{C}}$ is the heart of the QLG method and in section [3.4] we will present the main collision operator that will be utilized throughout this dissertation. Lastly the streaming step moves the updated qubits to their nearest neighbor. This is done to recover the ∇^2 operator through finite difference.

3.2 Square Root of Swap

We begin with a universal 2-qubit CNOT gate.

$$\hat{\mathcal{C}}_{\text{CNOT}} = \begin{pmatrix} 1 & 0 & 0 & 0 \\ 0 & 1 & 0 & 0 \\ 0 & 0 & 0 & 1 \\ 0 & 0 & 0 & 1 \end{pmatrix}$$

If the first qubit is in state $|0\rangle$, then $\hat{\mathcal{C}}_{\text{CNOT}}$ leaves the second qubit unchanged. But if the first qubit is in state $|1\rangle$, then $\hat{\mathcal{C}}_{\text{CNOT}}$ will flip the second qubit (i.e. apply the Pauli spin operator σ_x). Thus $\hat{\mathcal{C}}_{\text{CNOT}}$ has the following mapping, $|00\rangle \rightarrow |00\rangle$, $|01\rangle \rightarrow |01\rangle$, but $|10\rangle \rightarrow |11\rangle$, $|11\rangle \rightarrow |10\rangle$. One can generate our entangled Bell state $|\Phi^+\rangle$ from an initial qubit state $|00\rangle$ by first applying the 1-qubit Hadamard gate to the 1st qubit and then the CNOT 2-qubit gate using the 1st qubit as control. That is

$$\begin{aligned} H|00\rangle &= (H|0\rangle) \otimes |0\rangle = \left(\frac{|0\rangle + |1\rangle}{\sqrt{2}} \right) \otimes |0\rangle \\ \hat{\mathcal{C}}_{\text{CNOT}} \left(\frac{|00\rangle + |10\rangle}{\sqrt{2}} \right) &= \left(\frac{|00\rangle + |11\rangle}{\sqrt{2}} \right) = |\Phi^+\rangle \end{aligned}$$

The CNOT gate entangles the qubits and it can be shown from quantum information theory that is a universal gate.

The first iteration of QLG employed the square-root of swap ($\sqrt{\text{SWAP}}$) collision oper-

ator,

$$\hat{\mathcal{C}}_{\sqrt{\text{SWAP}}} = \begin{pmatrix} \frac{1-i}{2} & \frac{1+i}{2} \\ \frac{1+i}{2} & \frac{1-i}{2} \end{pmatrix} \quad (3.7)$$

Equation [3.7] is actually a sub-block of the 2-qubit gate, its full matrix form is

$$\hat{\mathcal{C}}_{\sqrt{\text{SWAP}}} = \begin{pmatrix} 1 & 0 & 0 & 0 \\ 0 & \frac{1-i}{2} & \frac{1+i}{2} & 0 \\ 0 & \frac{1+i}{2} & \frac{1-i}{2} & 0 \\ 0 & 0 & 0 & 1 \end{pmatrix}$$

This operator is called the Square-Root-of-Swap since upon squaring it,

$$\left(\hat{\mathcal{C}}_{\sqrt{\text{SWAP}}}\right)^2 = \begin{pmatrix} 1 & 0 & 0 & 0 \\ 0 & 0 & 1 & 0 \\ 0 & 1 & 0 & 0 \\ 0 & 0 & 0 & 1 \end{pmatrix}$$

its action is to swap qubits, $|01\rangle \rightarrow |10\rangle$, $|10\rangle \rightarrow |01\rangle$, while $|00\rangle \rightarrow |00\rangle$, $|11\rangle \rightarrow |11\rangle$. Note that $\left(\hat{\mathcal{C}}_{\sqrt{\text{SWAP}}}\right)^4 = I_4$. It is convenient from now on to just consider the relevant sub-block, eq. [3.7], of the 4 x 4 unitary matrix. It can be shown that the square-root-of-swap is a universal gate in quantum information.

The accompanying streaming operator $\hat{\mathcal{S}}$ for our QLG algorithm is

$$\begin{aligned}\hat{\mathcal{S}}_{\pm\Delta x_i, q_1} &= \frac{1}{2}(1 - \sigma_z) + e^{\pm\Delta x_i \cdot \partial_{x_i}} \frac{1}{2}(1 + \sigma_z) = \begin{pmatrix} e^{\pm\Delta x_i \cdot \partial_{x_i}} & 0 \\ 0 & 1 \end{pmatrix} \\ \hat{\mathcal{S}}_{\pm\Delta x_i, q_2} &= \frac{1}{2}(1 + \sigma_z) + e^{\pm\Delta x_i \cdot \partial_{x_i}} \frac{1}{2}(1 - \sigma_z) = \begin{pmatrix} 1 & 0 \\ 0 & e^{\pm\Delta x_i \cdot \partial_{x_i}} \end{pmatrix}\end{aligned}\quad (3.8)$$

q_1 and q_2 in $\hat{\mathcal{S}}$ correspond to the relevant 2-qubits states, $|01\rangle$ and $|10\rangle$ respectively. Each qubit is streamed separately by a displacement of $\pm\Delta x_i$ along the i^{th} direction. Interleaving the non-commuting $\hat{\mathcal{C}}$ and $\hat{\mathcal{S}}$ operators leads to the evolution operator $\hat{\mathcal{U}}_{q_i}$

$$\hat{\mathcal{U}}_{q_i} = \hat{\mathcal{S}}_{-\Delta x_i, q_i} \hat{\mathcal{C}}_{\sqrt{\text{SWAP}}} \hat{\mathcal{S}}_{\Delta x_i, q_i} \hat{\mathcal{C}}_{\sqrt{\text{SWAP}}}, \quad i = 1, 2 \quad (3.9)$$

Note that eq. [3.9] is in 1D, extension to higher dimensions is straightforward by applying the evolution operator along the additional directions. $\hat{\mathcal{C}}_{\sqrt{\text{SWAP}}}$ does not contain the single-particle potential directly in the operator itself, instead we introduce any external potential into the required dynamics by invoking the unitary operator $\hat{\mathcal{U}}_v$,

$$\hat{\mathcal{U}}_v[V(x, t)] = e^{-i\Delta t V(x, t)} \quad (3.10)$$

To recover Schrödinger's equation with potential $V(x, t)$ one moves from qubit space to

standard wave functions by a simple zeroth order moment

$$\psi(x, t) = q_1(x, t) + q_2(x, t) \quad (3.11)$$

To initiate the quantum lattice algorithm we first encode the given initial wave function onto the qubit pairs, typically $q_1(x, 0) = q_2(x, 0) = \psi(x, 0)/2$. There seems to be no reason to introduce unnecessary asymmetry into the problem. The qubit pairs at each lattice site are then entangled by the unitary collision square-root-of-swap operator and that entanglement is spread throughout the lattice by the unitary streaming operator. Thus the time advancement from $t \rightarrow t + \Delta t$ is accomplished by the following sequence of unitary operators

$$\begin{pmatrix} q_1(x, t + \Delta t) \\ q_2(x, t + \Delta t) \end{pmatrix} = \hat{U}_{q_2}^2 \hat{U}_v \left[V \left(x, t + \frac{\Delta t}{2} \right) / 2 \right] \hat{U}_{q_1}^2 \hat{U}_v [V(x, t)/2] \begin{pmatrix} q_1(x, t) \\ q_2(x, t) \end{pmatrix} \quad (3.12)$$

To recover the Gross-Pitaevskii equation that describes the ground state wave function evolution of a BEC state, we will define the potential $V(x, t) = |\psi(x, t)|^2$. The $V(x, t + \Delta t/2)$ indicates that we need to use the updated wave function at this step. It should also be noted that if the unitary collision and unitary streaming operators commuted then $\hat{U}_{q_i}^2 = I_2$. Thus the evolution in eq.[3.12] is a perturbation expansion away from the unitary operator. Once $q_1(x, t + \Delta t)$ and $q_2(x, t + \Delta t)$ are determined we perform a Chapman-Enskog approximation on the time evolved qubits. That is we Taylor expand each qubit, and afterward Taylor expand again the sum of the qubits $q_1(x, t + \Delta t) + q_2(x, t + \Delta t)$. The resulting equation of

motion is

$$\begin{aligned}
 q_1(x, t + \Delta t) + q_2(x, t + \Delta t) &= (1 - i\Delta x^2 V(x, t) + i\Delta x^2 \partial_{xx}) (q_1(x, t) + q_2(x, t)) + \mathcal{O}[\Delta x^4] \\
 \psi(x, t + \Delta t) &= \psi(x, t) - i\Delta x^2 V(x, t)\psi(x, t) + i\Delta x^2 \partial_{xx}\psi(x, t) + \mathcal{O}[\Delta x^4]
 \end{aligned}
 \tag{3.13}$$

In the second line of eq. [3.13] we simply replaced the qubit sums with the wavefunction since that is how we set-up our problem. Subtracting $\psi(x, t)$ from both sides and dividing by Δt gives us the first time derivative in the limit $\Delta t \rightarrow 0$ and sets the diffusion ordering of the problem to

$$\Delta t = \Delta x^2 \tag{3.14}$$

Multiplying both sides of eq. [3.13] by the complex i recovers Schrödinger's equation with an arbitrary scalar potential $V(x, t)$. There is a $1/2$ term missing in front of the ∇^2 operator but that is easily recoverable through either rescaling, or by setting $\Delta x^2 = 1/2$. Thus only if the local entangling gate structure (i.e. quantum algorithmic protocol) is chosen appropriately, then the flow of quantum information can emulate, in the long wavelength limit, a quantum wave function governed by an equation of motion such as the Weyl, Dirac, or Schrödinger wave equation¹². The theory does not tell us the parameter regime in which we are modeling a physical equation as opposed to simply multiplying matrices. These parameters depend on the physics of a system, they can be an amplitude of some structure, the velocity of the system, a diffusion gradient or simply the interaction strength of some internal potential. If these values are too large we will find ourselves in a regime where our Chapman-Enskog

approximation is no longer valid, and in turn neither is our simulation. One way to identify that we are in the right parameter regime when modeling a system is to ensure that its conserved quantities are indeed conserved.

A number of successes have been realized with the $\hat{\mathcal{C}}_{\sqrt{\text{SWAP}}}$ collision operator which were mentioned in Chapter [1], but ultimately there is an upper limit to the potential interaction strengths present in $V(x, t)$ that it can be applied to. In the next section we present the relativistic operator that will be the basis for the new collision operator that is more capable than $\hat{\mathcal{C}}_{\sqrt{\text{SWAP}}}$.

3.3 Relativistic Dirac collision operator

A new relativistic collision operator, $\hat{\mathcal{C}}_{rel}$, was derived by Yopez¹³ for Dirac particles in 1+1 dimensions (time and space).

$$\hat{\mathcal{C}}_{rel} = \frac{1}{\gamma} \begin{pmatrix} \sqrt{\gamma^2 - \text{Sin}^2(\gamma ml)} & -ie^{-iml\sqrt{\gamma^2-1}}\text{Sin}(\gamma ml) \\ -ie^{iml\sqrt{\gamma^2-1}}\text{Sin}(\gamma ml) & \sqrt{\gamma^2 - \text{Sin}^2(\gamma ml)} \end{pmatrix} \quad (3.15)$$

γ is the Lorentz factor, $\gamma = \frac{1}{\sqrt{1-\beta^2}}$ with $\beta = \frac{v^2}{c^2}$, m is the mass of the particle, and l is the distance between lattice nodes. We are interested in the non-relativistic version of $\hat{\mathcal{C}}_{rel}$, but before getting there we present the derivation of $\hat{\mathcal{C}}_{rel}$ as it is the basis for the non-relativistic collision operator which is the main topic of this thesis. At the same time the derivation will give readers an idea of how these collision operators come about.

Following the procedure in the paper¹³ we begin with two unitary operators, specifically we take two arbitrary rotation operators (eq. [3.4]) that will act on our qubits.

$$\begin{aligned} U_1 &= e^{-i\frac{\beta_1}{2}\vec{n}_1\cdot\vec{\sigma}} \\ U_2 &= e^{-i\frac{\beta_2}{2}\vec{n}_2\cdot\vec{\sigma}} \end{aligned} \quad (3.16)$$

$\beta_{1,2}$ are small angles of rotations and $\vec{n}_{1,2}$ are unit vectors along the axis of rotation. Taylor expanding $U_{1,2}$ about the small angles and using the identities, $\sigma_i^2 = I_2$ and $(\vec{n}_1\cdot\vec{\sigma})\cdot(\vec{n}_1\cdot\vec{\sigma}) = \vec{n}_1\cdot\vec{n}_1 + i(\vec{n}_1\times\vec{n}_1)\cdot\vec{\sigma} = 1 + i0 = 1$, we rewrite our two rotation operators as

$$\begin{aligned} U_1 &= \text{Cos}\left(\frac{\beta_1}{2}\right)I_2 - i\vec{n}_1\cdot\vec{\sigma}\text{Sin}\left(\frac{\beta_1}{2}\right) \\ U_2 &= \text{Cos}\left(\frac{\beta_2}{2}\right)I_2 - i\vec{n}_2\cdot\vec{\sigma}\text{Sin}\left(\frac{\beta_2}{2}\right) \end{aligned} \quad (3.17)$$

In essence we have been able to sum the Taylor series to all orders because of the idempotent property of the Pauli spin operators. Taking the composition of U_2U_1 ,

$$\begin{aligned} U_2U_1 &= \left\{ \text{Cos}\left(\frac{\beta_1}{2}\right) - i\vec{n}_1\cdot\vec{\sigma}\text{Sin}\left(\frac{\beta_1}{2}\right) \right\} \left\{ \text{Cos}\left(\frac{\beta_2}{2}\right) - i\vec{n}_2\cdot\vec{\sigma}\text{Sin}\left(\frac{\beta_2}{2}\right) \right\} \\ &= \text{Cos}\left(\frac{\beta_1}{2}\right)\text{Cos}\left(\frac{\beta_2}{2}\right) - i\vec{n}_1\cdot\vec{\sigma}\text{Sin}\left(\frac{\beta_1}{2}\right)\text{Cos}\left(\frac{\beta_2}{2}\right) - i\vec{n}_2\cdot\vec{\sigma}\text{Cos}\left(\frac{\beta_1}{2}\right)\text{Sin}\left(\frac{\beta_2}{2}\right) \\ &\quad - (\vec{n}_2\cdot\vec{\sigma})(\vec{n}_1\cdot\vec{\sigma})\text{Sin}\left(\frac{\beta_1}{2}\right)\text{Sin}\left(\frac{\beta_2}{2}\right) \end{aligned} \quad (3.18)$$

Using the previous identity $(\vec{n}_2\cdot\vec{\sigma})\cdot(\vec{n}_1\cdot\vec{\sigma}) = \vec{n}_2\cdot\vec{n}_1 + i(\vec{n}_2\times\vec{n}_1)\cdot\vec{\sigma}$ we rewrite the above

result as,

$$\begin{aligned}
U_2U_1 = & \text{Cos}\left(\frac{\beta_1}{2}\right)\text{Cos}\left(\frac{\beta_2}{2}\right) - i\vec{n}_1 \cdot \vec{\sigma}\text{Sin}\left(\frac{\beta_1}{2}\right)\text{Cos}\left(\frac{\beta_2}{2}\right) - i\vec{n}_2 \cdot \vec{\sigma}\text{Cos}\left(\frac{\beta_1}{2}\right)\text{Sin}\left(\frac{\beta_2}{2}\right) \\
& - (\vec{n}_2 \cdot \vec{n}_1 + i(\vec{n}_2 \times \vec{n}_1) \cdot \vec{\sigma})\text{Sin}\left(\frac{\beta_1}{2}\right)\text{Sin}\left(\frac{\beta_2}{2}\right)
\end{aligned} \tag{3.19}$$

At this point we will choose our streaming operator, U_2 , to be along the z-direction and the collision operator, U_1 , to be along a general direction. We further simplify the problem by taking \vec{n}_1 perpendicular to \vec{n}_2 thus $\vec{n}_1 \cdot \vec{n}_2 = 0$.

$$\begin{aligned}
\vec{n}_1 &= (\alpha, \beta, \gamma) \\
\vec{n}_2 &= (0, 0, 1) \\
\vec{\sigma} &= (\sigma_x, \sigma_y, \sigma_z)
\end{aligned} \tag{3.20}$$

There is a slight issue with our choice of the streaming and collision operator. If one has a Hamiltonian $\mathcal{H} = \text{K.E} + \text{V}$, the operators for K.E and V do not commute, thus $e^{\frac{it}{\hbar}(\text{K.E}+\text{V})} \neq e^{\frac{it}{\hbar}\text{K.E}}e^{\frac{it}{\hbar}\text{V}}$. Our composition is an approximation and a more accurate operator splitting approach using the Suzuki-Trotter decomposition will be presented in Chapter [6]. The choice of vectors in eq. [3.20] leads eq. [3.19] to become

$$\begin{aligned}
U_2U_1 = & \text{Cos}\left(\frac{\beta_1}{2}\right)\text{Cos}\left(\frac{\beta_2}{2}\right) - i(\alpha\sigma_x + \beta\sigma_y + \gamma\sigma_z)\text{Sin}\left(\frac{\beta_1}{2}\right)\text{Cos}\left(\frac{\beta_2}{2}\right) - i\sigma_z\text{Cos}\left(\frac{\beta_1}{2}\right)\text{Sin}\left(\frac{\beta_2}{2}\right) \\
& - (i(-\beta\sigma_x + \alpha\sigma_y))\text{Sin}\left(\frac{\beta_1}{2}\right)\text{Sin}\left(\frac{\beta_2}{2}\right)
\end{aligned} \tag{3.21}$$

Using Lie-Algebra of the Pauli matrices $[\sigma_i, \sigma_j] = \epsilon_{ijk}i\sigma_k$ we can rewrite eq. [3.21] as

$$\begin{aligned}
U_2U_1 = U_s^zU_c &= \text{Cos}\left(\frac{\beta_1}{2}\right)\text{Cos}\left(\frac{\beta_2}{2}\right) \\
&- i \left(\alpha\text{Sin}\left(\frac{\beta_1}{2}\right)\text{Cos}\left(\frac{\beta_2}{2}\right) - \beta\text{Sin}\left(\frac{\beta_1}{2}\right)\text{Sin}\left(\frac{\beta_2}{2}\right) \right) \sigma_x \\
&- i \left(\alpha\text{Sin}\left(\frac{\beta_1}{2}\right)\text{Sin}\left(\frac{\beta_2}{2}\right) + \beta\text{Sin}\left(\frac{\beta_1}{2}\right)\text{Cos}\left(\frac{\beta_2}{2}\right) \right) \sigma_y \\
&- i \left(\text{Cos}\left(\frac{\beta_1}{2}\right)\text{Sin}\left(\frac{\beta_2}{2}\right) + \gamma\text{Sin}\left(\frac{\beta_1}{2}\right)\text{Cos}\left(\frac{\beta_2}{2}\right) \right) \sigma_z
\end{aligned} \tag{3.22}$$

We want the above result in eq. [3.22] to match

$$\begin{aligned}
\implies 1 + \frac{icp_z\tau}{\hbar}\sigma_z - \frac{imc^2\tau}{\hbar}\sigma_x \\
p_z = -i\hbar\partial_z
\end{aligned} \tag{3.23}$$

The desire to match equations [3.22] and [3.23] is by construction. Similarly to the procedure for recovering Schrödinger's equation via the $\hat{C}_{\sqrt{\text{SWAP}}}$ operator, we want in the long wavelength limit to recover something of the form

$$\psi'(z) = \left(1 + \frac{icp_z\tau}{\hbar}\sigma_z - \frac{imc^2\tau}{\hbar}\sigma_x \right) \psi(z) \tag{3.24}$$

In order for equations [3.22] and [3.23] to match we impose the following conditions,

$$\alpha\text{Cos}\left(\frac{\beta_2}{2}\right)\text{Sin}\left(\frac{\beta_1}{2}\right) - \beta\text{Sin}\left(\frac{\beta_1}{2}\right)\text{Sin}\left(\frac{\beta_2}{2}\right) = \frac{mc^2\tau}{\hbar} \tag{3.25}$$

$$\alpha \text{Sin} \left(\frac{\beta_1}{2} \right) \text{Sin} \left(\frac{\beta_2}{2} \right) + \beta \text{Cos} \left(\frac{\beta_2}{2} \right) \text{Sin} \left(\frac{\beta_1}{2} \right) = 0 \quad (3.26)$$

$$\text{Cos} \left(\frac{\beta_1}{2} \right) \text{Sin} \left(\frac{\beta_2}{2} \right) + \gamma \text{Cos} \left(\frac{\beta_2}{2} \right) \text{Sin} \left(\frac{\beta_1}{2} \right) = -\frac{cp_z \tau}{\hbar} \quad (3.27)$$

$$\alpha^2 + \beta^2 + \gamma^2 = 1 \quad (3.28)$$

Starting with equation [3.26] we solve by inspection for α , β and γ

$$\alpha \text{Sin} \left(\frac{\beta_1}{2} \right) \text{Sin} \left(\frac{\beta_2}{2} \right) + \beta \text{Cos} \left(\frac{\beta_2}{2} \right) \text{Sin} \left(\frac{\beta_1}{2} \right) = 0$$

$$\alpha = \text{Cos} \left(\frac{\beta_2}{2} \right)$$

$$\beta = -\text{Sin} \left(\frac{\beta_2}{2} \right)$$

$$\gamma = 0 \quad (3.29)$$

Substituting the results in eq. [3.29] into eq. [3.25] we get,

$$\alpha \text{Cos} \left(\frac{\beta_2}{2} \right) \text{Sin} \left(\frac{\beta_1}{2} \right) - \beta \text{Sin} \left(\frac{\beta_1}{2} \right) \text{Sin} \left(\frac{\beta_2}{2} \right) = \frac{mc^2 \tau}{\hbar}$$

$$\text{Cos} \left(\frac{\beta_2}{2} \right) \text{Cos} \left(\frac{\beta_2}{2} \right) \text{Sin} \left(\frac{\beta_1}{2} \right) - \left(-\text{Sin} \left(\frac{\beta_2}{2} \right) \right) \text{Sin} \left(\frac{\beta_1}{2} \right) \text{Sin} \left(\frac{\beta_2}{2} \right) = \frac{mc^2 \tau}{\hbar}$$

$$\text{Cos} \left(\frac{\beta_2}{2} \right)^2 \text{Sin} \left(\frac{\beta_1}{2} \right) + \text{Sin} \left(\frac{\beta_2}{2} \right)^2 \text{Sin} \left(\frac{\beta_1}{2} \right) = \frac{mc^2 \tau}{\hbar} \quad (3.30)$$

$$\left(\text{Cos} \left(\frac{\beta_2}{2} \right)^2 + \text{Sin} \left(\frac{\beta_2}{2} \right)^2 \right) \text{Sin} \left(\frac{\beta_1}{2} \right) = \frac{mc^2 \tau}{\hbar}$$

$$\text{Sin} \left(\frac{\beta_1}{2} \right) = \frac{mc^2 \tau}{\hbar}$$

Substituting the results of eq. [3.29] and the final result in eq. [3.30] we can simplify eq.

[3.27].

$$\begin{aligned}
\text{Cos}\left(\frac{\beta_1}{2}\right)\text{Sin}\left(\frac{\beta_2}{2}\right) + \gamma\text{Cos}\left(\frac{\beta_2}{2}\right)\text{Sin}\left(\frac{\beta_1}{2}\right) &= -\frac{cp_z\tau}{\hbar} \\
\text{Cos}\left(\frac{\beta_1}{2}\right)\text{Sin}\left(\frac{\beta_2}{2}\right) &= -\frac{cp_z\tau}{\hbar} \\
\sqrt{1 - \text{Sin}\left(\frac{\beta_1}{2}\right)^2}\text{Sin}\left(\frac{\beta_2}{2}\right) &= -\frac{cp_z\tau}{\hbar} \\
\sqrt{1 - \left(\frac{mc^2\tau}{\hbar}\right)^2}\text{Sin}\left(\frac{\beta_2}{2}\right) &= -\frac{cp_z\tau}{\hbar} \\
\text{Sin}\left(\frac{\beta_2}{2}\right) &= \frac{\left(-\frac{cp_z\tau}{\hbar}\right)}{\sqrt{1 - \left(\frac{mc^2\tau}{\hbar}\right)^2}}
\end{aligned} \tag{3.31}$$

Equations [3.30] and [3.31] allow us to determine what the product $\text{Cos}\left(\frac{\beta_1}{2}\right)\text{Cos}\left(\frac{\beta_2}{2}\right)$ is.

$$\text{Cos}\left(\frac{\beta_1}{2}\right) = \sqrt{1 - \text{Sin}\left(\frac{\beta_1}{2}\right)^2} = \sqrt{1 - \left(\frac{mc^2\tau}{\hbar}\right)^2} \tag{3.32}$$

$$\text{Cos}\left(\frac{\beta_2}{2}\right) = \sqrt{1 - \text{Sin}\left(\frac{\beta_2}{2}\right)^2} = \sqrt{1 - \frac{\left(-\frac{cp_z\tau}{\hbar}\right)^2}{1 - \left(\frac{mc^2\tau}{\hbar}\right)^2}} \tag{3.33}$$

$$\begin{aligned}
\text{Cos}\left(\frac{\beta_1}{2}\right)\text{Cos}\left(\frac{\beta_2}{2}\right) &= \sqrt{1 - \left(\frac{mc^2\tau}{\hbar}\right)^2} \sqrt{1 - \frac{\left(-\frac{cp_z\tau}{\hbar}\right)^2}{1 - \left(\frac{mc^2\tau}{\hbar}\right)^2}} \\
&= \sqrt{\left\{1 - \left(\frac{mc^2\tau}{\hbar}\right)^2\right\} \left\{1 - \frac{\left(-\frac{cp_z\tau}{\hbar}\right)^2}{1 - \left(\frac{mc^2\tau}{\hbar}\right)^2}\right\}} \\
&= \sqrt{\left\{1 - \left(\frac{mc^2\tau}{\hbar}\right)^2\right\} \left\{\frac{1 - \left(\frac{mc^2\tau}{\hbar}\right)^2}{1 - \left(\frac{mc^2\tau}{\hbar}\right)^2} - \frac{\left(-\frac{cp_z\tau}{\hbar}\right)^2}{1 - \left(\frac{mc^2\tau}{\hbar}\right)^2}\right\}} \\
&= \sqrt{\left\{1 - \left(\frac{mc^2\tau}{\hbar}\right)^2\right\} \left\{\frac{1 - \left(\frac{mc^2\tau}{\hbar}\right)^2 - \left(-\frac{cp_z\tau}{\hbar}\right)^2}{1 - \left(\frac{mc^2\tau}{\hbar}\right)^2}\right\}} \tag{3.34} \\
&= \sqrt{1 - \left(\frac{mc^2\tau}{\hbar}\right)^2 - \left(-\frac{cp_z\tau}{\hbar}\right)^2} \\
&= \sqrt{1 - (m^2c^4 + c^2p_z^2) \frac{\tau^2}{\hbar^2}} \\
\text{Cos}\left(\frac{\beta_1}{2}\right)\text{Cos}\left(\frac{\beta_2}{2}\right) &= \sqrt{1 - \left(\frac{E\tau}{\hbar}\right)^2}
\end{aligned}$$

The last line in eq. [3.34] used the relation $E^2 = m^2c^4 + c^2p_z^2$. Putting all of the results from equations [3.29], [3.30], [3.31] and [3.34] into eq. [3.22] leads to the following QLG evolution operator

$$U_s^z U_c = \sqrt{1 - \left(\frac{E\tau}{\hbar}\right)^2} + \frac{iE\tau}{\hbar} \left(\frac{cp_z}{E} \sigma_z - \frac{mc^2}{E} \sigma_x \right) \tag{3.35}$$

We want to now determine the individual operators U_c and U_s^z . Given the result in eq. [3.35] we can define the rotation vector from \vec{n}_1 to \vec{n}_2 to be,

$$\hat{n}_{12} = -\frac{mc^2}{E} \hat{x} + \frac{cp_z}{E} \hat{z} \tag{3.36}$$

To help us deconstruct the composition of $U_s^z U_c$ we will take advantage of two identities.

First that $(\hat{n}_{12} \cdot \vec{\sigma})^2 = 1$, an involution.

$$\begin{aligned}
(\hat{n}_{12} \cdot \vec{\sigma})^2 &= \left(\left\{ -\frac{mc^2}{E} \sigma_x, 0, \frac{cp_z}{E} \sigma_z \right\} \cdot \{ \sigma_x, \sigma_y, \sigma_z \} \right)^2 \\
&= \left(-\frac{mc^2}{E} \sigma_x + \frac{cp_z}{E} \sigma_z \right)^2 \\
&= \left(\left(-\frac{mc^2}{E} \right)^2 \underbrace{\sigma_x^2}_1 - \underbrace{\left(\frac{mc^2}{E} \frac{cp_z}{E} \right)^2 \sigma_x \sigma_z - \left(\frac{cp_z}{E} \frac{mc^2}{E} \right) \sigma_z \sigma_x}_0 + \left(\frac{cp_z}{E} \right)^2 \underbrace{\sigma_z^2}_1 \right) \\
&= \frac{m^2 c^4 + c^2 p_z^2}{E^2} = \frac{E^2}{E^2} \\
&= 1
\end{aligned} \tag{3.37}$$

Second that $\text{Sin} [\text{ArcCos} (\sqrt{1 - x^2})] = x$. This identity is easily seen if one considers a right triangle with legs of length x , $\sqrt{1 - x^2}$ and a hypotenuse of length 1, draw it on paper to convince yourself :). With these two identities we can rewrite eq. [3.35] as a single unitary operator $U_{comp} = e^{-i \frac{\beta_{12}}{2} \hat{n}_{12} \cdot \vec{\sigma}}$, here $\frac{\beta_{12}}{2} = \text{Cos}^{-1} \left(\sqrt{1 - \left(\frac{E_T}{\hbar} \right)^2} \right)$. Below we demonstrate that

U_{comp} is equivalent to eq. [3.35], recall that $e^{i\theta\hat{n}\cdot\vec{\sigma}} = \text{Cos}(\theta) + i\hat{n}\cdot\vec{\sigma}\text{Sin}(\theta)$.

$$\begin{aligned}
U_{comp} &= e^{-i\frac{\beta_{12}}{2}\hat{n}_{12}\cdot\vec{\sigma}} = e^{-i\text{Cos}^{-1}\left(\sqrt{1-\left(\frac{E\tau}{\hbar}\right)^2}\right)\hat{n}_{12}\cdot\vec{\sigma}} \\
&= \text{Cos}\left[\text{ArcCos}\left(\sqrt{1-\left(\frac{E\tau}{\hbar}\right)^2}\right)\right] + i\hat{n}_{12}\cdot\vec{\sigma}\text{Sin}\left[\text{ArcCos}\left(\sqrt{1-\left(\frac{E\tau}{\hbar}\right)^2}\right)\right] \\
&= \text{Cos}\left[\text{ArcCos}\left(\sqrt{1-\left(\frac{E\tau}{\hbar}\right)^2}\right)\right] + i\left(-\frac{mc^2}{E}\sigma_x + \frac{cp_z}{E}\sigma_z\right)\text{Sin}\left[\text{ArcCos}\left(\sqrt{1-\left(\frac{E\tau}{\hbar}\right)^2}\right)\right] \\
&= \sqrt{1-\left(\frac{E\tau}{\hbar}\right)^2} + i\frac{E\tau}{\hbar}\left(-\frac{mc^2}{E}\sigma_x + \frac{cp_z}{E}\sigma_z\right)
\end{aligned} \tag{3.38}$$

Equation [3.38] is exactly the same as eq. [3.35]. Since the rotation angle $\hat{n}_{12}\cdot\vec{\sigma}$ is a scalar we will replace it with a length quantity l . Doing so will make it easier for us to separate U_s^z from its composition with U_c .

$$\begin{aligned}
U_s^z U_c &= e^{-ih_d/\hbar c} \\
h_d &= -cp_z\sigma_z + mc^2\sigma_x \\
\text{Cos}\left(\frac{El}{\hbar c}\right) &= \sqrt{1-\left(\frac{E\tau}{\hbar}\right)^2}
\end{aligned} \tag{3.39}$$

The particular choice above for the argument of the Cosine term will later allow us to

eliminate τ from our operator. From the last line in eq. [3.39] we solve for τ in terms of l .

$$\begin{aligned}
\text{Cos} \left(\frac{El}{\hbar c} \right) &= \sqrt{1 - \left(\frac{E\tau}{\hbar} \right)^2} \\
\sqrt{1 - \text{Sin} \left(\frac{El}{\hbar c} \right)^2} &= \sqrt{1 - \left(\frac{E\tau}{\hbar} \right)^2} \\
1 - \text{Sin} \left(\frac{El}{\hbar c} \right)^2 &= 1 - \left(\frac{E\tau}{\hbar} \right)^2 \\
\text{Sin} \left(\frac{El}{\hbar c} \right) &= \frac{E\tau}{\hbar}
\end{aligned} \tag{3.40}$$

Recall that U_s^z is simply the streaming operator that shifts the qubits of the Dirac field $\pm l$ units along the z-direction, that is

$$\begin{aligned}
U_s^z &= e^{ilk_z\sigma_z} = e^{l\sigma_z p_z} \\
p_z &= i\partial_z
\end{aligned} \tag{3.41}$$

Thus for $U_s^z = U_2 = e^{-i\frac{\beta_2}{2}\vec{n}_2 \cdot \vec{\sigma}}$ we know that $\frac{\beta_2}{2} = -lk_z$. With $\frac{\beta_2}{2}$ known, we proceed to write down U_c .

$$\vec{n}_1 = (\alpha, \beta, \gamma) = \left(\text{Cos} \left(\frac{\beta_2}{2} \right), -\text{Sin} \left(\frac{\beta_2}{2} \right), 0 \right) \tag{3.42}$$

$$\begin{aligned}
U_c &= U_1 = e^{-i\frac{\beta_1}{2}\vec{n}_1 \cdot \vec{\sigma}} \\
&= \text{Cos} \left(\frac{\beta_1}{2} \right) I_2 - i\vec{n}_1 \cdot \vec{\sigma} \text{Sin} \left(\frac{\beta_1}{2} \right) \\
&= \text{Cos} \left(\frac{\beta_1}{2} \right) I_2 - i \left(\text{Cos} \left(\frac{\beta_2}{2} \right) \sigma_x - \text{Sin} \left(\frac{\beta_2}{2} \right) \sigma_y \right) \text{Sin} \left(\frac{\beta_1}{2} \right)
\end{aligned} \tag{3.43}$$

We can factor out σ_x from the last line in eq. [3.43] using the relation $\sigma_x^{-1} = \sigma_x$

$$\begin{aligned}
U_c &= \text{Cos}\left(\frac{\beta_1}{2}\right)I_2 - i\sigma_x \left(\text{Cos}\left(\frac{\beta_2}{2}\right) - \text{Sin}\left(\frac{\beta_2}{2}\right)\sigma_x^{-1}\sigma_y \right) \text{Sin}\left(\frac{\beta_1}{2}\right) \\
&= \text{Cos}\left(\frac{\beta_1}{2}\right)I_2 - i\sigma_x \left(\text{Cos}\left(\frac{\beta_2}{2}\right) - \text{Sin}\left(\frac{\beta_2}{2}\right)\sigma_x\sigma_y \right) \text{Sin}\left(\frac{\beta_1}{2}\right) \\
&= \text{Cos}\left(\frac{\beta_1}{2}\right)I_2 - i\sigma_x \left(\text{Cos}\left(\frac{\beta_2}{2}\right) - i\text{Sin}\left(\frac{\beta_2}{2}\right)\sigma_z \right) \text{Sin}\left(\frac{\beta_1}{2}\right)
\end{aligned} \tag{3.44}$$

By now $\text{Cos}\left(\frac{\beta_2}{2}\right) - i\text{Sin}\left(\frac{\beta_2}{2}\right)\sigma_z = e^{-i\sigma_z\frac{\beta_2}{2}}$ should be a familiar relation to us. Replacing the last line in eq. [3.44] with its operator form

$$\begin{aligned}
U_c &= \text{Cos}\left(\frac{\beta_1}{2}\right)I_2 - i\sigma_x \left(e^{-i\sigma_z\frac{\beta_2}{2}} \right) \text{Sin}\left(\frac{\beta_1}{2}\right) \\
&= \sqrt{1 - \left(\frac{mc^2\tau}{\hbar}\right)^2} I_2 - i\frac{mc^2\tau}{\hbar}\sigma_x e^{-i\sigma_z\frac{\beta_2}{2}} \\
&= \sqrt{1 - \left(\frac{mc^2\tau}{\hbar}\right)^2} I_2 - i\frac{mc^2\tau}{\hbar}\sigma_x e^{-i\sigma_z lp_z}
\end{aligned} \tag{3.45}$$

Writing out $\left(i\frac{mc^2\tau}{\hbar}\sigma_x e^{-i\sigma_z lp_z}\right)$ in eq. [3.45] explicitly,

$$\begin{aligned}
i\frac{mc^2\tau}{\hbar}\sigma_x e^{-i\sigma_z lp_z} &= i\frac{mc^2\tau}{\hbar} \begin{pmatrix} 0 & 1 \\ 1 & 0 \end{pmatrix} e^{-i\sigma_z lp_z} = i\frac{mc^2\tau}{\hbar} \begin{pmatrix} 0 & 1 \\ 1 & 0 \end{pmatrix} e^{-i\sigma_z lk_z} \\
&= i\frac{mc^2\tau}{\hbar} \begin{pmatrix} 0 & 1 \\ 1 & 0 \end{pmatrix} \begin{pmatrix} e^{ilk_z} & 0 \\ 0 & e^{-ilk_z} \end{pmatrix} \\
&= i\frac{mc^2\tau}{\hbar} \begin{pmatrix} 0 & e^{-ilk_z} \\ e^{ilk_z} & 0 \end{pmatrix}
\end{aligned} \tag{3.46}$$

Substituting the last line in eq. [3.46] into eq. [3.45], U_c becomes

$$\begin{aligned}
 U_c &= \sqrt{1 - \left(\frac{mc^2\tau}{\hbar}\right)^2} I_2 - i\frac{mc^2\tau}{\hbar} \begin{pmatrix} 0 & e^{-ik_z} \\ e^{ik_z} & 0 \end{pmatrix} \\
 &= \begin{pmatrix} \sqrt{1 - \left(\frac{mc^2\tau}{\hbar}\right)^2} & -ie^{-ik_z} \frac{mc^2\tau}{\hbar} \\ -ie^{ik_z} \frac{mc^2\tau}{\hbar} & \sqrt{1 - \left(\frac{mc^2\tau}{\hbar}\right)^2} \end{pmatrix}
 \end{aligned} \tag{3.47}$$

We want to get rid of the τ dependence in the collision operator. We have the usual energy, mass, momentum relation and begin with the Lorentz factor,

$$\gamma \equiv \frac{E}{mc^2} \tag{3.48}$$

Note that the Lorentz factor γ in eq. [3.48] has nothing to do with the one used in the \vec{n}_1 vector.

$$E = \sqrt{(p_z c)^2 + (mc^2)^2} \Rightarrow p_z c = \sqrt{E^2 - (mc^2)^2} \tag{3.49}$$

Using equations [3.48] and [3.49] we can rewrite the momentum p_z in terms of the Lorentz

factor γ .

$$\begin{aligned}
 p_z c &= \sqrt{E^2 - (mc^2)^2} \\
 p_z c &= mc^2 \sqrt{\frac{E^2}{(mc^2)^2} - 1} \\
 p_z &= mc \sqrt{\frac{E^2}{(mc^2)^2} - 1} \\
 p_z &= mc \sqrt{\gamma^2 - 1} = \hbar k_z
 \end{aligned} \tag{3.50}$$

Recall that in eq. [3.40] we chose a particular form for the argument of the Cosine function. This is going to finally come into play here, we will rewrite the energy, mass and momentum relation with p_z replaced by its form in eq. [3.50].

$$\begin{aligned}
 E &= \sqrt{\left(mc\sqrt{\gamma^2 - 1}\right)^2 c^2 + (mc^2)^2} \\
 &= \sqrt{(mc)^2 (\gamma^2 - 1) c^2 + (mc^2)^2} \\
 &= \sqrt{(mc^2)^2 [(\gamma^2 - 1) + 1]} \\
 &= mc^2 \sqrt{\gamma^2 - 1 + 1} \\
 &= mc^2 \gamma
 \end{aligned} \tag{3.51}$$

Substituting the expression for energy from eq. [3.51] into eq. [3.40]

$$\begin{aligned}
\frac{E\tau}{\hbar} &= \text{Sin} \left(\frac{El}{\hbar c} \right) \\
\frac{mc^2\gamma\tau}{\hbar} &= \text{Sin} \left(\frac{mc\gamma l}{\hbar} \right) \\
\frac{mc^2\tau}{\hbar} &= \frac{1}{\gamma} \text{Sin} \left(\frac{mc\gamma l}{\hbar} \right)
\end{aligned} \tag{3.52}$$

The final line in eq. [3.52] allows us to eliminate τ from the collision operator in eq. [3.47].

$$\begin{aligned}
U_c &= \begin{pmatrix} \sqrt{1 - \left(\frac{mc^2\tau}{\hbar}\right)^2} & -ie^{-ik_z} \frac{mc^2\tau}{\hbar} \\ -ie^{ik_z} \frac{mc^2\tau}{\hbar} & \sqrt{1 - \left(\frac{mc^2\tau}{\hbar}\right)^2} \end{pmatrix} \\
&= \begin{pmatrix} \sqrt{1 - \left(\frac{1}{\gamma} \text{Sin} \left(\frac{mc\gamma l}{\hbar}\right)\right)^2} & -ie^{-ik_z} \frac{1}{\gamma} \text{Sin} \left(\frac{mc\gamma l}{\hbar}\right) \\ -ie^{ik_z} \frac{1}{\gamma} \text{Sin} \left(\frac{mc\gamma l}{\hbar}\right) & \sqrt{1 - \left(\frac{1}{\gamma} \text{Sin} \left(\frac{mc\gamma l}{\hbar}\right)\right)^2} \end{pmatrix} \\
&= \begin{pmatrix} \sqrt{\frac{\gamma^2}{\gamma^2} - \frac{1}{\gamma^2} \left(\text{Sin} \left(\frac{mc\gamma l}{\hbar}\right)\right)^2} & -ie^{-ik_z} \frac{1}{\gamma} \text{Sin} \left(\frac{mc\gamma l}{\hbar}\right) \\ -ie^{ik_z} \frac{1}{\gamma} \text{Sin} \left[\frac{mc\gamma l}{\hbar}\right] & \sqrt{\frac{\gamma^2}{\gamma^2} - \frac{1}{\gamma^2} \left(\text{Sin} \left[\frac{mc\gamma l}{\hbar}\right]\right)^2} \end{pmatrix} \\
&= \frac{1}{\gamma} \begin{pmatrix} \sqrt{\gamma^2 - \left(\text{Sin} \left(\frac{mc\gamma l}{\hbar}\right)\right)^2} & -ie^{-ik_z} \text{Sin} \left(\frac{mc\gamma l}{\hbar}\right) \\ -ie^{ik_z} \text{Sin} \left(\frac{mc\gamma l}{\hbar}\right) & \sqrt{\gamma^2 - \left(\text{Sin} \left(\frac{mc\gamma l}{\hbar}\right)\right)^2} \end{pmatrix} \\
U_c &= \frac{1}{\gamma} \begin{pmatrix} \sqrt{\gamma^2 - \text{Sin} \left(\frac{mc\gamma l}{\hbar}\right)^2} & -ie^{-ilmc\sqrt{\gamma^2-1}} \text{Sin} \left(\frac{mc\gamma l}{\hbar}\right) \\ -ie^{ilmc\sqrt{\gamma^2-1}} \text{Sin} \left(\frac{mc\gamma l}{\hbar}\right) & \sqrt{\gamma^2 - \text{Sin} \left(\frac{mc\gamma l}{\hbar}\right)^2} \end{pmatrix}
\end{aligned} \tag{3.53}$$

Taking natural units with $\hbar = c = 1$ finally recovers $\hat{\mathcal{C}}_{rel}$ in eq. [3.15]. Unlike for the $\hat{\mathcal{C}}_{\sqrt{\text{SWAF}}}$ operator, $\hat{\mathcal{C}}_{rel}$ has the potential term introduced via the relativistic mass, that is

$$m = m_{particle} + V(x, t).$$

3.4 Non-Relativistic Operator with Phase

We want the non-relativistic version of $\hat{\mathcal{C}}_{rel}$ since we intend to work with Schrödinger's equation and not Dirac's. Simply setting the Lorentz factor $\gamma = 1$ is insufficient, but we find that in addition introducing a phase angle θ to the arguments of Sine and Cosine functions allows us to recover the desired equation of motion.

$$\begin{aligned} \left(\hat{\mathcal{C}}_{rel}\right)_{lim \ \gamma \rightarrow 1} &\rightarrow \hat{\mathcal{C}} = \begin{pmatrix} \sqrt{1 - \text{Sin}^2(\theta + ml)} & -i\text{Sin}(\theta + ml) \\ -i\text{Sin}(\theta + ml) & \sqrt{1 - \text{Sin}^2(\theta + ml)} \end{pmatrix} \\ &= \begin{pmatrix} \text{Cos}(\theta + ml) & -i\text{Sin}(\theta + ml) \\ -i\text{Sin}(\theta + ml) & \text{Cos}(\theta + ml) \end{pmatrix} \end{aligned} \quad (3.54)$$

As mentioned previously the relativistic mass term served as a means to introduce the potential into the system, so we replace it with the potential involved in the problem. Also we set $l = 1$ lattice nodes. With these changes $\hat{\mathcal{C}}$ takes the form,

$$\hat{\mathcal{C}} = \begin{pmatrix} \text{Cos}[\theta + V(x, t)] & -i\text{Sin}[\theta + V(x, t)] \\ -i\text{Sin}[\theta + V(x, t)] & \text{Cos}[\theta + V(x, t)] \end{pmatrix} \quad (3.55)$$

With this collision operator $\hat{\mathcal{C}}$ in eq. [3.55], and the streaming operator in eq. [3.8], we now wish to construct an interleaved collide-stream sequence that when applied to a pair

of qubits will recover the desired equation of motion in the long wavelength limit given an appropriate θ . Taking $\theta = \frac{\pi}{4}$, we present the following collide-stream sequence

$$\begin{pmatrix} q_1(x, t + \Delta t) \\ q_2(x, t + \Delta t) \end{pmatrix} = \hat{\mathcal{S}}_{\Delta x_2} \hat{\mathcal{C}} \hat{\mathcal{S}}_{-\Delta x_1} \hat{\mathcal{C}} \hat{\mathcal{S}}_{\Delta x_2} \hat{\mathcal{C}} \hat{\mathcal{S}}_{-\Delta x_1} \hat{\mathcal{C}} \hat{\mathcal{S}}_{-\Delta x_2} \hat{\mathcal{C}} \hat{\mathcal{S}}_{\Delta x_1} \hat{\mathcal{C}} \hat{\mathcal{S}}_{-\Delta x_2} \hat{\mathcal{C}} \hat{\mathcal{S}}_{\Delta x_1} \hat{\mathcal{C}} \begin{pmatrix} q_1(x, t) \\ q_2(x, t) \end{pmatrix} \quad (3.56)$$

Equation [3.56] recovers a similar result as in eq. [3.13] (in 1D)

$$\psi(x, t + \Delta t) = \psi(x, t) - 8i\epsilon^2 V(x, t)\psi(x, t) + i\epsilon^2 \partial_{xx}\psi(x, t) + \mathcal{O}[\epsilon^4] \quad (3.57)$$

with the same diffusion ordering as eq. [3.14], and $\epsilon = \frac{\Delta x^2}{\Delta t}$. Note that to recover eq. [3.57] we went through the same Chapman-Enskog procedure as the one presented in Section [3.2] for the $\hat{\mathcal{C}}_{\sqrt{\text{SWAP}}}$ operator. Taking the first term on the right-hand side of eq. [3.57] and moving it to the left, dividing by Δt and multiplying by i gives us the desired form of our equation.

$$i \left(\frac{\psi(x, t + \Delta t) - \psi(x, t)}{\Delta t} \right) \Big|_{\lim \Delta t \rightarrow 0} \rightarrow i\partial_t \psi(x, t) = -\epsilon^2 \nabla^2 \psi(x, t) + 8\epsilon^2 V(x, t)\psi(x, t) + \mathcal{O}[\epsilon^4] \quad (3.58)$$

The glaring difference between equations [3.13] and [3.58] is the factor of 8 that appears next to the potential term. This 8 corresponds to the number of times the collision is applied, and can easily be resolved by dividing the potential term in $\hat{\mathcal{C}}$ by $c = 8$. Thus our final form

for the non-relativistic collision operator $\hat{\mathcal{C}}$ is

$$\hat{\mathcal{C}} = \begin{pmatrix} \text{Cos}[\frac{\pi}{4} + \frac{1}{c}V(x, t)] & -i\text{Sin}[\frac{\pi}{4} + \frac{1}{c}V(x, t)] \\ -i\text{Sin}[\frac{\pi}{4} + \frac{1}{c}V(x, t)] & \text{Cos}[\frac{\pi}{4} + \frac{1}{c}V(x, t)] \end{pmatrix} \quad (3.59)$$

$$c_{1D} = 8, \quad c_{2D} = 16, \quad c_{3D} = 24$$

All results presented in this dissertation will have come from the use of the collision operator $\hat{\mathcal{C}}$ in eq. [3.59]. $\hat{\mathcal{C}}$ is an upgraded version of the $\hat{\mathcal{C}}_{\sqrt{\text{SWAP}}}$ operator and is able to handle problems with stronger potential interactions. Still it has the same requirements in that the ϵ in eq. [3.57] must still be small enough in order for us to be in a parameter regime in which we are modeling a desired system. In the next chapter we present QLG simulation results using $\hat{\mathcal{C}}$ for various potentials.

CHAPTER 4

QLG Simulation Results

4.1 1D Quantum Harmonic Oscillator

The first system we consider is the simple quantum harmonic oscillator (SHO). It is a simple well known problem with analytic stationary solutions. Our goal is to demonstrate that the QLG algorithm can preserve the stationary state of the system (thus the density and energy is conserved as well). The Hamiltonian for a quantum SHO¹⁵ is,

$$\hat{H} = \frac{\hat{p}^2}{2m} + \frac{1}{2}m\omega^2\hat{x}^2 \quad (4.1)$$

where ω is the frequency of oscillation, and m is the mass of the system. \hat{H} has well known Hermit polynomial solutions

$$\begin{aligned}\Psi_n(x) &= \frac{1}{\sqrt{2^n n!}} \left(\frac{m\omega}{\pi\hbar}\right)^{1/4} e^{-m\omega x^2/2\hbar} H_n\left(\sqrt{\frac{m\omega}{\hbar}}x\right), n = 0, 1, 2, \dots \\ H_n(x) &= (-1)^n e^{x^2} \frac{d^n}{dx^n}(e^{-x^2})\end{aligned}\tag{4.2}$$

Above n is an integer corresponding to the number of nodes in the system. In our simulations we set $\hbar = 1$ for computational simplicity. The important parameters here are the mass and the frequency ω , as they determine the amplitude of the system. The quantized energy levels are given by,

$$E_n = \hbar\omega \left(n + \frac{1}{2}\right), n = 0, 1, 2, \dots\tag{4.3}$$

Because the only potential present in this problem, is the external harmonic potential, the collision operator

$$\hat{C} = \begin{pmatrix} \text{Cos}\left[\frac{\pi}{4} + \frac{1}{8}\left(\frac{1}{2}m\omega^2x^2\right)\right] & -i\text{Sin}\left[\frac{\pi}{4} + \frac{1}{8}\left(\frac{1}{2}m\omega^2x^2\right)\right] \\ -i\text{Sin}\left[\frac{\pi}{4} + \frac{1}{8}\left(\frac{1}{2}m\omega^2x^2\right)\right] & \text{Cos}\left[\frac{\pi}{4} + \frac{1}{8}\left(\frac{1}{2}m\omega^2x^2\right)\right] \end{pmatrix}$$

for this example is constant in time. As was explained in Chapter [3] we encode the initial condition in two qubits $q_1(x, t)$ and $q_2(x, t)$. How this encoding is achieved on a classical computer is somewhat arbitrary. One can choose for example to set the initial qubits at $t = 0$ as $q_1(x, 0) = \psi(x, 0)$, $q_2(x, 0) = 0$. The collision operator will populate q_2 during the collision step and the system would evolve without complications. We always choose

to split the wavefunction among the two qubits evenly, that is $q_1(x, 0) = \frac{1}{2}\psi(x, 0)$ and $q_2(x, 0) = \frac{1}{2}\psi(x, 0)$, this will be the assumed encoding scheme throughout the dissertation. Once the qubits are encoded, we act on them by the collide-stream sequence presented in eq. [3.56], which after completing constitutes one iteration. Below figures [4.1a], [4.1b] and [4.1c] illustrate excellent agreement between the analytic and QLG results for various n values, over 10^6 iterations. The choice of ω is simply taken to be such that the wavefunction spans

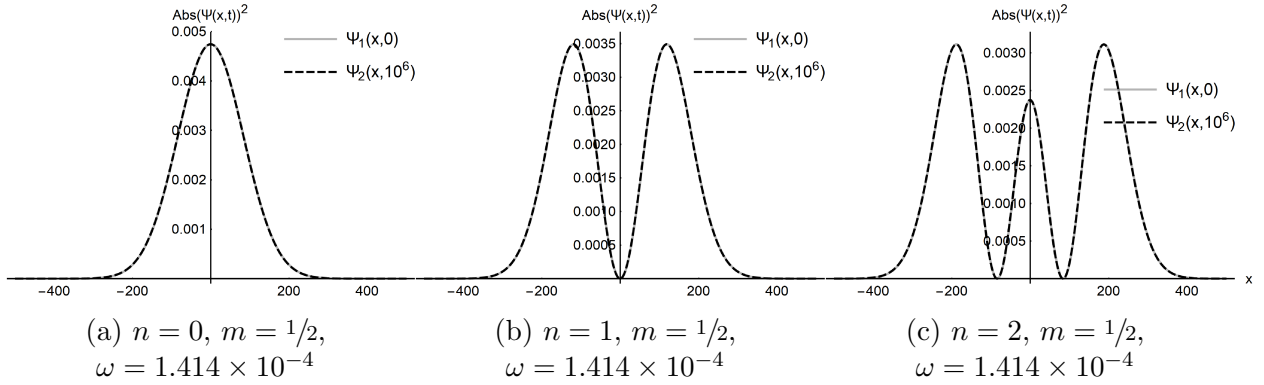


FIG: 4.1 Simulation results for SHO ground state and first two excited states.

a significant portion of the grid $L = 1000$. Figure [4.2] shows the deviation of the QLG solution from the analytic solution after $t = 10^6$ iterations, averaged over the grid L .

4.2 Bright Solitons

The one dimensional GP equation (eq. [2.18]) is also known as the Non-Linear *Schrödinger* (NLS) equation that describes propagation of light in a nonlinear optical fiber.

$$i\partial_t\psi = -\partial_x^2\psi + \beta g|\psi|^2\psi \quad (4.4)$$

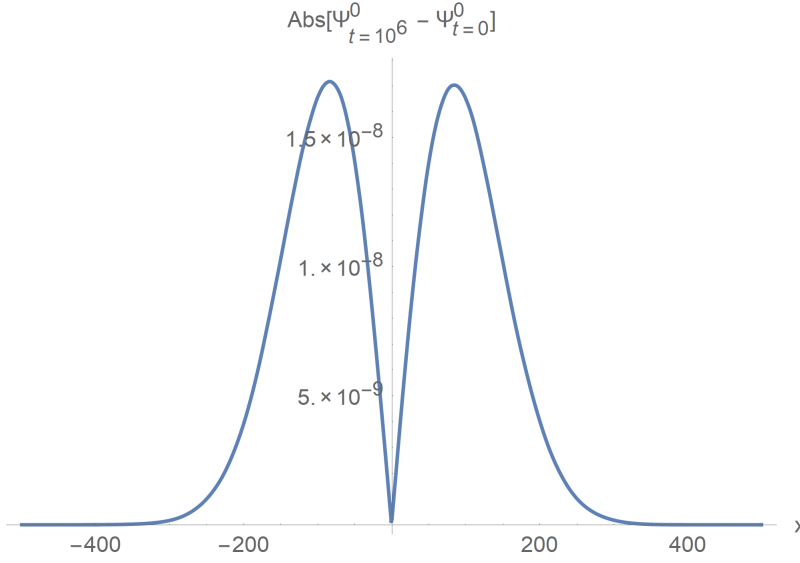


FIG. 4.2: The deviation of the QLG solution after $t = 10^6$ iterations from its analytic counterpart for the case $n = 0$ shown in Fig. [4.1a].

$\beta = \pm 1$ depending on whether a_s is positive or negative. The scattering length, a_s , can be tuned by the magnetic field and the harmonic trap applied on the BEC¹⁶. NLS captures the interplay between the dispersive properties of a medium and the non-linear interaction which results in localized wavepackets that propagate without distortion. When the non-linear interaction is negative ($\beta = -1$) the interaction is attractive and the wavepackets are called bright-solitons. Eq. [4.4] has an infinite number of conserved moments, for us the relevant ones are the normalization of the system,

$$N(t) := \int_{\mathbb{R}} |\psi(x, t)|^2 dx, \quad t \geq 0 \quad (4.5)$$

energy,

$$E(t) := \frac{1}{2} \int_{\mathbb{R}} [|\partial_x \psi(x, t)|^2 + \beta g |\psi(x, t)|^4] dx, \quad t \geq 0 \quad (4.6)$$

and momentum

$$P(t) := \frac{i}{2} \int_{\mathbb{R}} [\psi(x, t) \partial_x \psi^\dagger(x, t) - \psi^\dagger(x, t) \partial_x \psi(x, t)] dx, \quad t \geq 0 \quad (4.7)$$

Eq. [4.4] admits the well-known bright-soliton solution^{17,18},

$$\psi(x, t) = \sqrt{2}\alpha \text{Sech}[\alpha(x - \beta t)] e^{i(\beta/2)x - (\beta^2/4 - \alpha^2)t} \quad (4.8)$$

In eq. [4.8], α is the amplitude of the soliton, and β is its velocity. This analytic solution makes the NLS a good test bed for the QLG algorithm. While the presence of solitons in optical fibers has been observed for some time, bright solitons were first created in the BEC in 2002 by K. E. Strecker et. al.¹⁹ using ⁷*Li*. Their BEC had $N \sim 6 \times 10^3$. As noted earlier, the solitons propagate without distortion, this means their amplitudes and velocities will remain unchanged. However an interesting feature is that when two solitons pass through each other they undergo a phase shift²⁰. We shall demonstrate that QLG is able to capture all of these features of the NLS problem. The form of the collision operator for the NLS problem and our choice of β is

$$\hat{c} = \begin{pmatrix} \text{Cos}[\frac{\pi}{4} - \frac{1}{8}(g|\psi|^2)] & -i\text{Sin}[\frac{\pi}{4} - \frac{1}{8}(g|\psi|^2)] \\ -i\text{Sin}[\frac{\pi}{4} - \frac{1}{8}(g|\psi|^2)] & \text{Cos}[\frac{\pi}{4} - \frac{1}{8}(g|\psi|^2)] \end{pmatrix}$$

Our potential term is no longer constant unlike for the SHO problem. An important factor is keeping the potential current, that is after every streaming step, before applying the collision

on the qubits we update the potential term in the collision operator with its latest streamed value. Taking a domain $L = 6,000$ grid points with periodic boundary conditions, $\alpha_1 = 0.31$, $\alpha_2 = 0.17$ and velocities $\beta_1 = 0.5$, $\beta_2 = -0.5$ (lattice units)/(time step). The two soliton system is described by the initial condition

$$\psi(x, t = 0) = 0.44 \text{Sech} [0.31(x - L/6)] e^{i(0.5/2)(x - L/6)} + 0.25 \text{Sech} [0.17(x - 5L/6)] e^{i(-0.5/2)(x - 5L/6)} \quad (4.9)$$

The spatial resolution is $\Delta x = 1$ lattice points, and thus $\Delta t = 1$ as well (due to the diffusion ordering in eq. [3.14]). The solitons are well separated by about 4000 lattice points with the larger amplitude soliton moving to the right, while the lower amplitude soliton to the left. The first collision occurs at around $t = 40k$, Figure [4.3] displays the results over 8×10^5 iterations in a 10^6 iteration run. With periodic boundary conditions the solitons travel in a closed loop, upon reaching the boundary from either direction, they translate to the boundary on the other and continue their motion.

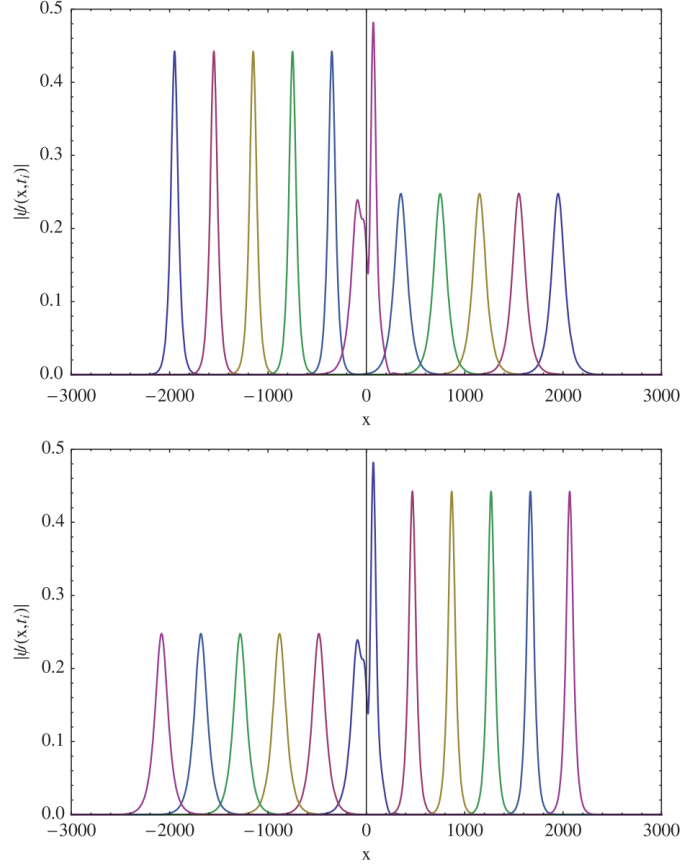


FIG. 4.3: Snapshot of $|\psi(x, t_i)|$ at 8000 time intervals ($\Delta t = 8k$) for (*top*) pre-collision and (*bottom*) post-collision soliton motion. Initially, the larger soliton has its peak around $x \sim -2000$ while the smaller soliton has its peak around $x \sim +2000$. Color scheme for (*top*): blue ($t = 0$) \rightarrow red ($t = 8k$) \rightarrow brown ($t = 16k$) \rightarrow green ($t = 24k$) \rightarrow blue ($t = 32k$) \rightarrow red-overlap ($t = 40k$). Color scheme for (*bottom*): blue-overlap ($t = 40k$) \rightarrow red ($t = 48k$) \rightarrow brown ($t = 56k$) \rightarrow green ($t = 64k$) \rightarrow blue ($t = 72k$) \rightarrow red ($t = 80k$). The large amplitude soliton always moves to the right while the lower amplitude soliton always moves to the left under periodic boundary conditions. Soliton overlap/collision occurs at $t = 40k$. Note that the solitons move with the same amplitude and speed pre- and post-collision.

After the 15th soliton-soliton collision, we see a spatial shift in the location of the soliton due to a collision-induced phase shift, but the solitons retain their exact shape and speed, Figure [4.4].

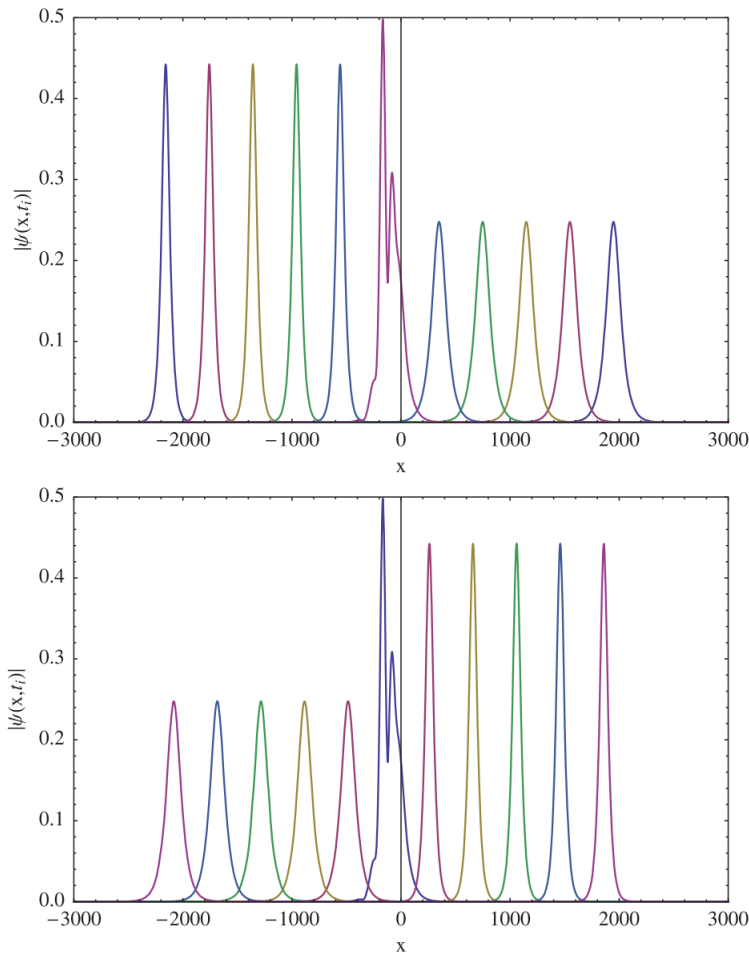


FIG. 4.4: Snapshot of $|\psi(x, t_i)|$ at time intervals of $(\Delta t = 8k)$ for the post-15th collision. Initial time instant for these six snap-shots is $t = 832k$ with the larger soliton peak at around $x \sim -2200$, and the smaller peak at $x \sim +1950$: (*top*) pre-15th collision and (*bottom*) post-15th collision soliton motion. The color scheme is the same as in Figure [4.2].

In Figure [4.5], we plot the time development of the collision-induced spatial shift in the larger soliton. After every soliton-soliton collision, this spatial shift is +18 lattice units. Since the soliton retains its exact form and speed post-collision there is no spatial shift in-between

collisions. Hence, the staircase structure in Figure [4.5]. The Gibbs-like jaggedness during the soliton-soliton collision time is a numerical artifact of the algorithm that simply spits out the location of the maximum in $|\psi|$. During the soliton-soliton collision, this peak location is not necessarily the location of the individual soliton that one has been following before the collision.

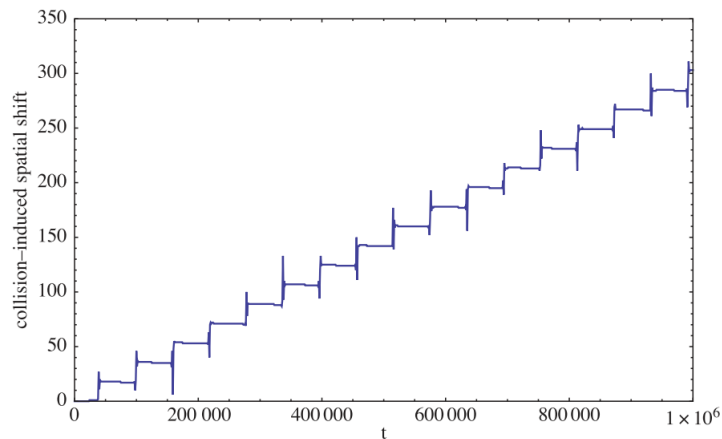


FIG. 4.5: The time evolution of the collision-induced spatial phase shifts in the larger soliton with speed $\beta = 0.5$ lattice units/time step. The spatial shift in-between soliton-soliton collisions is basically a constant, as expected theoretically for soliton-soliton collisions of 1D NLS. The Gibbs-like spikes that appear during the soliton-soliton overlap collision is a numerical artifact on the use of the peak in $|\psi|$ during the collision.

Lastly we look at the energy of the system, presented in Figure [4.6] There are two things to note about the energy in Figure [4.6]. First, the energy is negative due to the rescaling applied on the system. A soliton's width is determined by its amplitude and when the amplitude is relatively high it becomes quite narrow. One can increase the spatial resolution in order to resolve the soliton in enough detail, or rescale the system. Increasing spatial resolution, by setting $\Delta x < 1$ requires an increased number of data points, and due to the diffusion ordering, has an additional requirement in that a greater amount of iterations are

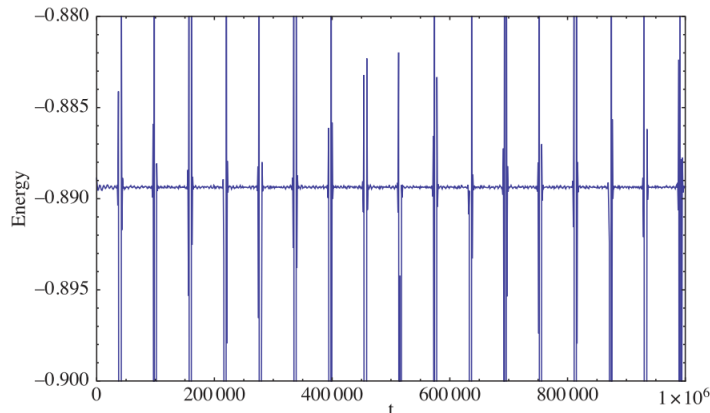


FIG. 4.6: The time evolution of the energy integral, a constant of the motion of the 1D NLS Hamiltonian system. For the chosen parameters, $E_{const.} = -0.889$. The Gibbs-like spikes that appear during the soliton-soliton overlap collision are numerical artifacts related to the stencil used to calculate Equation [4.6]

needed to reach the same point in time. While in 1D more iterations is not a significant factor, in higher dimensions (especially 3D) it can be more significant. Rescaling on the other hand does not add additional computation time, but does increase the second term in eq. [4.6], resulting in a negative energy. The second thing to note in Figure [4.6] are the oscillations that occur during collisions. These oscillations are a numerical artifact due to the simple finite difference method used to calculate the first derivative in eq. [4.6]. During the collision the wavefunction has some large gradients which can be smoothed out with a higher spatial resolution, but as mentioned previously this adds considerable computation time. Another way to manage the oscillations is presented by Dellar²¹, where one can estimate the energy integral as the expectation value of the Hamiltonian.

It must be stressed that in the QLG mesoscopic algorithm there is no knowledge of the existence of the constant energy integral of 1D NLS. It is only if we have chosen the simulation QLG parameters such that the subsequent moment equations (in this case the

1D NLS equation) arise from diffusion ordering with the existence of the needed theoretical perturbation parameter ϵ . If one sets the amplitude of the soliton too high, or the velocity too fast, a breakdown occurs that is readily apparent in the loss of energy and density conservation within the simulation.

4.3 Vector Solitons

We next consider a slightly more complicated scenario of an optical fiber that is birefringent, with a single-mode fiber permitting two orthogonal polarizations: the so-called O-mode which has a constant refractive index along its ray path, while the X-mode has a refractive index that varies along its ray path. It has been shown²² that the slowly varying amplitudes of these modes can be determined from the 1D coupled-NLS equations,

$$\begin{aligned} i\partial_t Q_1 &= -\partial_{xx} Q_1 - 2\mu \{ |Q_1|^2 + B|Q_2|^2 \} Q_1 \\ i\partial_t Q_2 &= -\partial_{xx} Q_2 - 2\mu \{ |Q_2|^2 + B|Q_1|^2 \} Q_2 \end{aligned} \tag{4.10}$$

with $\mu > 0$, and B is the cross-phase birefringence modulation coefficient, $2 \leq 3B \leq 6$. We will be looking at the specific case of $B = 1$ for which it has been shown that the coupled NLS equations [4.10] are completely integrable^{22,23,24} and are known as the Manakov equations.

Exact 2-vector soliton solutions for the Manakov system in eqs. [4.10] are

$$\begin{aligned} Q_1(x, t) &= \sum_{n=1}^2 \frac{1}{2} \alpha_n \operatorname{sech} \left[\operatorname{Re}(\eta_n) + \frac{1}{2} R_n \right] e^{-1/2 + i \operatorname{Im}(\eta_n)} \\ Q_2(x, t) &= \sum_{n=1}^2 \frac{1}{2} \beta_n \operatorname{sech} \left[\operatorname{Re}(\eta_n) + \frac{1}{2} R_n \right] e^{-1/2 + i \operatorname{Im}(\eta_n)} \end{aligned} \quad (4.11)$$

α_n , β_n and k_n are arbitrary complex parameters with ($n = 1, 2$)

$$\begin{aligned} \eta_n &= k_n(x - x_{0n} + i k_n t) \\ R_n &= L n \left[\frac{\mu(|\alpha_n|^2 + |\beta_n|^2)}{4 \operatorname{Re}(k_n)^2} \right] \end{aligned} \quad (4.12)$$

For each propagating mode, the (real) parameters x_{0n} predominantly determine the location of the soliton peaks if the two solitons are non-overlapping, while $\operatorname{Re}(k_n)$ predominantly dictate the individual soliton amplitudes and $\operatorname{Im}(k_n)$ the soliton speeds. The asymptotic post-collision vector soliton solutions have been evaluated^{22,23,24} for when the solitons are non-overlapping. In particular for $\operatorname{Re}(k_n) > 0$, the post-collision non-overlapping two-soliton amplitudes are given by (where 'r' denotes post-collision state properties)

$$\begin{aligned} \frac{\alpha'_1}{\beta'_1} &= \left(\left[1 - g + \left| \frac{\alpha_1}{\beta_1} \right|^2 \right] \frac{\alpha_2}{\beta_2} \right) \left(g \frac{\alpha_1^*}{\beta_1^*} \frac{\alpha_2}{\beta_2} + (1 - g) \left| \frac{\alpha_1}{\beta_1} \right|^2 + 1 \right)^{-1} \\ \frac{\alpha'_2}{\beta'_2} &= \left(\left[1 - h + \left| \frac{\alpha_2}{\beta_2} \right|^2 \right] \frac{\alpha_1}{\beta_1} \right) \left(h^* \frac{\alpha_2^*}{\beta_2^*} \frac{\alpha_1}{\beta_1} + (1 - h^*) \left| \frac{\alpha_2}{\beta_2} \right|^2 + 1 \right)^{-1} \end{aligned} \quad (4.13)$$

with

$$\begin{aligned} g(k_1, k_2) &= \frac{2\text{Re}(k_1)}{k_2 + k_1^*} \\ h(k_1, k_2) &= \frac{2\text{Re}(k_2)}{k_2^* + k_1} \end{aligned} \tag{4.14}$$

Radhakrishnan et. al.²² showed analytically that for certain values of parameters there exist inelastic vector soliton solutions, that is in a vector soliton collision, one of the soliton pairs in a particular polarization is annihilated. This type of inelastic collision is impossible in scalar NLS theory because of the normalization constraint

$$\int dx |Q_i(x, t)|^2 = \text{const}, \quad i = 1, 2 \tag{4.15}$$

Unlike previous systems we've looked at, the vector soliton solutions are comprised of two coupled wave-functions. Thus far we have only worked with one, and the change we make to accommodate both is simply using two qubit pairs, alongside two collision operators. That is we will encode $Q_i(x, t)$ in qubit pairs (q_{1_i}, q_{2_i}) , $i = 1, 2$ respectively. The systems are coupled by their interaction which appear directly in the collision operators, thus they maintain constant knowledge of how the system evolves. Each step of the collide-stream sequence is applied simultaneously to each wavefunction, while keeping the potential values

current after every streaming operation.

$$Q_1(q_{1_1}, q_{2_1}) = \begin{pmatrix} q_{1_1}(x, t) \\ q_{2_1}(x, t) \end{pmatrix}$$

$$Q_2(q_{1_2}, q_{2_2}) = \begin{pmatrix} q_{1_2}(x, t) \\ q_{2_2}(x, t) \end{pmatrix}$$

$$\hat{C}^{Q_1} = \begin{pmatrix} \text{Cos}[\frac{\pi}{4} + \frac{1}{8}(2\mu|Q_1|^2 + B|Q_2|^2)] & -i\text{Sin}[\frac{\pi}{4} + \frac{1}{8}(2\mu|Q_1|^2 + B|Q_2|^2)] \\ -i\text{Sin}[\frac{\pi}{4} + \frac{1}{8}(2\mu|Q_1|^2 + B|Q_2|^2)] & \text{Cos}[\frac{\pi}{4} + \frac{1}{8}(2\mu|Q_1|^2 + B|Q_2|^2)] \end{pmatrix}$$

$$\hat{C}^{Q_2} = \begin{pmatrix} \text{Cos}[\frac{\pi}{4} + \frac{1}{8}(2\mu|Q_2|^2 + B|Q_1|^2)] & -i\text{Sin}[\frac{\pi}{4} + \frac{1}{8}(2\mu|Q_1|^2 + B|Q_2|^2)] \\ -i\text{Sin}[\frac{\pi}{4} + \frac{1}{8}(2\mu|Q_2|^2 + B|Q_1|^2)] & \text{Cos}[\frac{\pi}{4} + \frac{1}{8}(2\mu|Q_2|^2 + B|Q_1|^2)] \end{pmatrix}$$

Figure [4.7] shows a simulation of an inelastic vector-soliton collision for 2-soliton pairs ($|Q_1(x, t)|$ in blue, and $|Q_2(x, t)|$ in red), at pre-collision and post-collision time. At $t = 0$, the vector 2-soliton pairs are centered around $x = 900$ and $x = 5000$. For specially chosen initial parameters, there is an inelastic collision as is seen in the disappearance of the soliton in the post-collision state of $|Q_1(x, t)|$ that is propagating to the left (see the left plot of Fig. [4.7]). However, in the subsequent soliton collisions the amplitudes will no longer satisfy the criterion ($\alpha'_1 = 0$, $\alpha'_2 \neq 0$) for an inelastic collision, and the $|Q_1(x, t)|$ 2-solitons will reappear. In Fig. [4.8] we plot the time evolution of the 2-soliton maxima (i.e. the $\max_{1 \leq x \leq L} |Q_n(x, t)|$, $n = 1, 2$) throughout the run (here $t_{max} = 400K$). The higher amplitude soliton is shown dashed, to distinguish it from the lower amplitude soliton. The spikes in the

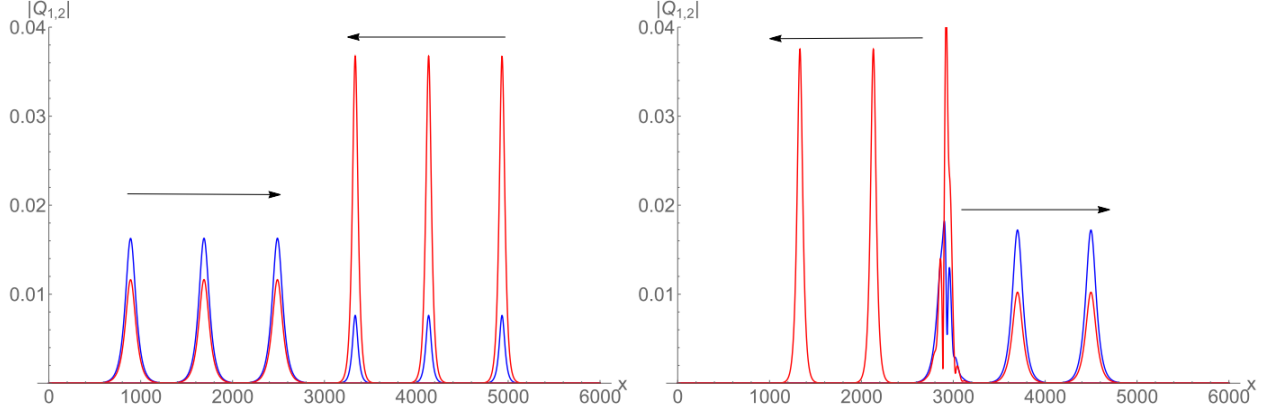


FIG. 4.7: The collisional evolution of Manakov solitons left figure. The pre-collision states at $t = 0$, $t = 10K$, $t = 20K$ while the post-collision states right figure are at times $t = 25K$, $t = 35K$, $t = 45K$. The first polarization amplitude 2-soliton $|Q_1(x, t)|$ is in blue, while the orthogonal polarization 2-soliton $|Q_2(x, t)|$ is in red. The inelastic soliton collision occurs for specially chosen soliton amplitudes and speeds, and in this case the post-collision soliton for $|Q_1(x, t)| = 0$ for $x < 3000$ is totally absent. Simulations performed on a grid $L = 6000$, under periodic boundary conditions.

peaks occur during soliton-soliton overlap. The inelastic collision, resulting in the loss of the lower amplitude soliton in $|Q_1|$ is clearly seen after the 1st soliton-soliton collision around $t = 25K$, see also Fig. [4.7], but it reappears after the 2nd soliton-soliton collision. In the time intervals between soliton-soliton collisions the four soliton shape, amplitude and speed remains invariant as can be seen in Fig. [4.7] and Fig. [4.8]. There is no second inelastic vector soliton-soliton collision in $|Q_1|$, although around $t = 330K$ the secondary soliton peak is quite low, $|Q_1| \sim 2 \times 10^{-4}$.

4.4 Dark Solitons

The last 1D system we're going to look at are dark solitons, the case where $\beta = +1$ in eq. [4.4]. Unlike the bright soliton, dark soliton interaction is repulsive, our goal is to set

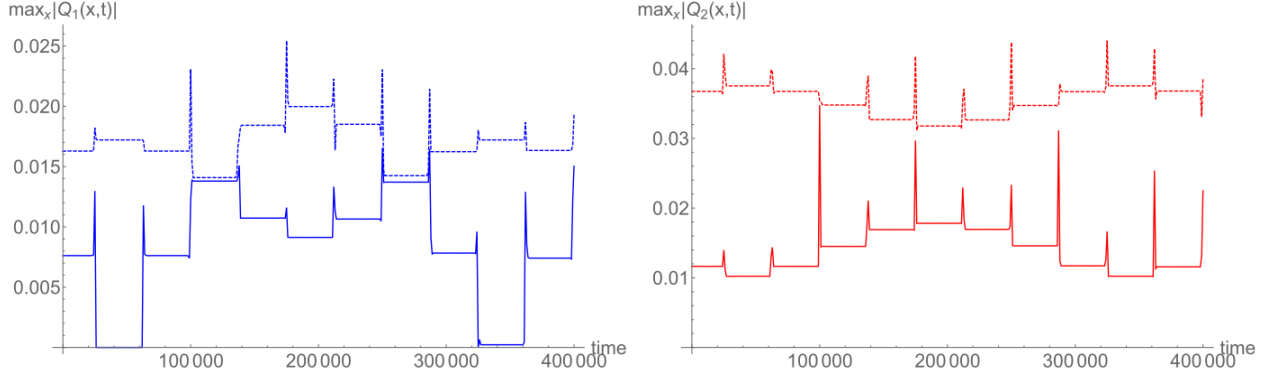


FIG. 4.8: A plot of the time evolution of the vector 2-soliton peaks, $\max_{1 \leq x \leq L} |Q_n(x, t)|$, $n = 1, 2$, in each mode. Vector soliton-soliton collisions occur whenever the peaks spike. For the parameters chosen, an inelastic Manakov soliton collision occurs only for $t = 24K$, with the subsequent loss of one of the solitons. This soliton reappears following the next vector soliton-soliton overlap collision. The dashed curves are for the higher amplitude soliton within that particular mode, while the solid curve is for the lower soliton amplitude. For the integrable Manakov system the vector 2-soliton solution exhibits invariant soliton properties away from the collisional overlap regions: i.e., the constant horizontal sections indicate the non-overlapping soliton spatial regions.

the velocity of the solitons low enough so as to observe this behavior. If the velocity is too high, the solitons will overcome the repulsion and pass through each other. There is a subtle difference in this case that makes it a slightly more challenging problem than bright solitons.

The solution to eq. [4.4] in the case of $\beta = +1$ is

$$\psi(x, t) = \frac{1}{\sqrt{2}} (2\alpha \text{Tanh} [\alpha(x + \beta t)] e^{-i/2(\beta^2 + 4\alpha^2)t}) \quad (4.16)$$

β is the velocity of the soliton, while α is its depth. For dark solitons the asymptote of the wavefunction at the boundary is non-zero and thus periodic boundary-conditions can no longer be employed as that would result in a phase discontinuity across the boundary²⁵.

Instead we employ Neumann boundary conditions, on an interval $[-L, L]$

$$\begin{aligned}\psi'(-L, t) &= 0 \\ \psi'(L, t) &= 0\end{aligned}\tag{4.17}$$

With ψ' denoting the first spatial derivative of the wavefunctions. This means that our simulation is limited to the domain spanned by our grid, and whenever a soliton reaches the boundary, the simulation become unphysical and effectively ends. Additionally multiple solitons must have the same speed and depth (in contrast to the bright-soliton case) in order to ensure continuity of $\psi(x, t)$. It is somewhat difficult to convey soliton pass-through versus bouncing-off each other using still images. The main distinguishing feature of the two processes is the soliton overlap, during pass-through the solitons will undergo a complete overlap while during a bounce they will only experience a partial overlap before changing direction. Figure [4.9] displays a simulation of two dark solitons as they approach and pass through each other on a grid of length $L = 3000$. An almost complete overlap is seen at time $t = 3.94 \times 10^4$ and sometime later at $t = 6 \times 10^4$ the solitons have passed through each other and maintain their original shapes. In figure [4.10] we present a simulation in which the soliton speeds are slow enough that their kinetic energy cannot overcome the repulsive interaction. Upon collision the solitons reverse direction and bounce off each other. Because of the slower speeds we consider a smaller grid of length $L = 800$ to reduce the amount of time it takes for a collision to occur.

Figure [4.11a] demonstrates the effects of a soliton-boundary collision with three snap-

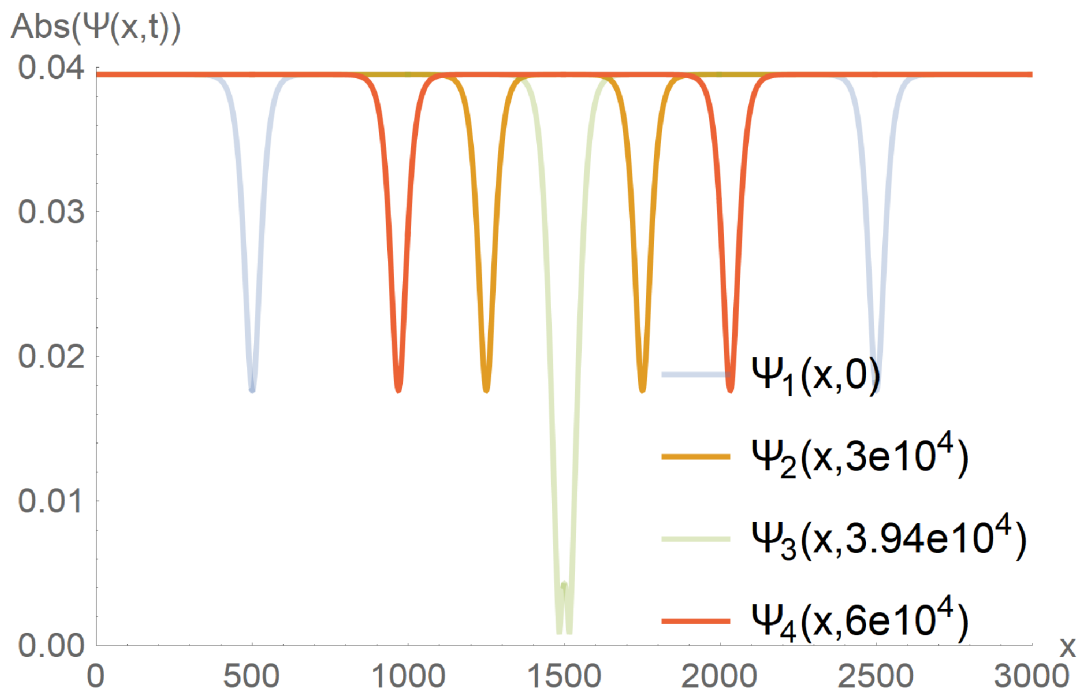


FIG. 4.9: Two dark solitons with an equal depth of $\alpha = 0.025$ and velocities $\beta = \pm 0.025$ lattice units/time step. At $t = 0$ the left soliton is moving to the right and the right soliton is moving to the left. At $t = 3.94 \times 10^4$ we observe an almost complete overlap of the two solitons, and at $t = 6 \times 10^4$ they have passed through each other. The grid length $L = 3000$ with $\Delta x = 1$.

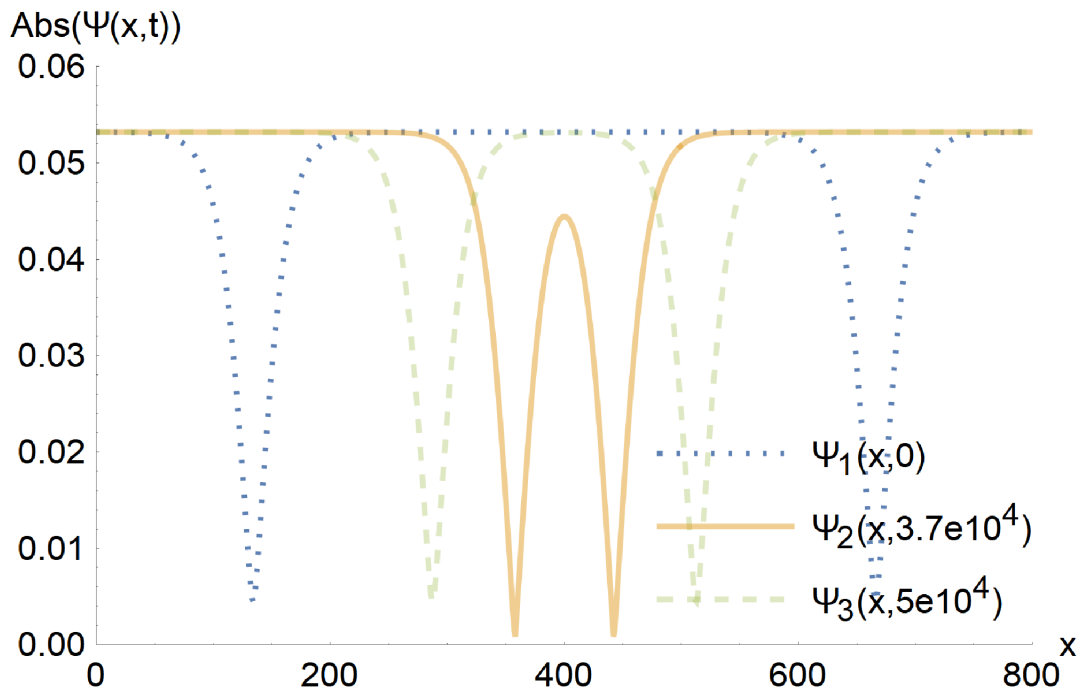
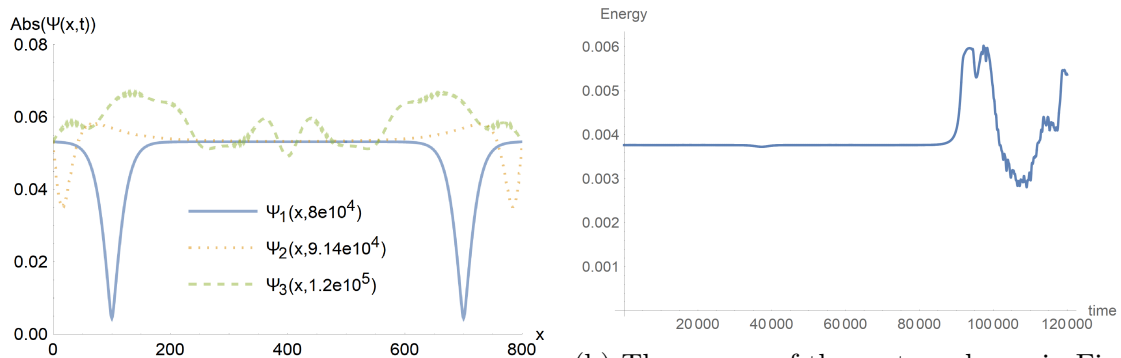


FIG. 4.10: Two dark solitons with an equal depth of $\alpha = 0.0375$ and velocities $\beta = \pm 0.00625$ lattice units/time step. At $t = 0$ the left soliton is moving to the right and the right soliton is moving to the left. At $t = 3.7 \times 10^4$ we observe the maximum partial overlap of the two solitons before their velocities change sign, and at $t = 5 \times 10^4$ the initial left (right) soliton is moving left (right). The grid length $L = 800$ with $\Delta x = 1$.

shots showcasing the solitons before, during and after the collision. During the soliton-boundary collision one sees the distortion of the wavefunction from its expected behavior and post collision at $t = 1.2 \times 10^5$ the wavefunction is completely distorted. Conservation of energy in the simulation can be seen in fig. [4.11b]. We show the energy before and after the solitons make contact with the boundary. Note that the energy is appropriately positive as no rescaling was applied to the system. Prior to the collision the energy curve is a horizontal line with a distortion during the collision at $t = 3.7 \times 10^4$, indicating good energy conservation. At $t = 8 \times 10^4$ the solitons make contact with the boundary of the grid rendering the simulation unphysical from that point forward. This is readily apparent in the almost immediate loss of energy conservation of the system. QLG only simulates eq.



(a) Three snapshots of the wavefunction at $t = 8 \times 10^4$ before a boundary collision, $t = 9.14 \times 10^4$ during the collision, and $t = 1.2 \times 10^5$ after a collision.

(b) The energy of the system shown in Fig. [4.9]. The bump seen at $t = 3.7 \times 10^4$ is when the soliton collision occurs, and at $t = 8 \times 10^4$ is when the solitons reach the boundary.

FIG: 4.11

[3.57] if we are within the bounds of the small parameters assumed for the Chapman-Enskog approximation, in this case that small parameter being velocity of the dark soliton. In fig. [4.12] we demonstrate what happens to the energy of a dark soliton system in which the

velocity is set too high. When we are not in the correct parameter regime to model the GP system there is a complete lack of energy conservation.

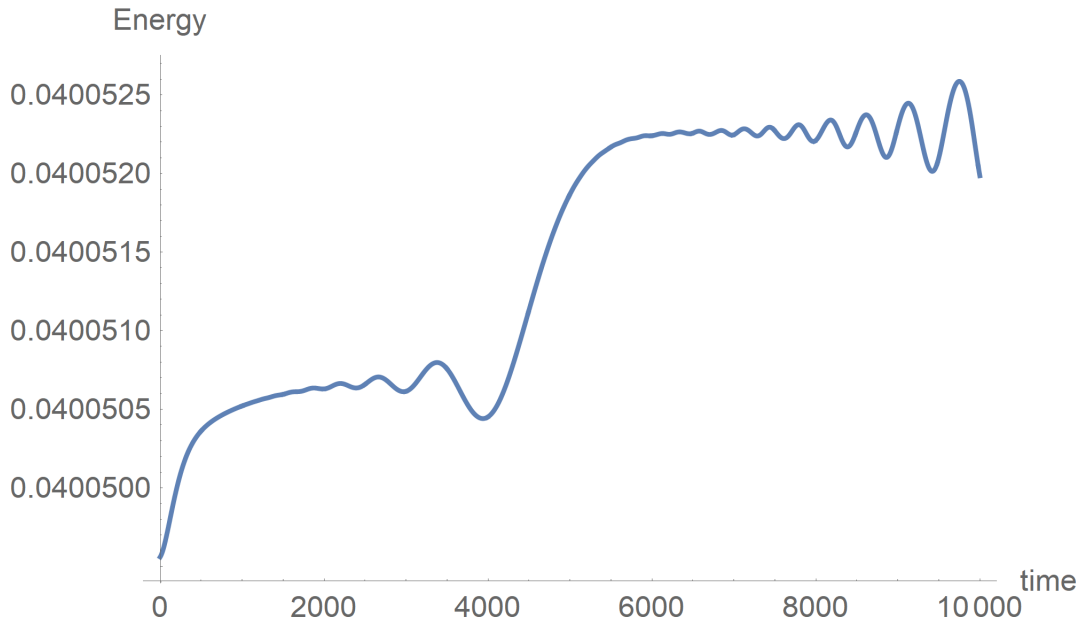


FIG. 4.12: Modeling dark solitons with velocity $\beta = 0.06875$ (lattice units)/(time step). This velocity is too high which is reflected in the lack of energy conservation throughout the simulation.

4.5 Vortex Rings

In this section we will consider the full scalar 3D GPE which unlike its 1D counterpart has no analytic solution.

$$2i\partial_t\psi = -\nabla^2\psi + (g|\psi|^2 - \mu)\psi \quad (4.18)$$

μ is the chemical potential of the system. Specifically we will look at vortex rings in a BEC gas along with vortex ring reconnection. Reconnection is a term used to describe topological changes in a system. It is a long standing problem in the study of fluids, notably present

in plasmas (solar flares, Earth’s magnetosphere, tokomaks). Despite the physical differences between a BEC and a classical thermal fluid, they exhibit many similar phenomena. Unlike in classical fluids vortex reconnection in the GP system is driven by the quantum pressure term (eq. [2.25]) that appears when we look at the hydrodynamic form of the GPE. For the scalar BEC, describable by a single GP eq. [4.18], the quantum vortex core is a topological line of zero density. The structure of a quantum vortex itself is typically quite local, away from which the wavefunction asymptotes, $\psi \rightarrow |\psi_\infty| = \text{const.}$ a small distance from the core, called the healing length ξ . For example, a typical quantum vortex in ^{87}Rb has a healing length $\xi \approx 4\mu\text{m}$. The vortex reconnection of line vortices has been considered in considerable detail by many authors²⁶. Here, following Baggaley²⁷, we shall consider the reconnection and topological changes of vortex rings.

The first step in the QLG algorithm is to encode a wavefunction into the qubit pair, thus our first task is to determine a suitable initial condition. We will work in polar coordinates because it simplifies the problem, and assume the system is symmetric about the z-axis. Considering a time-independent vortex-line solution of the form

$$\psi = R(r)e^{in\theta} \tag{4.19}$$

$$n = 1, \quad \text{winding number}$$

we substitute our solution in eq. [4.19] into eq. [4.18] which gives us an ODE in terms of $R(r)$.

$$\frac{1}{2} \left(R''(r) + \frac{R'(r)}{r} - \frac{R(r)}{r^2} \right) + (\mu - gR(r)^2) R(r) = 0 \tag{4.20}$$

We then consider a Páde approximation of the radial function $R(r)$. A Páde approximation employs the use of a rational polynomial to represent $R(r)$,

$$R(r)_M^N = \sqrt{\frac{\sum_{n=0}^N a_n r^n}{1 + \sum_{m=0}^M b_m r^m}} \quad (4.21)$$

$$M = N$$

The coefficients for a_n and b_m are determined through Berloff asymptotics at the boundaries.

$$\psi \rightarrow \sqrt{\frac{\mu}{g}} \text{ as } r \rightarrow \infty \quad (4.22)$$

We can approximate $R(r)$ with a finite set of a_m and b_n . The above procedure would provide us with vortex-line solutions, but we are interested in vortex-rings. Such an initial condition is presented by Baggaley²⁷, based on the straight line vortex determined by a Páde approximation. Starting with our Páde polynomial

$$R(r) = \sqrt{\frac{a_1 r^2 + a_2 r^4}{1 + b_1 r^2 + b_2 r^4}}$$

$$a_1 = \frac{11\mu^2}{32g} \quad (4.23)$$

$$b_1 = \frac{\mu}{3}$$

$$a_2 = b_2 = \frac{11\mu^2}{384g}$$

Our initial wavefunction at $t = 0$ is

$$\psi(x, t = 0) = \Psi(z, s + R_0)\Psi^*(z, s - R_0) \quad (4.24)$$

$$\Psi(z, s) = R \left(\sqrt{z^2 + s^2} \right) e^{i\theta} \quad (4.25)$$

In essence we are taking a line vortex and twisting it about an axis into a loop ($s^2 = x^2 + y^2$) of radius R_0 .

With an initial condition we are in a position to perform our simulation. In the non-relativistic collision operator, $V(x, t) = g|\psi|^2 - \mu$, and in 3D, $c = \frac{1}{24}$. The governing parameters for our system are μ and the parameter g which arises from the s-wave Bose-Bose interactions. Computationally it controls the BEC density, as for an isolated quantum vortex, $\psi \rightarrow \sqrt{\frac{\mu}{g}}$, can be readily seen from a Thomas-Fermi approximation of the scalar GPE in the limit of negligible kinetic energy (i.e., in the asymptotic region where the wavefunction has negligible spatial variations and we take $\nabla^2\psi \rightarrow 0$).

We first consider a choice of $\mu = 0.002$ and $g = 10^6$ on a 720^3 grid with an initial vortex ring radius $R_0 = 75$ (in our lattice units $\Delta x = \Delta t = 1$). An important detail is that we are using periodic boundary conditions in our simulation. The choice of these parameters was driven by the desire to perform a single fairly long run ($t_{max} = 92000$). Nearly all the reported simulations on vortex rings apply simple non-reflecting boundary conditions so that their simulations end when the vortex ring approaches the boundaries (as in our earlier discussion on the simulation of dark solitons). Here we wish to perform long time integration

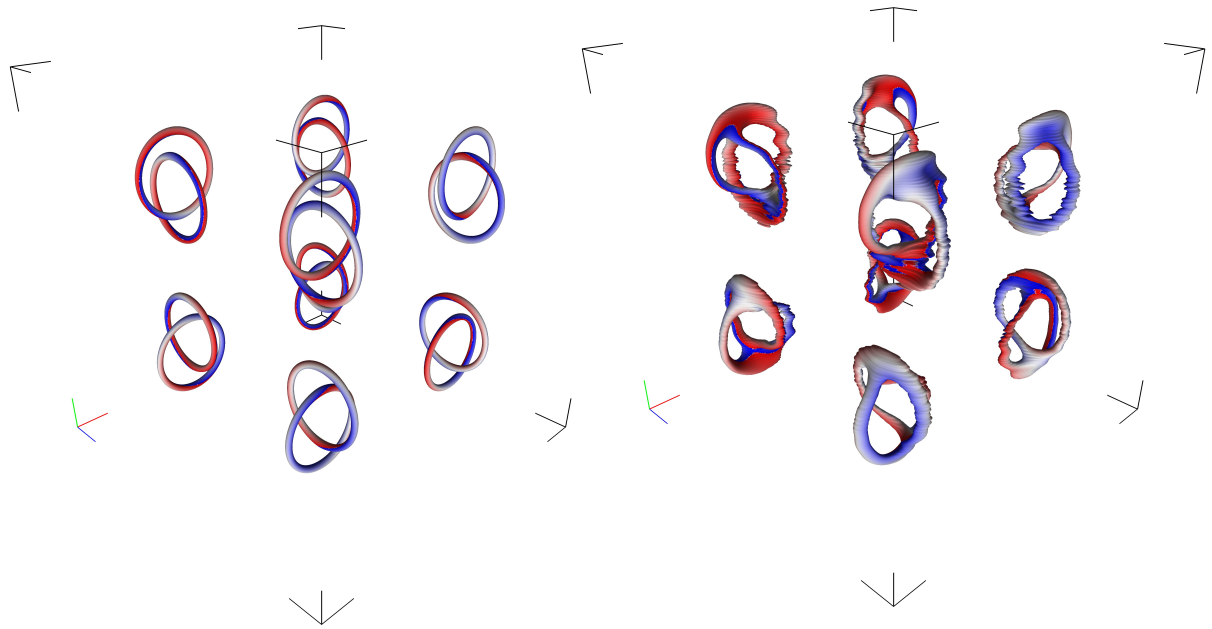
and vortex ring dynamics and so consider periodic boundary conditions. This will require us to set up an appropriate set of 8-ring vortices in 3D and adjust their phases so that we have periodicity on all boundary faces. Moreover we will be interested in the vortex Hopf link topology and how it evolves in time. Thus we will be concerned with interlocked vortex rings. In particular, we consider vortex rings that lie in the x-y plane which above $z = 0$ have a positive phase, and those below ($z < 0$) negative. In addition we have another set of 8 perpendicular vortex-rings in the y-z plane, for which the phase is positive for those above $x = 0$, and negative below ($x < 0$). Each vortex ring is its own wavefunction $\phi_i(\vec{x})$ defined in eq. [4.25], and our initial condition is the product of all vortex-rings, $\psi(\vec{x}, 0) = \prod \phi_i(\vec{x})$.

Our symplectic integration scheme preserves the Hamiltonian structure of the GPE which is seen quite clearly in vortex-ring simulations with very high g-factors. All Hamiltonians exhibit a Poincaré recurrence time, $t = T_{\text{Poincaré}}$, in which the system comes arbitrary close to its initial condition. However for continuous Hamiltonians this Poincaré recurrence is typically so long that it is rarely, if ever, observable. For the 3D GPE system, with initial straight line quantum vortices, it has been shown²⁸ that a system with very weak s-wave interactions exhibits a remarkably short Poincaré recurrence time which has a dependence on the grid size,

$$T_{\text{Poincaré}} = 0.159L_{\text{grid}}^2 \tag{4.26}$$

In our vortex ring simulations on a 720^3 grid this would result in $T_{\text{Poincaré}} = 82,612$ iterations, our simulation yields $T_{\text{Poincaré}} = 82,500$ (outputs step $\Delta t = 100$). As in the straight line quantum vortex case we also see the mirror inversion of the initial vortex-ring state at

$t = 0.5T_{\text{Poincaré}}$. Figures [4.13a] shows an isosurface of the initial wavefunction at low density and [4.13b] demonstrate the rapid onset of vortex-ring reconnection after just 500 time steps.



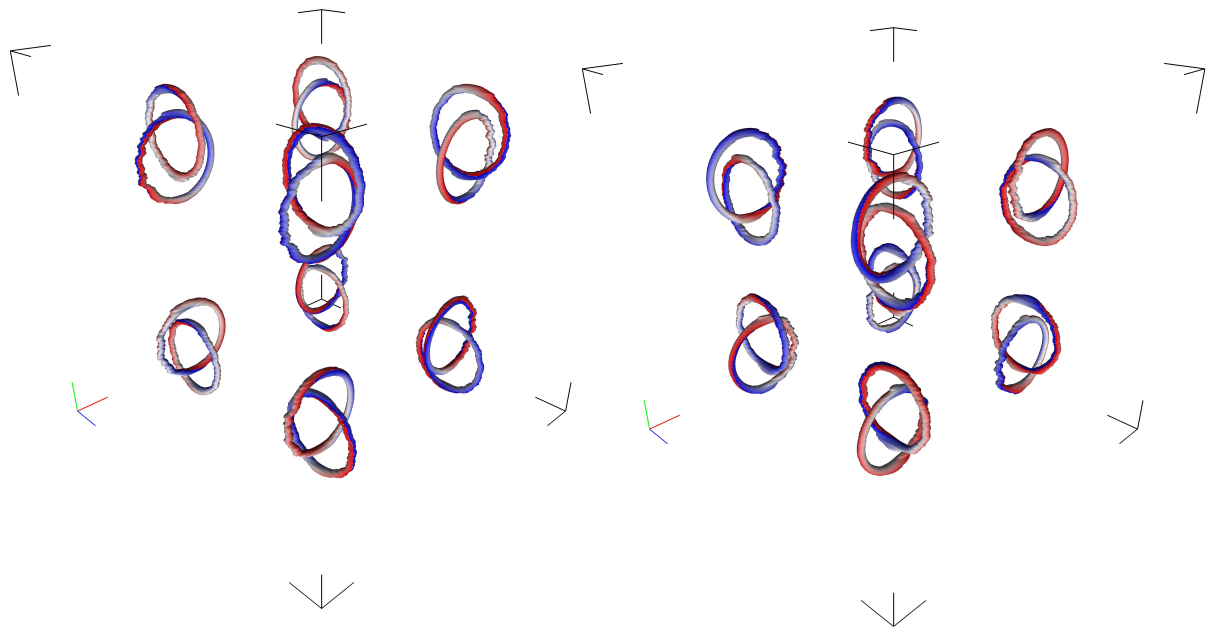
(a) An isosurface at low densities of the initial ($t = 0$) vortex-ring profile on a 720^3 grid. $\mu = 0.002$, $g = 10^6$ and $R_0 = 75$

(b) An isosurface with the same parameters as in fig. [4.13a] but at a later time. Vortex-ring reconnection is visible after just 500 time steps.

FIG: 4.13 Isosurfaces of vortex-rings

As expected in figures [4.14a] and [4.14b] we observe Poincaré recurrence at $t \approx 41,000$ and $t \approx 81,000$ respectively. Figure [4.14a] corresponds to $t = 0.5T_{\text{Poincaré}}$ during which the wavefunction is mirrored and in fig. [4.14b] we reach $t = T_{\text{Poincaré}}$. The entire simulation was ran for $90k$ iterations with an initial total energy of $E_0 = 8.717 \times 10^{-10}$ and a deviation of 0.007% from E_0 at the end of the run.

These results should be contrasted with those for strong s-wave interactions between



(a) An isosurface at low densities of the vortex-ring profile at $t = 41200$ on a 720^3 grid, displaying Poincaré recurrence. $\mu = 0.002$, $g = 10^6$ and $R_0 = 75$. Note how the profile is inverted relative to the initial profile in fig. [4.13a].

(b) An isosurface with the same parameters as in fig. [4.14a] but at a later time, $t = 81300$. During the second Poincaré recurrence our profile is reoriented to match the initial one in fig. [4.13a].

FIG: 4.14 Poincaré recurrence in vortex-ring simulations.

the bosons (i.e., for lower values of g). In these simulations the chemical potential $\mu = 0.004$, and $g = 3 \times 10^3$, our parameter is about 3 orders of magnitude greater. In this parameter regime we no longer observe Poincaré recurrence, that is $T_{\text{Poincaré}} \rightarrow \infty$. Figures [4.15a - 4.15f] demonstrate the results of the simulation with a total energy $E_0 = 6.257 \times 10^{-7}$ and a deviation of 0.013% in E_0 after 90k iterations, with the mean density conserved to 0.03%. As expected at $t = 400$ time-steps the vortex rings have reconnected, and subsequent iterations are followed by a destruction in that topology as seen in the vortex core isosurface plots. Furthermore the system does not exhibit Poincaré recurrence, at $0.5T_{\text{Poincaré}}$, comparing Fig. [4.15e] to Fig. [4.13a]. Similarly comparing Fig. [4.15f] to Fig. [4.13b] one sees a clear lack of Poincaré recurrence.

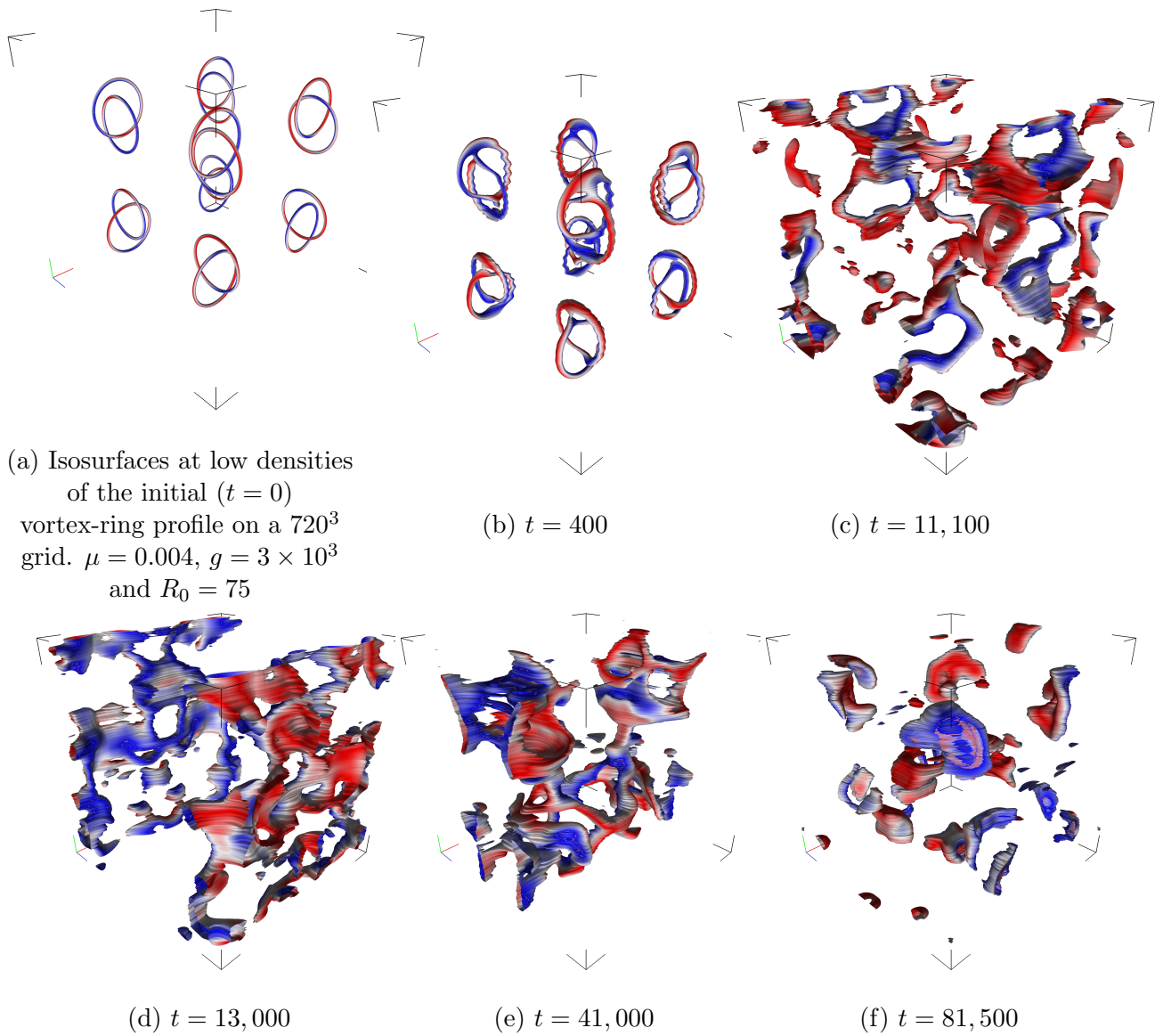


FIG: 4.15 Simulation of vortex-ring reconnection in a stronger interaction regime.

CHAPTER 5

Imaginary Time

5.1 Imaginary-Time Collision Operator

In Chapter [4] we saw that QLG requires a good initial condition in order to properly model a physical system. There are many techniques one can employ to find ground state solutions for quantum systems, one specifically being the Imaginary Time (IT) method. In IT the Schrödinger equation, and its non-linear generalization, is transformed into a diffusion equation using a Wicks rotation of time by $\pi/2$ in the complex plane: $t \rightarrow -it$.

$$\hbar\partial_t\psi(x, t) = \left(\frac{\hbar^2}{2m}\nabla^2 - V_{ext}(x, t) \right) \psi(x, t) \quad (5.1)$$

For convenience we will take $\hbar \rightarrow 1$ and the mass $m \rightarrow 1$. Among the plethora of IT methods, the simplest use Backwards-Euler (BEFD) or Crank-Nicholson (CNFD) finite difference

schemes to recover the diffusion equation. For example the BEFD scheme is shown below.

$$\phi_i^n = \phi(x_i, t_n)$$

$$\begin{aligned} \frac{\phi_i^{n+1} - \phi_i^n}{\Delta t} &= \frac{1}{2m\Delta x} (\phi_{i+1}^{n+1} - 2\phi_i^{n+1} + \phi_{i-1}^{n+1}) - \mathbf{V}_{(\text{ext}),i}^n \phi_i^{n+1} - \mathbf{V}_{(\text{int}),i}^n \phi_i^{n+1} \\ \phi_i^{n+1} - \phi_i^n &= \frac{\Delta t}{2m\Delta x^2} (\phi_{i+1}^{n+1} - 2\phi_i^{n+1} + \phi_{i-1}^{n+1}) - \Delta t (\mathbf{V}_{(\text{ext}),i}^n + \mathbf{V}_{(\text{int}),i}^n) \phi_i^{n+1} \\ \phi_i^n &= \phi_i^{n+1} - \frac{\Delta t}{2m\Delta x^2} (\phi_{i+1}^{n+1} - 2\phi_i^{n+1} + \phi_{i-1}^{n+1}) + \Delta t (\mathbf{V}_{(\text{ext}),i}^n + \mathbf{V}_{(\text{int}),i}^n) \phi_i^{n+1} \\ \phi_i^n &= \left\{ 1 + \frac{\Delta t}{m\Delta x^2} + \Delta t (\mathbf{V}_{(\text{ext}),i}^n + \mathbf{V}_{(\text{int}),i}^n) \right\} \phi_i^{n+1} - \frac{\Delta t}{2m\Delta x^2} (\phi_{i+1}^{n+1} + \phi_{i-1}^{n+1}) \end{aligned}$$

Due to the nature of the diffusion equation, one has to normalize the wavefunction after every iteration to prevent the system from simply diffusing out. BEFD and CNFD involve inverting a matrix that is determined by the size of the simulation grid. Alternatively we can utilize the QLG scheme presented in Section [3.4] with a modified collision operator, $\hat{\mathcal{C}}_{\text{IT}}$, to perform IT integration.

$$\hat{\mathcal{C}}_{\text{IT}} = \hat{U} = \frac{\text{Cos}(\frac{\pi}{4} + \frac{1}{c}V(x, t))}{\sqrt{2}} \begin{pmatrix} 1 & 1 \\ 1 & 1 \end{pmatrix} \quad (5.2)$$

$$c_{1D} = 8, \quad c_{2D} = 16, \quad c_{3D} = 24$$

Not surprisingly $\hat{\mathcal{C}}_{\text{IT}}$ is no longer unitary, this has been noted by Succi and his collaborators²⁹, after all we are trying to model the diffusion equation which does not preserve the norm of a system. As such this particular IT scheme would not be applicable on a quantum computer, but the initial condition it generates can still serve its purpose on any system (classical or

quantum). As mentioned previously, we resolve the non-unitary aspect by normalizing the wavefunction after every collision step with the normalized density N on a domain Ω defined as

$$N(\psi) = \int_{\Omega} |\psi|^2 d\vec{x} \quad (5.3)$$

$\hat{\mathcal{C}}_{\text{IT}}$ when used in the the collide-stream sequence of eq. [3.56 recovers our dimensionless form of the diffusion equation

$$\psi(x, t + \Delta t) = \{1 - 8\epsilon^2 V(x, t) + \epsilon^2 \nabla^2 + \mathcal{O}(\epsilon^4)\} \psi(x, t) \quad (5.4)$$

The IT algorithm consists of 5 steps:

1. initialize the wavefunction, $\psi(x, t)$
2. encode the wavefunction into a qubit pair, (q_1, q_2)
3. apply the collide-stream sequence in eq. [3.56] using $\hat{\mathcal{C}} = \hat{\mathcal{C}}_{\text{IT}}$
4. normalize the qubits after every collision
5. update the wavefunction, $\psi(x, t) = q_1 + q_2$

5.2 1D SHO

We first consider the IT integration of the 1D simple quantum harmonic oscillator (SHO) to ensure that the algorithm can correctly recover the analytically known ground

state solutions presented in Section [4.1]. For the initial wave function we consider two cases: first the analytic solution itself (to verify that the IT algorithm does not introduce spurious deviations), and a second case where the wavefunction is a constant horizontal line. We consider a domain $\Omega = [-500, 500]$ with $\Delta x = \frac{1}{\sqrt{2}}$. This choice of Δx is so that we may recover the $1/2$ term in front of the ∇^2 operator. We take the usual harmonic potential,

$$V_{ext} = \frac{1}{2}m(\omega x)^2 = \frac{1}{2}kx^2 \tag{5.5}$$

$$k = 1/\Omega$$

In Fig. [5.1a] we plot the results from our IT-QLG algorithm for the analytic initial condition. The profiles overlap rather well, with the respective error shown in [5.1b]. IT methods are rather robust in the sense that one can choose arbitrary initial conditions and often end up with the same ground state solution. In particular, for our second case we chose $\psi = \text{constant}$ as our initial condition. The imaginary QLG algorithm recovers the analytic solution with a similar error range, Fig. [5.1c - d]. Interestingly, it is possible to recover the first excited state of the SHO when taking an initial condition with two peaks of the same amplitude.

5.3 1D NLS

We next consider the 1D NLS problem presented in Chapter [3]. We intend to compare our result with that of Succi²⁹ as well as with the results from the backward-Euler finite-

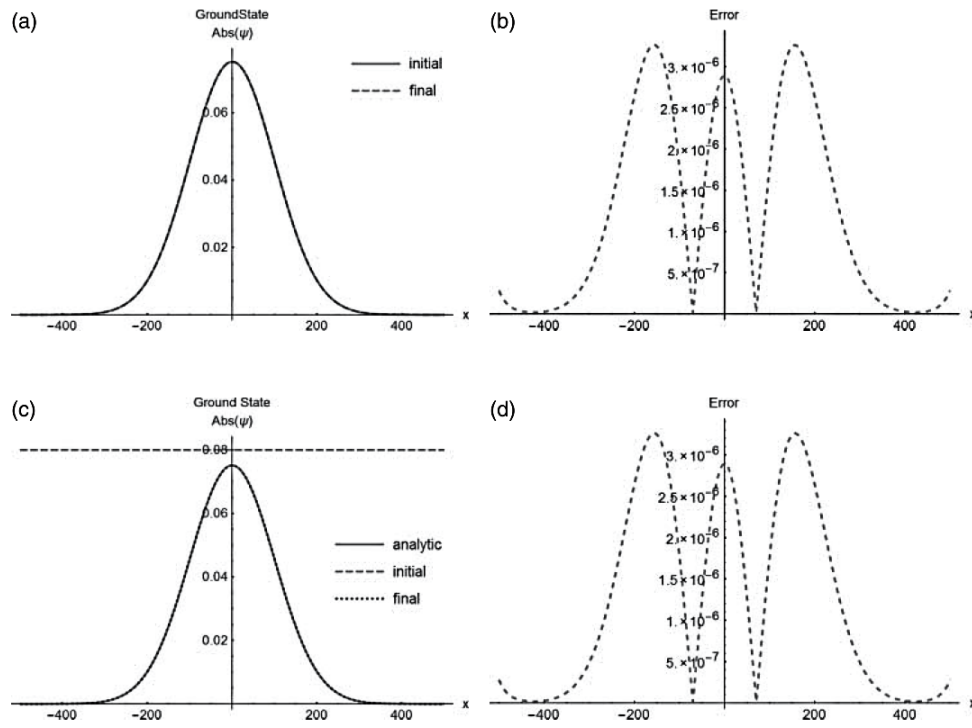


FIG. 5.1: (a) IT-QLG testing stability over 4×10^5 iterations. $\Omega = [-500, 500]$, $\Delta x = \frac{1}{\sqrt{2}}$, $k = \frac{1}{\Omega^2}$. (b) $Error = |\psi_{analytic} - \psi_{IT}|$. Comparing the analytic ground state for the SHO and the IT-QLG algorithm result. (c) IT-QLG ground state solution after 3.5×10^3 iterations, same parameters as in Fig.[5.1a]. (d) $Error = |\psi_{analytic} - \psi_{IT}|$.

difference (BEFD) method. In order to model the same system we use the following potential in our collision operator

$$V(x, t) = V_{\text{ext}}(x) + V_{\text{int}}(x, t) = \frac{1}{2}m(\omega x)^2 + \beta|\psi(x, t)|^2 \quad (5.6)$$

Where β once again is ± 1 depending on whether we are working with bright or dark solitons. For our initial condition we take a Gaussian profile

$$\psi(x, 0) = (2\pi\Delta_0^2)^{1/4} e^{-\frac{(x-x_0)^2}{4\Delta_0^2}} \quad (5.7)$$

Using the same parameters as in Succi et al.²⁹, $\Delta_0 = 16$, $\omega = \frac{1}{128}$, and $m = 1/8$ we recover their results for the case $\beta = 1$ which are illustrated in fig. [5.2]. The BEFD method requires one to perform matrix inversion whereas QLG is only comprised of matrix multiplication. This difference is very significant when it comes to computation time, especially in higher dimensions. An important note is that $m \neq 1$ in this case, we accommodate this by simply rescaling the system. That is we simply change c in eq. [5.2], $c \rightarrow \frac{c}{m}$

Next we consider the 1D NLS with no external potential and a $\beta < 0$ to recover a bright-soliton stationary state. For an initial real wave function, we readily obtain a steady-state soliton from the IT QLG shown in Fig. [5.3a]. If the initial wave function has a small complex phase then invariably our IT-QLG algorithm will converge to a purely real wavefunction (soliton) solution. However, if the complex phase is sufficiently large one can recover an additional soliton, akin to the first excited state. It is interesting to note that

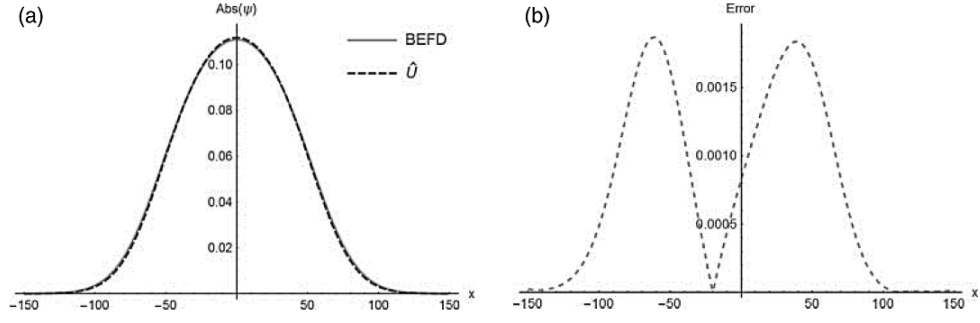


FIG. 5.2: (a) Matching Succi's result for the 1D NLS equation. $\Omega = [-150, 150]$, $\Delta x = \frac{1}{2}$, $\Delta_0 = 16$, $\omega = \frac{1}{128}$, $m = 1/8$ and $\beta = +1$. (b) Difference between the BEFD ($\Delta x = 0.1$) converged value versus the QLG-IT algorithm, $Error = |\psi_{BEFD} - \psi_{IT}|$.

since we do not perform any matrix inversions, like many IT algorithms have to do, we have no difficulty with complex wavefunctions as our initial condition.

To test the accuracy of our IT-QLG non-unitary algorithm, we have used the resulting initial condition solution in the unitary time-evolving QLG that solves the 1D NLS. We indeed have verified that the IT initial solution is invariant under the unitary time-evolving QLG, and in Fig. [5.3b], we plot the energy integral and find that it is indeed constant to good accuracy.

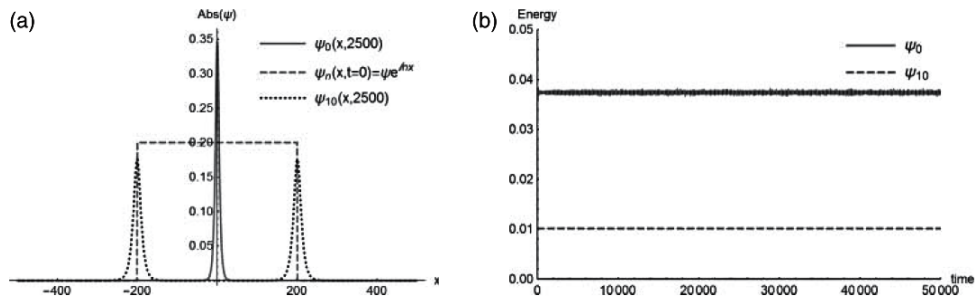


FIG. 5.3: (a) Stationary bright-soliton solutions for the 1D NLS. $\Omega = [-500, 500]$, $\beta = -1$, $\Delta x = 1$. Here, ψ_0 is purely real producing a single soliton and ψ_{10} has a complex phase producing two solitons. (b) Energy of the stationary solutions when substituted into the time-evolving unitary QLG algorithm.

For the case of $\beta = +1$, it is difficult to get an initial steady-state that is not simply the

asymptote of the BEC itself. Thus we introduce a very small external potential of the form

$$V_{ext}(x) = \frac{\alpha}{\text{Cosh}(x - x_0)} \quad (5.8)$$

in order to generate the dark-soliton solutions. α is just an amplitude parameter for the potential and is what influences the depth of the dark-soliton. A dark-soliton solution is shown in Fig. [5.4a]. As with the bright soliton we have substituted the IT result into our time-evolving unitary QLG algorithm and have verified that the solution is indeed a steady state. It should be noted that in the unitary time-evolving QLG algorithm one must include the external potential that was used in the IT method. The dark soliton is indeed a steady-state solution and the energy integral, plotted in [5.4b], is shown to be a constant.

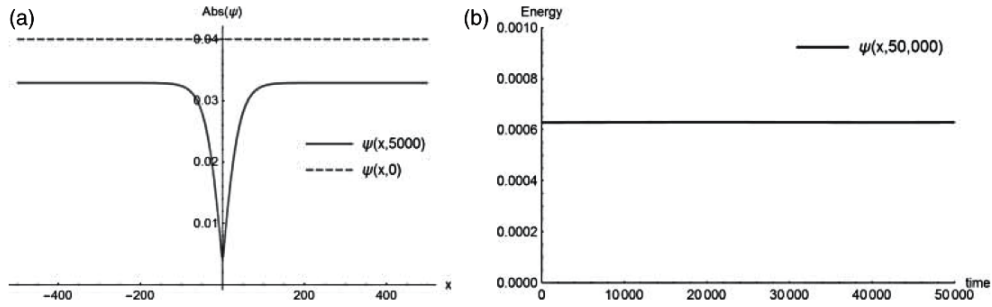


FIG. 5.4: (a) Stationary dark-soliton solution for the 1D NLS. $\Omega = [-500, 500]$, $\beta = +1$, $\Delta x = 1$, $\alpha = 0.1$. (b) Energy stability of the stationary solution when substituted into the time-evolving QLG algorithm for 5×10^4 time steps.

CHAPTER 6

Road Forward

6.1 Fourier Operator Splitting

Recall in section [3.3] when deriving $\hat{\mathcal{C}}_{\text{rel}}$ we took the composition of two unitary operators, which approximated the kinetic, ∇^2 , and potential, $V(x, t)$, operators of the Hamiltonian as commuting when they actually are not.

$$H = T + V$$

$$\psi(x, t + \Delta t) = e^{-i\Delta t H} \psi(x, t) \tag{6.1}$$

$$e^{-i\Delta t H} \neq e^{-i\Delta t T} e^{-i\Delta t V}$$

There is indeed a better way to approach this dilemma via the Suzuki-Trotter decomposition, an operator splitting technique presented by Barenghi in a review³⁰.

$$e^{-i\Delta t H} \approx e^{-i\Delta t \frac{V}{2}} e^{-i\Delta t T} e^{-i\Delta t \frac{V}{2}} \quad (6.2)$$

$$\psi(x, t + \Delta t) = e^{-\frac{i\Delta t V}{2}} \mathcal{F}^{-1} \left\{ e^{-i\Delta t k^2} \cdot \mathcal{F} \left[e^{-\frac{i\Delta t V}{2}} \psi(x, t) \right] \right\}$$

In eq. [6.2] \mathcal{F} and \mathcal{F}^{-1} are the Fourier and the inverse Fourier transform respectively. Thus, no longer are we using streaming operator $\hat{\mathcal{S}}$ to recover the kinetic term through finite difference, but instead we perform a Fourier transform and then its inverse. Furthermore our potential is applied via the collision operator $\hat{\mathcal{C}}$ rather than the exponential $e^{-i\Delta t V}$. The complete sequence of events in QLG for one time step becomes

$$\begin{pmatrix} q_1(x, t + \Delta t) \\ q_2(x, t + \Delta t) \end{pmatrix} = \hat{\mathcal{C}} \mathcal{F}^{-1} \left\{ e^{-i\Delta t k^2} \cdot \mathcal{F} \left[\hat{\mathcal{C}} \begin{pmatrix} q_1(x, t) \\ q_2(x, t) \end{pmatrix} \right] \right\} \quad (6.3)$$

$c = 2$

In eq. [6.3] $c = 2$ because we apply the collision operator twice. Furthermore unlike previously where we only specified Δx and the diffusion ordering was automatically respected assuming we were in the correct parameter regime, in this scheme we must specify both Δx and Δt and ensure the our choice preserves the diffusion ordering. An important remark is that using Fourier transforms limits us to periodic boundary conditions due to the nature of FFT algorithms. While there are methods to use non-periodic boundary conditions with Fourier transforms, they involve a lot of hoops to jump through that become impractical

when dealing with very large grids in 3D. We will spare the reader the successful Simple Harmonic Oscillator results and instead in fig. [6.1] present a successful simulation of bright soliton-soliton collision using the method in eq. [6.2]. While the Fourier transform can

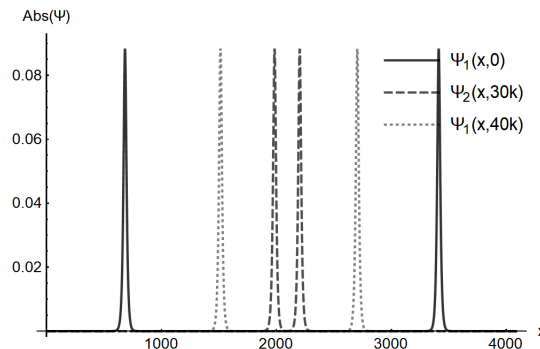


FIG. 6.1: Bright-soliton collision using the QLG sequence presented in eq. [6.2]. Simulation performed on a grid of length $L = 4096$ with $\Delta x = \Delta t = 1$, and velocity $\beta = 0.06875$ with the left most soliton moving to the right and right soliton to the left.

be a very non-local step in classical physics, in quantum computing the quantum Fourier transform scales beautifully with increasing lattice size and is an ideal unitary operator to introduce. Indeed, it is known that factoring a large number into its 2 (also large) prime number constituents is an exponentially hard problem in classical algorithms but it has been shown by Shor that the factorization scales only algebraically with the use of quantum entanglement. Moreover, behind this exponential speed was Shor's use of the quantum Fourier transform. This also leads to the subject of quantum cryptography. Naturally a future goal that is underway is extending the approach in eq. [6.3] to 3D and using higher order operator decompositions so as to model more complex systems.

6.2 Spin-1 Interaction

A future goal is to model the spin-1 interaction in the GPE that is expressed in the following set of coupled equations

$$\begin{aligned}
i\partial_t\psi_{(m=1)} &= (-\nabla^2 + V_{ext})\psi_1 + (c_0N - \mu + c_1F_z)\psi_1 + \frac{c_1}{\sqrt{2}}F_+\psi_0 \\
i\partial_t\psi_{(m=0)} &= (-\nabla^2 + V_{ext})\psi_0 + (c_0N - \mu)\psi_0 + \frac{c_1}{\sqrt{2}}F_+\psi_1 + \frac{c_1}{\sqrt{2}}F_-\psi_{-1} \\
i\partial_t\psi_{(m=-1)} &= (-\nabla^2 + V_{ext})\psi_{-1} + (c_0N - \mu - c_1F_z)\psi_{-1} + \frac{c_1}{\sqrt{2}}F_-\psi_0
\end{aligned} \tag{6.4}$$

$$N = \sum_{m=-1}^1 |\psi_m|^2$$

$$F_z = |\psi_1|^2 - |\psi_{-1}|^2 \tag{6.5}$$

$$F_+ = (\psi_1^*\psi_0 + \psi_0^*\psi_{-1})$$

$$F_- = F_+^*$$

F is the spin density vector, $\vec{F}(r) = \psi^\dagger \vec{f} \psi$ and \vec{f} is the spin-1 matrix vector. N is the total density of the system and c_0 is our standard g parameter presented in Appendix [C], while c_1 is the spin interaction strength. The spin-1 Zeeman manifold is a vector system similar to that of the vector solitons presented in section [4.3] but there are some important differences. For our vector soliton system with two coupled equations, we can effectively

write our collision operator as a 4×4 matrix acting on two qubit pairs

$$\begin{pmatrix} \hat{C}_{11}^{Q_1} & \hat{C}_{12}^{Q_1} & 0 & 0 \\ \hat{C}_{21}^{Q_1} & \hat{C}_{22}^{Q_1} & 0 & 0 \\ 0 & 0 & \hat{C}_{11}^{Q_2} & \hat{C}_{12}^{Q_2} \\ 0 & 0 & \hat{C}_{21}^{Q_2} & \hat{C}_{22}^{Q_2} \end{pmatrix} \begin{pmatrix} q_{1_1} \\ q_{2_1} \\ q_{1_2} \\ q_{2_2} \end{pmatrix} \quad (6.6)$$

Unlike in eq. [6.6] where the system is diagonal, the spin-1 system is not due to the presence of mixed terms. Our first attempt at a collision operator was an approximation that was unitary only to $\mathcal{O}(\epsilon^2)$, similar to that of our algorithm. Because we have 3 equations, we require 3 qubit pairs and a 6×6 operator for the system

$$\hat{c}_{\text{spin-1}} = \frac{1}{\sqrt{2}} \begin{pmatrix} 1 - \epsilon(G_0 + c_1 F_z) & -i(1 + \epsilon(G_0 + c_1 F_z)) & -\epsilon c_2 F_- & -i\epsilon c_2 F_- & 0 & 0 \\ -i(1 + \epsilon(G_0 + c_1 F_z)) & 1 - \epsilon(G_0 + c_1 F_z) & -i\epsilon c_2 F_- & -\epsilon c_2 F_- & 0 & 0 \\ -\epsilon c_2 F_+ & -i\epsilon c_2 F_+ & 1 - \epsilon G_0 & -i(1 - \epsilon G_0) & -\epsilon c_2 F_- & -i\epsilon c_2 F_- \\ -i\epsilon c_2 F_+ & -\epsilon c_2 F_+ & -i(1 - \epsilon G_0) & 1 - \epsilon G_0 & -i\epsilon c_2 F_- & -\epsilon c_2 F_- \\ 0 & 0 & -\epsilon c_2 F_+ & -i\epsilon c_2 F_+ & 1 - \epsilon(G_0 - c_1 F_z) & -i(1 + \epsilon(G_0 - c_1 F_z)) \\ 0 & 0 & -i\epsilon c_2 F_+ & -\epsilon c_2 F_+ & -i(1 + \epsilon(G_0 - c_1 F_z)) & 1 - \epsilon(G_0 - c_1 F_z) \end{pmatrix} \quad (6.7)$$

$$G_0 = c_0 N - \mu$$

$$c_2 = c_1 / \sqrt{2} \quad (6.8)$$

$$CC^\dagger = I_6, \quad \text{2nd order in } \epsilon$$

Recently Yezpez³¹ has determined the collision operator accurate to all orders for a spin-1 GP system, so future simulations are in order.

CHAPTER 7

Conclusion

In this dissertation we have presented the most recent QLG algorithm that is a direct upgrade to its predecessor, which is capable of modeling various systems in the weak interaction regime. Specifically we presented results for the GP system, modeling a neutral Bose-Gas where only nearest-neighbor interactions play a role. We have successfully modeled the GPE in 1D and 3D, in each case capturing the expected physical behavior. The unitary nature of QLG leads to the unconditional conservation of density and energy of a quantum system and allows its implementation on both quantum and classical computers. Furthermore the algorithm is extremely scalable as shown in figures [7.1] and [7.2], able to take full advantage of super-computers. QLG is further compatible with the latest implementations both in hardware and software. The code can use MPI, OpenMP thread technology and graphic accelerators (Cuda, OpenCL), all simultaneously or any combination of that delivers the best performance.

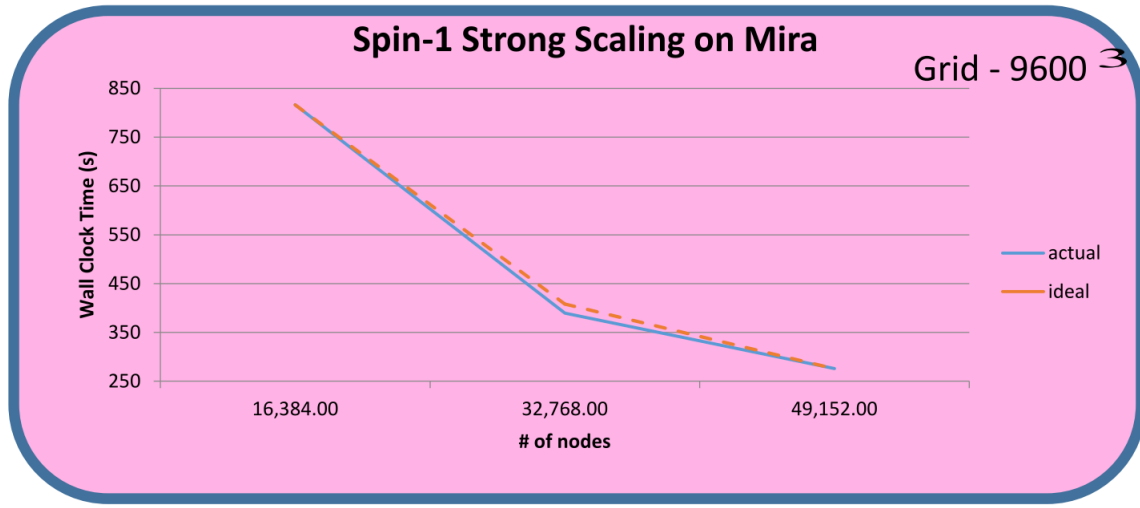


FIG. 7.1: Testing strong scalability of a prototype spin-1 QLG algorithm on the Argonne's super-computer Mira.

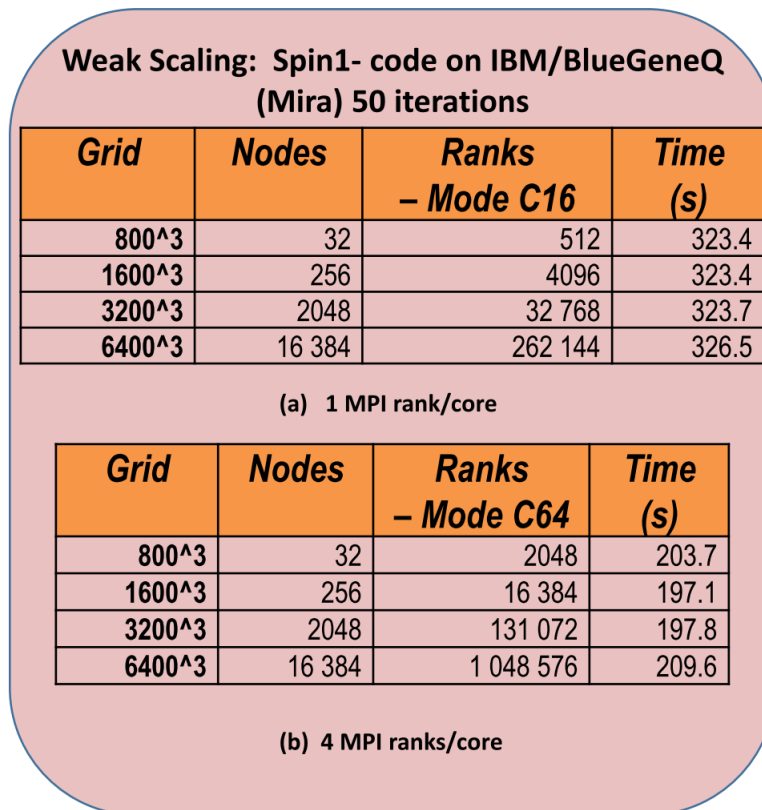


FIG. 7.2: Testing weak scalability of a prototype spin-1 QLG algorithm on the Argonne's super-computer Mira.

We have also presented a map forward for future work with some preliminary results for the Fourier operator splitting method. While this places restrictions on the boundary conditions, there are other more sophisticated streaming algorithms that can also be employed which would allow us to use non-periodic boundary conditions. Due to the diffusion ordering present in the QLG algorithm one of the biggest challenges is extending the method to incorporate strong interactions such as a coulomb interaction present in a plasma for example. We have been able to broaden the parameter range of QLG with the non-relativistic collision operator and future works will focus on taking this even further.

APPENDIX A

BEC Phase State Derivation

Below is a derivation of the BEC phase state. We begin with the Bose-Einstein distribution function for bosonic matter,

$$f(E) = \frac{1}{e^{(E - \mu)/k_B T} - 1} \quad (\text{A.1})$$

where E is the energy, k_B is the Boltzmann's constant (1.38×10^{23} *joule/K*), and μ is the chemical potential, or energy required to add/remove a particle into/from the ensemble. The distribution function is so called because it tells us the distribution of particles across possible states as a function of energy. We consider an ideal, neutral gas of bosons confined in some volume V that obeys the above distribution function. For simplicity we also assume a continuous energy spectrum, thus a large number of available energy levels for particles to occupy. We will later see that this simplification doesn't properly account for particles in the ground state but is sufficient for our sought-after result. The number of particles with energy E can be described by

$$N(E) = g(E)f(E) \quad (\text{A.2})$$

where $g(E)$ is the density of states, a measure of degeneracy corresponding to a particular energy, that is the number of states between energies E and $E + dE$. It is expressed as

$$g(E) = \frac{2\pi(2m)^{3/2}V}{h^3} E^{1/2} \quad (\text{A.3})$$

V is the physical volume of our gas, m is the mass and h is Planck's constant ($6.626 \times 10^{34} \text{ Js}$). Substituting equations (A.1 and A.3) into A.2 we can express the total number of particles as

$$N = \frac{2\pi(2m)^{3/2}V}{h^3} \int_0^\infty \frac{E^{1/2}}{e^{(E-\mu)/k_B T} - 1} dE \quad (\text{A.4})$$

The above integral is challenging but fortunately falls into a known class of integrals with a solution. It can be expressed in a more general form as a product of the Gamma³² function, $\Gamma(\alpha)$, and the polylogarithm³³ function, $Li_n(z)$ (which coincides with the Riemann-zeta function when $z = 1$).

$$\int_0^\infty \frac{x^\alpha}{e^{x/z} - 1} dx = \Gamma(\alpha + 1) Li_{\alpha+1}(z) \quad (\text{A.5})$$

$$\Gamma(x) = \int_0^\infty t^{x-1} e^{-t} dt \quad (\text{A.6})$$

$$Li_n(z) = \sum_{p=1}^\infty \frac{z^p}{(p+c)^n} \quad (\text{A.7})$$

Matching the coefficients of eq. [A.5] with A.4 we have $\alpha = 1/2$, $x = E/k_B T$, $z = e^{\mu/k_B T}$, $c = 0$, and $\Gamma(3/2) = \sqrt{\pi}/2$. Upon evaluation our expression for the number of particles N reduces to

$$N = \frac{(2\pi m k_B T)^{3/2} V}{h^3} Li_{3/2}(z) \quad (\text{A.8})$$

Before we proceed, there are some important physical observations that we need to consider that will allow us to place limits on $z = e^{\mu/k_B T}$. In order for our distribution function A.1 to

represent reality $f(E) \geq 0$, otherwise we would have a negative number of particles. This requirement places a restriction that $\mu \leq 0$. This in turn places an easy to see limit on z , $0 < z \leq 1$. Below we plot the polylogarithm function with our set of parameters in FIG. [A.1]. Of note is the maximum value of $Li_{3/2}(1) = 2.6123$. Our main result is obtained

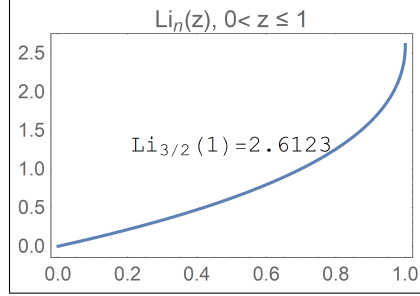


FIG. A.1: The polylogarithm function $Li_n(z) = \sum_{p=1}^{\infty} \frac{z^p}{(p+c)^n}$ plotted for $n = 3/2$, $c = 0$ and $0 < z \leq 1$.

from eq. [A.8], because it seemingly places an upper bound on the number of particles the distribution may contain. If we wish to add particles, we need to increase the density of states, but this values has an upper bound.

$$N_c = \frac{(2\pi mk_B T)^{3/2} V}{h^3} \zeta^{3/2} = 2.6123 \frac{(2\pi mk_B T)^{3/2} V}{h^3} \quad (\text{A.9})$$

Where we've expressed the polylogarithmic function with its Zeta (ζ) function counterpart for $z = 1$. We know that for bosons we can always add more particles, so what is this upper bound then? It stems from the simplification we made in the beginning of using a continuous energy spectra, our density of state $g(E) \propto E^{1/2}$, would imply that for the ground state of $E = 0$, the density is also 0, which of course is not true. Thus our simplified approach did not account for particles in the ground state, but what it has shown, is that there is an upper limit of particles that can occupy the excited states. Additional particles added after the critical number density is reached, as predicted by Einstein, will be added to the ground

state of the system. Of note is that we may also lower the temperature of the system, which would decrease N_c , and any particles occupying excited states would then be moved to the ground state, this is the underlying principle used to create the BEC phase via cooling.

APPENDIX B

Brief Derivation of Second Quantization

Normally we deal with single-particle quantum mechanics, but if we want to treat more than one particle we have to expand our Hilbert space H . Just like going from 1 to 2 dimensions we take $R \rightarrow R \otimes R$, we similarly expand our Hilbert space by having $H \rightarrow H \otimes H$, and $H^n = H \otimes \dots \otimes H$ for n particles. We can right away write a two particle state as $|1\rangle \otimes |2\rangle$ in $H \otimes H$.

$$\langle r_1, r_2 | (|1\rangle \otimes |2\rangle) = \langle r_1 | 1 \rangle \langle r_2 | 2 \rangle = \phi(r_2) \phi(r_1) \quad (\text{B.1})$$

A general 2-particle state in H^2 can be written as

$$|\psi\rangle_2 = \alpha(|1\rangle \otimes |2\rangle) + (-1)^p \beta(|2\rangle \otimes |1\rangle) \quad (\text{B.2})$$

where $p = 0$ for bosons and $p = 1$ for fermions. From this general expression we can write down the Slater determinant to represent an anti-symmetric wavefunction.

$$\langle r_1, r_2 | \psi \rangle_2^f = \frac{1}{\sqrt{2}} (\phi_1(r_1)\phi_2(r_2) - \phi_2(r_1)\phi_1(r_2)) = \frac{1}{\sqrt{2}} \begin{pmatrix} \phi_1(r_1) & \phi_1(r_2) \\ \phi_2(r_1) & \phi_2(r_2) \end{pmatrix} \quad (\text{B.3})$$

Generalization to N particles is trivial and the subspace spanned by the anti-symmetric states is called Fock's space for fermions. The state indices increase with the rows by convention for writing the Slater determinant. For bosons, instead of taking the determinant, we take the permanent which only has pluses and no minuses. For N particles the normalization becomes $(\frac{1}{\sqrt{N!}})$. An alternative representation for the Slater determinant is to write a state with 1's in positions where particles are present and 0's where they are not.

$$|\psi\rangle_{l,m}^f = |0, \dots, 0, \underbrace{1}_l, 0, \dots, 0, \underbrace{1}_m, 0, \dots\rangle \quad (\text{B.4})$$

This is the occupation number representation for fermionic states. In expanding our Hilbert space our goal is to be able to add as many particles as we want to our system. We can do this using creation and annihilation operators acting on the vacuum state.

$$\begin{aligned} |0\rangle_{l,m} &= |0, \dots, 0, \underbrace{0}_l, 0, \dots, 0, \underbrace{0}_m, 0, \dots\rangle \\ c_m^\dagger |0\rangle &= |0, \dots, 0, \underbrace{1}_m, 0, \dots\rangle \\ c_l^\dagger c_m^\dagger |0\rangle &= |0, \dots, 0, \underbrace{1}_l, 0, \dots, 0, \underbrace{1}_m, 0, \dots\rangle \equiv |\psi\rangle_{l,m}^f \\ c_m^\dagger c_l^\dagger |0\rangle &= -|0, \dots, 0, \underbrace{1}_l, 0, \dots, 0, \underbrace{1}_m, 0, \dots\rangle \equiv |\psi\rangle_{m,l}^f \end{aligned} \quad (\text{B.5})$$

Here we have taken c_n^\dagger to be the creation operator and conversely its conjugate c_n is the annihilation operator. From the last two equations above we get the anti-commutation relations for fermions due to their anti-symmetry.

$$\begin{aligned}
(c_m^\dagger c_l^\dagger + c_l^\dagger c_m^\dagger)|0\rangle &= 0 \\
(c_m^\dagger c_l^\dagger + c_l^\dagger c_m^\dagger) &= 0 \\
\{c_l, c_m\} &= 0 \\
\{c_l^\dagger, c_m^\dagger\} &= 0 \\
\{c_l, c_m^\dagger\} &= \delta_{lm}
\end{aligned} \tag{B.6}$$

Similarly for bosons we have commutation relations since they are symmetric,

$$\begin{aligned}
[c_l, c_m] &= 0 \\
[c_l^\dagger, c_m^\dagger] &= 0 \\
[c_l, c_m^\dagger] &= \delta_{lm}
\end{aligned} \tag{B.7}$$

We convert our one particle state from $|\alpha\rangle$ to $|\alpha'\rangle$ by the usual unitary transformation,

$$\begin{aligned}
|\alpha'\rangle &= \sum_{\alpha} |\alpha\rangle \langle \alpha | \alpha'\rangle \\
\sum_{\alpha} |\alpha\rangle \langle \alpha| &= 1 \text{ (completeness)}
\end{aligned} \tag{B.8}$$

The indices α correspond to quantum numbers that describe a particular state (ie. spin). Our creation operator transforms similarly,

$$\begin{aligned}
c_{a'_{N+1}}^\dagger |a'_1, a'_2, \dots, a'_N\rangle &= |a'_1, a'_2, \dots, a'_N, a'_{N+1}\rangle \\
&= \sum_a \langle a_{N+1} | a'_{N+1} \rangle |a'_1, a'_2, \dots, a'_N, \underbrace{a_{N+1}}_{\text{not primed}} \rangle \\
&= \sum_a \langle a_{N+1} | a'_{N+1} \rangle c_{a_{N+1}}^\dagger |a'_1, a'_2, \dots, a'_N\rangle \\
c_{a'}^\dagger &= \sum_a \langle a | a' \rangle c_a^\dagger
\end{aligned} \tag{B.9}$$

Knowing how our creation and annihilation operators transform allows us to represent our state in the position or momentum basis. For example changing to the position basis,

$$\begin{aligned}
\phi_a(r) &= \langle r | a \rangle \\
\psi^\dagger(r) &= \sum_a \langle a | r \rangle c_a^\dagger = \sum_a \phi_a^*(r) c_a^\dagger
\end{aligned} \tag{B.10}$$

$\psi^\dagger(r)$ is a creation (or annihilation) field operator that creates (destroys) a particle at a point r in space. Inversely this transformation is

$$c_a^\dagger = \int d^3r \langle r | a \rangle \psi^\dagger(r) = \int d^3r \phi_a(r) \psi^\dagger(r) \tag{B.11}$$

As an example let's consider the simple particle-number operator N .

$$\begin{aligned}
N &= \sum_a c_a^\dagger c_a \\
&= \int d^3r d^3r' \langle r | a \rangle \langle a | r' \rangle \psi^\dagger(r) \psi(r') \\
&= \int d^3r \psi^\dagger(r) \psi(r) = \rho(r)
\end{aligned} \tag{B.12}$$

Above we have used the completeness relation and the orthogonality of the position basis $\langle r|r'\rangle = \delta(r - r')$ to recover the last line with ρ as the particle-density operator. Consider a single-particle position operator A'_i that we'll expand in terms of two bases α and β .

$$\begin{aligned} A'_i &= \sum_{\alpha\beta} A'(r_i) |\alpha\rangle \langle \alpha||\beta\rangle \langle \beta| \\ &= \sum_{\alpha\beta} A'_{\alpha\beta} |\alpha\rangle \langle \beta| \\ A'_{\alpha\beta} &\equiv A'(r_i) \langle \alpha|\beta\rangle \end{aligned} \tag{B.13}$$

We want to extend this operation to N -particles, so we consider an N -body operator \mathbf{A} which is the sum of the single-particle operators A'_i .

$$\mathbf{A} = \sum_{i=1}^N A'_i \tag{B.14}$$

How does \mathbf{A} affect a many-particle state?

$$\mathbf{A}|\alpha_1, \alpha_2, \dots, \alpha_N\rangle = (|A'_1\alpha_1, \alpha_2, \dots, \alpha_N\rangle + |\alpha_1, A'_2\alpha_2, \dots, \alpha_N\rangle + \dots + |\alpha_1, \alpha_2, \dots, A'_N\alpha_N\rangle) \tag{B.15}$$

Knowing that $A'_i = \sum_{\alpha\beta} A'_{\alpha\beta} |\alpha\rangle\langle\beta|$ let's guess that $\mathbf{A} = |\alpha\rangle\langle\beta|$ and substitute it in eq. [B.15].

$$\begin{aligned}
\mathbf{A}|\alpha_1, \alpha_2, \dots, \alpha_N\rangle &= (|\alpha_1\rangle\langle\beta_1|\alpha_1, \alpha_2, \dots, \alpha_N\rangle + |\alpha_1, \alpha_2\rangle\langle\beta_2|\alpha_2, \dots, \alpha_N\rangle + \dots + |\alpha_1, \alpha_2, \dots, \alpha_N\rangle\langle\beta_N|\alpha_N\rangle) \\
&= \sum_{i=1}^N \langle\beta_i|\alpha_i\rangle |\alpha_1, \alpha_2, \dots, \alpha_N\rangle \\
&= \sum_{i=1}^N \delta_{\beta_i\alpha_i} |\alpha_1, \alpha_2, \dots, \alpha_N\rangle \\
&= c_{a_j}^\dagger \sum_{i=1}^N \delta_{\beta_i\alpha_i} (\pm 1)^{i-1} |\alpha_1, \alpha_2, \dots, (\text{no } \alpha_j), \dots, \alpha_N\rangle \\
\mathbf{A}|\alpha_1, \alpha_2, \dots, \alpha_N\rangle &= c_a^\dagger c_\beta |\alpha_1, \alpha_2, \dots, \alpha_N\rangle
\end{aligned} \tag{B.16}$$

We get at the above final result given that

$$c_{\beta_j} |\alpha_1, \alpha_2, \dots, \alpha_N\rangle = \sum_{i=1}^N \delta_{\beta_i\alpha_i} |\alpha_1, \alpha_2, \dots, (\text{no } \alpha_j), \dots, \alpha_N\rangle \tag{B.17}$$

The appearance of $(\pm 1)^{i-1}$ in eq. [B.16] when extracting the creation operator is dependent on whether we're dealing with bosons or fermions. With our guess we find that \mathbf{A} can be written simply in terms of our creation and annihilation operators.

$$\mathbf{A} = \sum_{\alpha\beta} A'_{\alpha\beta} c_\alpha^\dagger c_\beta \tag{B.18}$$

Our single-particle non-interacting Hamiltonian H' with an external potential V' is

$$H' = \frac{p^2}{2m} + V'(r) \tag{B.19}$$

Written in the position basis H' is

$$\langle r|H'|r'\rangle = -\frac{\hbar^2}{2m}\nabla^2\delta(r-r') + V'(r)\delta(r-r') \quad (\text{B.20})$$

Applying our second-quantization result in eq. [B.18] directly to the single-particle non-interacting Hamiltonian H' we have,

$$\begin{aligned} H &= \int d^3r d^3r' \langle r|H'|r'\rangle \psi^\dagger(r)\psi(r') \\ H_0 &= \int d^3r \psi^\dagger(r) \left(-\frac{\hbar^2}{2m}\nabla^2 + V'(r)\right) \psi(r) \end{aligned} \quad (\text{B.21})$$

The above result recovers the first term on the right hand side of eq. [2.2]. We next consider second quantization of the inter-particle interaction term. For this we need an operator that acts on two particles at the same time. First let's consider a general two-body operator.

$$\begin{aligned} A_{ij}^{(2)} &= \sum_{\alpha,\alpha',\beta,\beta'} |\alpha\rangle|\alpha'\rangle \langle\alpha|\langle\alpha'| A_{ij}^{(2)} |\beta\rangle|\beta'\rangle \langle\beta|\langle\beta'| \\ A_{ij}^{(2)} &= \sum_{\alpha,\alpha',\beta,\beta'} |\alpha\rangle|\alpha'\rangle A_{\alpha',\beta,\alpha,\beta'}^{(2)} \langle\beta|\langle\beta'| \\ A_{ij}^{(2)} &= \sum_{\alpha,\alpha',\beta,\beta'} A_{\alpha',\beta,\alpha,\beta'}^{(2)} |\alpha\rangle|\alpha'\rangle \langle\beta|\langle\beta'| \end{aligned} \quad (\text{B.22})$$

α and β act on particle i while α' and β' act on particle j . The operator for the whole system is then

$$A = \frac{1}{2} \sum_{i \neq j} A_{ij}^{(2)} \quad (\text{B.23})$$

We now make the same guess as before, that $A_{ij}^{(2)} = |\alpha\rangle|\alpha'\rangle\langle\beta|\langle\beta'|$. Acting with A on a state and substituting this assumption we have,

$$\begin{aligned}
A|\alpha_1\alpha'_1, \alpha_2\alpha'_2, \dots, \alpha_N\alpha'_N\rangle &= (|\alpha_1\rangle|\alpha'_1\rangle\langle\beta_1|\langle\beta'_1|\alpha_1\alpha'_1, \alpha_2\alpha'_2, \dots, \alpha_N\alpha'_N\rangle \\
&\quad + |\alpha_1\alpha'_1, \alpha_2\rangle|\alpha'_2\rangle\langle\beta_2|\langle\beta'_2|\alpha_2\alpha'_2, \dots, \alpha_N\alpha'_N\rangle \\
&\quad + \dots + |\alpha_1\alpha'_1, \alpha_2\alpha'_2, \dots, \alpha_N\rangle|\alpha'_N\rangle\langle\beta_N|\langle\beta'_N|\alpha_N\alpha'_N\rangle) \\
&= \sum_{i \neq j}^N \langle\beta'_j|\alpha_i\rangle\langle\beta_i|\alpha'_j\rangle|\alpha_1\alpha'_1, \alpha_2\alpha'_2, \dots, \alpha_N\alpha'_N\rangle \quad (\text{B.24}) \\
&= c_{\alpha_k}^\dagger c_{\alpha'_k}^\dagger \sum_{i \neq j}^N \delta_{\beta'_j\alpha_k} \delta_{\beta_i\alpha'_k} (\pm 1)^{i-1} (\pm 1)^{j-2} |\alpha_1\alpha'_1, \alpha_2\alpha'_2, \dots, (\text{no } \alpha_k\alpha'_k), \dots, \alpha_N\alpha'_N\rangle \\
A|\alpha_1\alpha'_1, \alpha_2\alpha'_2, \dots, \alpha_N\alpha'_N\rangle &= c_{\alpha}^\dagger c_{\alpha'}^\dagger c_{\beta} c_{\beta'} |\alpha_1\alpha'_1, \alpha_2\alpha'_2, \dots, \alpha_N\alpha'_N\rangle
\end{aligned}$$

The above result holds for when $i < j$ and $i > j$, and in general (putting back the coefficient we omitted in our assumption)

$$A = \frac{1}{2} \sum_{\alpha, \alpha', \beta, \beta'} A_{\alpha, \beta, \alpha, \beta'}^{(2)} c_{\alpha}^\dagger c_{\alpha'}^\dagger c_{\beta} c_{\beta'} \quad (\text{B.25})$$

We are now in a position to derive the second inter-particle interaction term of the second-quantization Hamiltonian. The matrix elements of the interaction term in position space are

$$\begin{aligned}
V^{(2)}(r_i, r_j) &= V_{r, r', r'', r'''}^{(2)} = \langle r | \langle r' | V^{(2)}(r_i, r_j) | r'' \rangle | r''' \rangle \\
&= V^{(2)}(r, r') \delta(r' - r'') \delta(r - r''') \quad (\text{B.26})
\end{aligned}$$

Substituting the result in eq. [B.26] into eq. [B.25] we get

$$\begin{aligned}
 V &= \frac{1}{2} \int dv dv' dv'' dv''' \langle r | \langle r' | V^{(2)}(r_i, r_j) | r'' \rangle | r''' \rangle \psi^\dagger(r) \psi^\dagger(r') \psi(r'') \psi(r''') \\
 V_{int} &= \frac{1}{2} \int d\mathbf{v} d\mathbf{v}' \psi^\dagger(\mathbf{r}) \psi^\dagger(\mathbf{r}') V^{(2)}(\mathbf{r}, \mathbf{r}') \psi(\mathbf{r}') \psi(\mathbf{r})
 \end{aligned}
 \tag{B.27}$$

The above recovers the second portion of the right hand side of eq. [2.2]. This fully recovers the second quantization Hamiltonian. Those interested in a more thorough look at this topic can refer to most graduate quantum texts, for example³⁴.

APPENDIX C

Dimensionless GPE

We need to substitute the rescaled units in eq. [2.19] into eq. [2.1]. First looking at how the time derivative changes,

$$\partial_{t_s} \psi(x_s, t_s) = \frac{\partial \psi}{\partial t_s} \frac{\partial t_s}{\partial t} = \frac{\partial \psi}{\partial t_s} \partial_t \left(\frac{t}{\tau} \right) = \frac{1}{\tau} \frac{\partial \psi}{\partial t_s} \quad (\text{C.1})$$

Next we consider the spatial derivative,

$$\begin{aligned} \partial_{x_s} \psi(x_s, t_s) &= \frac{\partial \psi}{\partial x_s} \frac{\partial x_s}{\partial x} = \frac{\partial \psi}{\partial x_s} \partial_x \left(\frac{x}{L} \right) = \frac{1}{L} \frac{\partial \psi}{\partial x_s} \\ \frac{\partial^2 \psi(x_s, t_s)}{\partial x_s^2} &= \frac{\partial}{\partial x_s} \left(\frac{\partial \psi(x_s, t_s)}{\partial x_s} \right) = \frac{\partial}{\partial x_s} \left(\frac{\partial \psi}{\partial x_s} \frac{\partial x_s}{\partial x} \right) \\ &= \left(\frac{\partial}{\partial x_s} \frac{\partial \psi}{\partial x_s} \right) \frac{\partial x_s}{\partial x} + \left(\frac{\partial}{\partial x_s} \frac{\partial x_s}{\partial x} \right) \frac{\partial \psi}{\partial x_s} \\ &= \left(\frac{1}{L} \frac{\partial}{\partial x_s} \frac{\partial \psi}{\partial x_s} \right) \partial_x \left(\frac{x}{L} \right) + \left(\frac{\partial}{\partial x_s} \frac{1}{L} \right) \frac{\partial \psi}{\partial x_s} \\ &= \left(\frac{1}{L} \frac{\partial}{\partial x_s} \frac{\partial \psi}{\partial x_s} \right) \left(\frac{1}{L} \right) + 0 \\ &= \frac{1}{L^2} \frac{\partial^2 \psi}{\partial x_s^2} \end{aligned} \quad (\text{C.2})$$

Substituting the results of eq. [C.1] and eq. [C.2] into eq. [2.1] we get,

$$i\frac{\hbar}{\tau}\partial_{t_s}\psi(x_s, t_s) = \left(-\frac{\hbar^2}{2m}\frac{1}{L^2}\nabla_s^2 + \frac{mL^2}{2}\omega^2(\vec{x}_s \cdot \vec{x}_s) + g|\psi(x_s, t_s)|^2 \right) \psi(x_s, t_s) \quad (\text{C.3})$$

Multiplying eq. [C.3] by $\frac{1}{m\omega^2x_s}$ and looking at the resulting units,

$$\begin{aligned} \left(\frac{1}{m\omega^2x_s} \right) i\frac{\hbar}{\tau}\partial_{t_s}\psi &= \frac{1}{m\omega^2x_s} \left\{ -\frac{\hbar^2}{2m}\frac{1}{L^2}\nabla_s^2 + \frac{mL^2}{2}\omega^2(\vec{x}_s \cdot \vec{x}_s) + \frac{4\pi\hbar^2Na}{m}|\psi|^2 \right\} \psi \\ i\left(\frac{1}{m\omega^2x_s} \right) \frac{mL^2}{\tau^2}\partial_{t_s}\psi &= \frac{1}{m\omega^2x_s} \left\{ -\frac{1}{2m}\frac{m^2L^4}{\tau^2}\frac{1}{L^2}\nabla_s^2 + \frac{mL^2}{2}\omega^2(\vec{x}_s \cdot \vec{x}_s) + \frac{m^2L^4}{\tau^2}\frac{L}{mL^3}|\psi|^2 \right\} \psi \\ i\left(\frac{1}{\omega^2x_s} \right) \frac{L^2}{\tau^2}\partial_{t_s}\psi &= \frac{1}{\omega^2x_s} \left\{ -\frac{L^2}{2\tau^2}\nabla_s^2 + \frac{L^2}{2}\omega^2(\vec{x}_s \cdot \vec{x}_s) + \left(\frac{L}{\tau} \right)^2 |\psi|^2 \right\} \psi \end{aligned} \quad (\text{C.4})$$

Taking $\omega = 1/\tau$ as our characteristic time and $x_s = L^2$ as our characteristic length eq. [C.4] reduces to,

$$i\partial_{t_s}\psi = \left\{ -\frac{1}{2}\nabla_s^2 + \frac{1}{2}(\vec{x}_s \cdot \vec{x}_s) + |\psi|^2 \right\} \psi \quad (\text{C.5})$$

In eq. [C.5] the coefficients are not shown, but rather the units of coefficients are shown to be gone. Thus we have made a dimensionless problem that is easy to work with numerically.

Writing out eq. [C.5] with the coefficients in place, starting with the first equation in eq. [C.4] and keeping $\tau = \frac{1}{\omega}$, $x_s = L^2$,

$$\begin{aligned} \left(\frac{1}{m\omega^2x_s} \right) i\frac{\hbar}{\tau}\partial_{t_s}\psi &= \frac{1}{m\omega^2x_s} \left\{ -\frac{\hbar^2}{2m}\frac{1}{L^2}\nabla_s^2 + \frac{mL^2}{2}\omega^2(\vec{x}_s \cdot \vec{x}_s) + \frac{4\pi\hbar^2Na}{m}|\psi|^2 \right\} \psi \\ i\left(\frac{\hbar}{m\omega x_s} \right) \partial_{t_s}\psi &= \left\{ -\frac{\hbar^2}{2m^2\omega^2x_s^2}\nabla_s^2 + \frac{1}{2}(\vec{x}_s \cdot \vec{x}_s) + \frac{\hbar}{m\omega}\frac{4\pi\hbar Na}{m\omega}|\psi|^2 \right\} \psi \end{aligned} \quad (\text{C.6})$$

From eq. [C.6] we can recognize some terms,

$$\begin{aligned}\epsilon &= \left(\frac{\hbar}{m\omega x_s} \right) \\ a_0 &= \sqrt{\frac{\hbar}{m\omega}}\end{aligned}\tag{C.7}$$

ϵ is a dimensionless constant and a_0 is the characteristic length of the system, set by the harmonic potential. With the definitions in eq. [C.7] we can rewrite eq. [C.6],

$$i\epsilon\partial_{t_s}\psi = \left(-\frac{\epsilon^2}{2}\nabla_s^2 + \frac{1}{2}(\vec{x}_s \cdot \vec{x}_s) + (4\pi a_0^2 N a) \epsilon |\psi|^2 \right) \psi\tag{C.8}$$

Choosing $x_s = \frac{\hbar}{m\omega}$ results in $\epsilon = 1$, and recovers our dimensionless GP equation with the dimensionless factor $g = (4\pi a_0^2 N a)$. Recall that $N = \frac{\# \text{ of particles}}{\text{volume}} = \frac{N'}{L^3}$, with N' as just a scalar number and now $L = a_0$, is the characteristic length. Substituting this into eq. [C.8] we recover

$$\begin{aligned}i\partial_{t_s}\psi &= \left(-\frac{1}{2}\nabla_s^2 + \frac{1}{2}(\vec{x}_s \cdot \vec{x}_s) + \left(\frac{4\pi a_0^2 N' a}{a_0^3} \right) |\psi|^2 \right) \psi \\ i\partial_{t_s}\psi &= \left(-\frac{1}{2}\nabla_s^2 + \frac{1}{2}(\vec{x}_s \cdot \vec{x}_s) + \left(\frac{4\pi N' a}{a_0} \right) |\psi|^2 \right) \psi\end{aligned}\tag{C.9}$$

We will drop the prime in N' from this point forward and our final expression for $g = \left(\frac{4\pi N a}{a_0} \right)$. Our choice for ϵ is appropriate for a weak interaction regime where the scattering length is much smaller than the characteristic length of the system ($a \ll a_0$). If we did not choose all trap frequencies to be equal then our external potential term simply would have been

$$V_{ext} = \frac{1}{2} \left(x^2 + \left(\frac{\omega_y}{\omega_x} \right)^2 y^2 + \left(\frac{\omega_z}{\omega_x} \right)^2 z^2 \right)\tag{C.10}$$

Typically in such a system the trapping frequency is strong along one direction (in this

case the x-direction), and this frequency sets the characteristic length of the system. In the absence of an external potential, the characteristic frequency is just the stationary state frequency, $\omega = \mu/\hbar$, where μ is the chemical potential of the system. The chemical potential μ is the amount of energy required to add or remove a particle from the system and has been omitted thus far for simplicity. It will be incorporated into the system in the form of an additional potential as we shall later see.

Bibliography

- [1] M. Morris Mano and Charles R. Kime. *Logic and Computer Design Fundamentals*. 4th ed. Prentice Hall, 2004. ISBN: 978-0131989269.
- [2] Richard P. Feynman. “Simulating physics with computers”. In: *International Journal of Theoretical Physics* 21(6/7) (1982), 467488.
- [3] Bruce Boghosian Jeffrey Yepez. In: *Computer Physics Communications* 146 (2002), pp. 280–294.
- [4] A. Einstein. In: *Sitzber Kgl Preuss Akad Wiss* (1925).
- [5] M. H. Anderson et al. In: *Science* 269.5221 (1995), pp. 198–201.
- [6] Harold J. MetcalfPeter van der Straten. *Laser Cooling and Trapping*. 1999. ISBN: 978-1-4612-1470-0.
- [7] L. P. Pitaevskii. In: *Soviet Physics JETP* 13.2 (1961).
- [8] Swann Piatecki Nir Navon and Kenneth Günter. “Dynamics and Thermodynamics of the Low-Temperature Strongly Interacting Bose Gas”. In: *Phys. Ref. Letter* 107 (2011).
- [9] C. Nore. M. Abid and M. E. Brachet. “Decaying Kolmogorov Turbulence in a Model of Superflow”. In: *Physics of Fluids* 9 (1997). DOI: 10.1063/1.869473.
- [10] B. M. Boghosian and W. Taylor. In: *Phys. Rev. E* 54 (1998).
- [11] Isaac L. Nielsen Michael A. Chuang. *Quantum Computation and Quantum Information*. Cambridge University Press, 2010. ISBN: ISBN 978-1-107-00217-3.

- [12] J. Yepez. “Lattice gas dynamics: Volume III Quantum algorithms for computational physics; Technical Report AFRL-VS-HA-TR-2006-1143”. In: *Air Force Research Laboratory: AFRL/RV Hanscom AFB MA 01731*. DTIC ADA474659 (2007).
- [13] J. Yepez. “Quantum lattice gas model of Dirac particles in 1+1 dimensions”. In: *arXiv:1307.3595 [quant-ph]* (2013).
- [14] Juha Javanainen and Janne Ruostekoski. “Symbolic calculation in development of algorithms: split-step methods for the GrossPitaevskii equation”. In: *Journal of Physics A: Mathematical and General* 39 (2006).
- [15] Eugene Merzbacher. *Quantum Mechanics*. 3rd ed. 1998, p. 656. ISBN: 0-471-88702-1.
- [16] Jie-Fang Zhang Xiao-Fei Zhang Qin Yang and W. M. Liu. “Controlling soliton interactions in Bose-Einstein condensates by synchronizing the Feshbach resonance and harmonic trap”. In: *Phys. Rev. A* 77 (2008).
- [17] General G. Neugebauer R. Meinel. “N-soliton solution of the AKNS class on arbitrary background”. In: *Phys. Lett. A* 100 (1984).
- [18] V.F. Zaitsev A.D. Polyenin. *Handbook of Nonlinear Partial Differential Equations*. 2nd ed. Chapman & Hall/CRC, Boca Raton, 2004, p. 1912. ISBN: 9781420087239.
- [19] G. B. Patridge K. E. Strecker and R. G. Hulet. “Formation and propagation of matter-wave soliton trains”. In: *Nature* 417 (2002), pp. 150–153.
- [20] Taiju Tsuboi. “Phase shift in the collision of two solitons propagating in a nonlinear transmission line”. In: *Phys. Rev. A* 40 (1989).
- [21] Paul J. Dellar. “An exact energy conservation property of the quantum lattice Boltzmann algorithm”. In: *Physics Letters A* 376 (2011), pp. 6–13.

- [22] K. Lakshmanan R. Radhakrishnan and J. Hietarinta. “Inelastic collision and switching of coupled bright solitons in optical fibers”. In: *Phys. Rev. E* 56 (1997).
- [23] K. Steiglitz M. K. Jakubowski and R. Squier. “State transformations of colliding optical solitons and possible applications to computation in bulk media”. In: *Phys. Rev. E* 58 (1998).
- [24] K. Steiglitz. “Time-gated Manakov spatial solitons are computationally universal”. In: *Phys. Rev. E* 63 (2001).
- [25] Qinglin Tang Weizhu Bao and Zhiguo Xu. “Numerical methods and comparison for computing dark and bright solitons in the nonlinear Schrödinger equation”. In: *Journal of Computational Physics* 235 (2013), pp. 423–445.
- [26] Yuji Hattori Makoto Tsubota Shinichiro Ogawa. “Vortex Reconnection and Acoustic Emission by the Numerical Analysis of the Gross-Pitaevskii Equation”. In: *Journal of Low Temperature Physics* 121 (2000).
- [27] Andrew W. Baggaley. “Helicity transfer during quantised vortex reconnection”. In: *arXiv:1403.8121v1 [physics.flu-dyn]* (2014).
- [28] Yepez J. Vahala G. and Vahala L. “Poincaré recurrence and spectral cascades in three-dimensional quantum turbulence.” In: *Phys. Rev. E* 84 (2011).
- [29] Succi S. Palpacelli S. and Spigler R. “Ground-state Computation of Bose-Einstein Condensates by an Imaginary-time Quantum Lattice Boltzmann Scheme”. In: *Phys. Rev. E* 76 (2007).
- [30] Carlo F. Barenghi and Nick G. Parker. *A Primer on Quantum Fluids*. Springer, 2016, p. 121. ISBN: 978-3-319-42476-7.
- [31] Yepez J. “Closed-form analytical continuation of spin density interactions in spin-2 superfluids”. In: *arXiv:1609.02229v2* (2016).

- [32] Hans J. Weber George B. Arfken. *Mathematical Methods for Physicists*. 6th ed. 2005, p. 527. ISBN: 978-0-12-059876-2.
- [33] W. C. Winnie Li Jeffrey C. Lagarias. In: *Research in the Mathematical Sciences* 3.2 (2016). DOI: 10.1186/s40687-015-0049-2.
- [34] Jim Napolitano J. J. Sakurai. *Modern Quantum Mechanics*. 2nd ed. 1994, p. 570. ISBN: 978-0-8053-8291-4.